NUMERICAL MODELING OF NEAR-FIELD THERMAL RADIATION IN COMPLEX, THREE-DIMENSIONAL AND MULTISCALE GEOMETRIES

by

Sheila Edalatpour

A dissertation submitted to the faculty of
The University of Utah
in partial fulfillment of the requirements for the degree of

Doctor of Philosophy

Department of Mechanical Engineering

The University of Utah

August 2016

The University of Utah Graduate School

STATEMENT OF DISSERTATION APPROVAL

The dissertation of **Sheila Edalatpour**

has been approved by the following supervisory committee members:

Mathieu Francoeur	, Chair	05/13/2016 Date Approved
Keunhan Park	, Member	05/13/2016 Date Approved
Tim Ameel	, Member	05/13/2016 Date Approved
Martin Čuma	, Member	05/13/2016 Date Approved
Fernando Guevara Vasquez	, Member	05/13/2016 Date Approved

and by **Tim Ameel** , Chair/Dean of

the Department/College/School of **Mechanical Engineering**

and by David B. Kieda, Dean of The Graduate School.

ABSTRACT

Modeling techniques are provided for accurate and efficient solution of near-field radiative heat transfer in complex, three-dimensional and multiscale geometries. These techniques are applied to investigate the physics of near-field thermal radiation in several configurations.

A closed-form expression based on fluctuational electrodynamics is derived and applied for modeling size effect on the emissivity of metallic and dielectric thin films. The emissivity of dielectric films increases with increasing film thickness, while metallic films show the inverse behavior. The critical thickness, above which no size effect is observed, is about a hundred nanometers for metals and a few centimeters for dielectrics.

A novel computational method, called the thermal discrete dipole approximation (T-DDA), for modeling near-field radiative heat transfer in arbitrary geometries is proposed and verified. The T-DDA is based on discretizing objects into cubical subvolumes behaving as electric point dipoles. The objects are submerged in an infinite lossless medium and can interact with an infinite surface. An extensive convergence analysis of the method is performed using the exact results for two spheres. The convergence of the T-DDA mostly depends on the dielectric function of the objects and the object size to gap ratio. An error less than 5% was achievable in the T-DDA using the available computational resources.

The T-DDA is applied to model near-field thermal radiation between a silica probe

and a silica surface separated by a gap of size d. When $d \to 0$, the probe-surface heat rate is dominated by the contribution of surface phonon-polaritons and approaches a d^{-2} power law. In this limit, the total heat rate and the resonance location can be predicted using the proximity approximation. When the probe tip size is comparable to the gap thickness, localized surface phonons also contribute to heat transfer and induce a resonance splitting in the thermal spectrum. In this regime, the spheroidal dipole approximation predicts the resonant frequencies accurately, and it provides a rough estimate of the heat rate. Finally, the T-DDA analysis of probe-sample interactions demonstrates that the resonance redshift observed in near-field thermal spectroscopy is caused by the reflection interactions between the probe and the sample.

TABLE OF CONTENTS

LIST OF TABLES

Tables

ACKNOWLEDGEMENTS

I would like to express my special appreciation to my advisor, Dr. Mathieu Francoeur. He has been an extremely supporting advisor for me during last five years. He is an excellent example of a dedicated researcher and teacher, and he is my role model for my future career.

My sincere thanks go to Dr. Martin Čuma. Without his constant help and guidance, I would not have been able to perform these large-scale simulations. I also thank Dr. Keunhan Park, Dr. Tim Ameel, and Dr. Fernando Guevara Vasquez who agreed to be a part of my Ph.D. committee. During my Ph.D., I was very lucky to work with my incredible fellow lab mates Michael Bernardi, John DeSutter, Spencer Petersen and Mitchell Short. I would like to express my gratitude to them for being amazing colleagues and friends. In addition, I acknowledge the Army Research Office and the Center for High Performance Computing at the University of Utah for providing financial and computational resources for my research project.

Most importantly, none of this would have been possible without the love and support of my family. My husband and best friend, Babak, has been a constant source of love, encouragement and strength during the last five years. My parents, Naser and Ziba, and my siblings, Homa, Siavash and Afrouz, have always supported me with love from thousands of miles away. I could not be luckier to have them in my life.

CHAPTER 1

INTRODUCTION

1.1 Near-field radiative heat transfer

Radiative heat transfer between bodies with characteristic lengths, i.e., size L and separation distance d, larger than the dominant thermal wavelength is referred to as the far-field regime of thermal radiation. The dominant thermal wavelength is predicted by Wien's law ($\lambda_{max}T = 2898$ μm·K [1]) and is approximately 10 μm at room temperature. In the far-field regime, radiative heat transfer is described by Planck's theory of heat radiation [2]. Two physical mechanisms are ignored in the Planck theory. First, thermal radiation is assumed to be incoherent such that wave interference is neglected. Second, the presence of evanescent waves is not accounted for. These mechanisms, which do not contribute in the far-field regime, become considerable when the characteristic lengths of the problem are comparable to or smaller than the thermal wavelength. In this case, the Planck theory ceases to be valid and radiative heat transfer is said to be in the near-field regime [1].

While thermal radiation in the far field is considered to be a surface phenomenon, near-field thermal radiation is a volumetric process. Thermal emission is due to the random motion of charged particles inside a body caused by thermal agitation at

a temperature greater than absolute zero. In the far-field regime where $L >> \lambda_{max}$, thermally generated waves emitted far from the object interface are internally absorbed and cannot escape the body. Indeed, thermal emission from the object is due to the contribution of a small portion of the volume located below the interface such that thermal emission is approximated as a surface phenomenon. When the size of the objects is comparable to or smaller than the contributing thin layer located below the interface, near-field thermal emission must be modeled as a volumetric and size-dependent process. Additionally, near-field radiative heat transfer can exceed the blackbody limit by several orders of magnitude and can be quasi-monochromatic [3-17]. The enhancement beyond Planck's distribution occurs when $d < \lambda_{max}$ and is due to the extraneous contribution to heat transport by waves evanescently confined within a distance of about a wavelength normal to the surface of a thermal source. These modes, as depicted in Fig. 1.1(a), include evanescent waves generated by total internal reflection of propagating waves at the material-gap interface (frustrated modes) as well as resonant surface waves such as surface phonon-polaritons and surface plasmon-polaritons [6]. These surface polaritons, with evanescent fields exponentially decaying on both sides of the material-gap interface, can lead to quasi-monochromatic heat exchange [6,18-22]. For example, the spectral heat flux between two bulks of silicon carbide (SiC) separated by a vacuum gap of thickness d is shown in Fig. 1.1(b) as a function of d and the angular frequency ω. One of the bulks is kept at $T_1 = 300$ K while the other one has a temperature of $T_2 = 0$ K. As shown in Fig. 1.1(b), the heat flux increases with decreasing gap size. While the increase in the near-field heat flux at ω_{res} is attributed to surface phonon-polaritons, the evanescent modes due to total internal reflection are responsible for the enhancement at other frequencies.

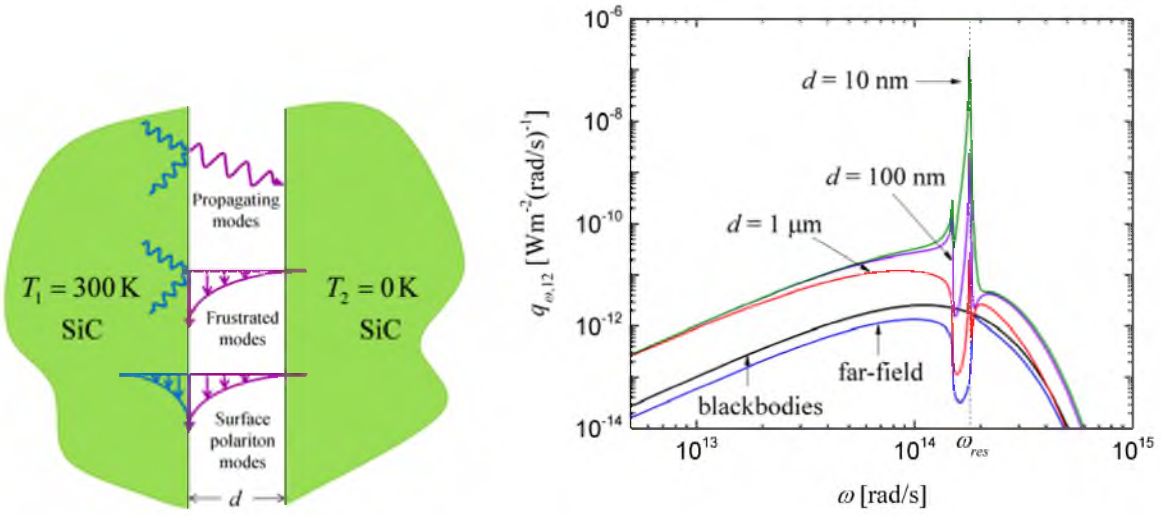

Figure 1.1 Radiative heat transfer between two bulks. (a) Two SiC bulks separated by a gap size d exchanging thermal radiation in the vacuum. (b) Spectral radiative heat flux for the configuration shown in part (a) as a function of the angular frequency and gap size.

Thermal radiation in the near field is modeled via fluctuational electrodynamics in which the Maxwell equations are augmented by stochastic current sources due to thermal agitation of charged particles [3]. The resulting equations are called the thermal stochastic Maxwell equations.

Near-field radiative heat transfer has recently attracted significant attention due to the advances in nanomanufacturing that allow fabrication of devices with sizes on the order of micro/nanometer. A clear understanding of near-field radiative heat transfer is necessary for thermal management of micro/nanoscale devices. Additionally, the unique properties of near-field radiative heat transfer can be exploited in many applications. Indeed, near-field thermal radiation may find application in imaging [23,24], spectroscopy [24-26], thermophotovoltaic power generation [27-32], tip-based nanomanufacturing [33-36], thermal management of electronic devices [37], thermal rectification through a vacuum gap [38,39], and radiative property control [40-42]. In

these applications, it is often required to predict near-field radiative heat transfer in complex, three-dimensional (3D) and multiscale geometries.

1.2 Modeling of near-field radiative heat transfer

Near-field radiative heat transfer predictions have been mainly restricted to simple canonical geometries. This is due to the fact that the vast majority of near-field thermal radiation problems have been solved by deriving analytical expressions for the dyadic Green's function (DGF) relating a source point $\mathbf{r}'$ to a field observed at $\mathbf{r}$; this approach is referred to as the DGF method. The DGF method provides exact solutions to near-field thermal radiation problems, but becomes intractable when dealing with 3D arbitrarily-shaped objects. Over the past years, the DGF approach has been applied to various cases: two bulks [4-6,43-47], two films [48-52], two structured surfaces [53], two nanoporous materials [54], one-dimensional (1D) layered media [55-57], a cylindrical cavity [58], two dipoles [59-61], two large spheres [62-64], dipole-surface [65-67], dipole-structured surface [68], sphere-surface [69,70], two long cylinders [71], two nanorods [72,73], two gratings [74] and N nanoparticles modeled as electric point dipoles [75].

Potential engineering systems capitalizing on near-field thermal radiation involve nontrivial geometries for which analytical solutions of the thermal stochastic Maxwell equations do not exist. Numerical methods should be used for modeling near-field thermal radiation in complex geometries. Prior to this research, there were only two available numerical methods for modeling near-field thermal radiation problems. These approaches, namely the finite-difference frequency-domain (FDFD) method [76] and the finite-difference time-domain (FDTD) method [77], are based on discretizing the

differential form of the thermal stochastic Maxwell equations in space and frequency (FDFD) or time (FDTD). The FDFD and FDTD methods require that both the objects and the free space be discretized, which is computationally expensive. So far, the FDTD method has been applied for modeling near-field thermal radiation in a few nanostructures [78-83]. Concurrent with this research, the boundary element method (BEM) [84] and a volume-discretization based method [85] were also proposed for modeling near-field thermal radiation problems. The BEM is based on the discretization of the boundary integral form of the thermal stochastic Maxwell equations, and is thus difficult to apply to inhomogeneous materials.

Additionally, many potential near-field thermal radiation applications [23-26,33-37] involve interactions between micro/nanosized objects and a large surface. Modeling near-field radiative heat transfer in this multiscale geometry is quite challenging. Analytical solutions do not exist except for a single sphere above an infinite surface [69,70]. Numerical methods [76,77,84,85] are also difficult to apply to this multiscale problem due to the prohibitive calculation time associated with discretizing a surface that is many orders of magnitude larger than the objects. The only formulation capable of handling nontrivial geometries and an infinite surface is based on a combination of the scattering-based approach and the boundary element method [86].

Modeling techniques are required to obtain an in-depth physical insight into near-field thermal radiation and to accelerate the development of its many potential applications. The objective of this dissertation is to provide accurate, efficient, and versatile modeling techniques for the solution of near-field thermal radiation in micro/nano and multiscale systems. These techniques are applied to investigate the

physics of radiative heat transfer in several geometries. The objective of the dissertation is fulfilled by deriving a closed-form expression for describing thermal emission from a common type of nanostructures, i.e., thin films. The closed-form solution is used to investigate the size effect on the emissivity of thin films. Analytical solutions are not available for near-field thermal radiation in complex, 3D, and multiscale geometries. A computational framework is established for large-scale simulations of near-field radiative heat transfer between arbitrary-shaped objects. The modeling challenge in multiscale geometries is addressed by treating the interactions of the objects and a surface analytically. The implemented computational framework is applied for investigating thermal radiation exchange in several configurations including a probe and an infinite surface. The probe-surface interaction is of great interest in tip-based imaging, spectroscopy, and nanomanufacturing techniques.

1.3 Organization of the dissertation

Thermal emission by nanostructures cannot be predicted via Planck's theory, since these structures have characteristic lengths that are smaller than the dominant thermal wavelength. Fluctuational electrodynamics should be used for modeling thermal emission by nanostructures. One of the most common types of nanostructures is a thin film. Thin films have many engineering applications, in solar cells, optical filters, and antireflection coatings, to name only a few [87]. For applications involving thermal effects, it is crucial to quantify thermal emission from thin layers. Thin films have a simple geometry and their thermal emission can be modeled analytically. In Chapter 2, a closed-form expression is derived for calculating the thickness-dependent emissivity of thin films. The

model is employed for predicting the spectral, hemispherical and total, hemispherical emissivities of a number of metals and dielectrics. The critical thickness above which no size effect is observed for metals and dielectrics is also studied.

Near-field radiative heat transfer between 3D complex-shaped objects, which cannot be treated analytically, is the topic of Chapter 3. This chapter describes a novel computational method called the thermal discrete dipole approximation (T-DDA) for simulating near-field radiative heat transfer between 3D arbitrarily-shaped objects. The T-DDA is inspired by the discrete dipole approximation (DDA) which is extensively used for predicting electromagnetic scattering by particles. The DDA is based on discretizing objects into cubical subvolumes behaving as electric point dipoles [88-92]. The T-DDA follows the same general procedure as the DDA, except that the dipole moments in the subvolumes are induced not only by an external illumination but also by thermally fluctuating dipoles arising from thermal agitation of charges. The T-DDA is verified against analytical results for two spheres separated by a subwavelength gap for various dielectric functions and separation distances.

In Chapter 4, the convergence of the T-DDA is investigated by comparison against the exact results for the two-sphere problem. The approximations associated with the T-DDA are discussed, and near-field radiative heat transfer between two spheres is studied for sphere sizes much smaller than, smaller than, and comparable to the wavelength. In each size regime, the T-DDA error is analyzed for various refractive indices and vacuum gap thicknesses. A nonuniform discretization scheme is proposed to reduce the computational requirement of the T-DDA.

The research presented in Chapter 5 is motivated by the fact that in many

applications, such as in near-field thermal microscopy [23-26], it is necessary to model the interactions between complex-shaped micro/nanosized objects and a surface. In this chapter, the presence of an infinite surface is integrated into the T-DDA formalism described in Chapter 3. The interactions between the objects and the surface are accounted for using the work of Sommerfeld who analyzed electric dipole radiation above an infinite surface [93]. The updated method is compared against the analytical solution of near-field radiative heat transfer between a sphere and a surface. The T-DDA with surface interaction is then employed to analyze radiative heat transfer between a probe and a surface in the near-field regime.

In Chapter 6, the T-DDA with surface interaction is applied to near-field thermal spectroscopy, which is a new technique for measuring the near-field thermal spectrum of a sample. In this technique, the near-field thermal spectrum from the sample is scattered in the far field using a subwavelength probing tip. The scattered thermal electromagnetic field is detected in the far field. Recently, two separate studies [25,26] reported that the resonant frequencies of the measured far-field signal are spectrally redshifted compared to the resonant frequencies of the near-field thermal spectrum of the sample. It is not clear if the resonance redshift is a physical phenomenon or an experimental artifact. The T-DDA, which does not neglect any physical aspect of the probe-sample interaction, is used for analyzing the potential resonance redshift. A further investigation of the resonance redshift is performed by analyzing the heat flux between the sample and a thin film.

A summary of the results obtained in this dissertation as well as the recommendations for future work are presented in Chapter 7.

1.4 References cited

[1] Howell J.R., Mengüç M.P. and Siegel R., *Thermal Radiation Heat Transfer*, CRC Press, Boca Raton, 6th Edition, 2015.

[2] Planck M., *The Theory of Heat Radiation*, Dover Publications, New York, 1991.

[3] Rytov S.M., Kravtsov Y.A. and Tatarskii V.I., *Principles of Statistical Radiophysics 3: Elements of Random Fields*, Springer, New York, 1989.

[4] Polder D. and Van Hove M., Theory of radiative heat transfer between closely spaced bodies, *Physical Review B* **4**(10), 3303-3314, 1971.

[5] Loomis J.J. and Maris H.J., Theory of heat transfer by evanescent electromagnetic waves, *Physical Review B* **50**(24), 18517-18524, 1994.

[6] Joulain K., Mulet J.-P., Marquier F., Carminati R. and Greffet J.-J., Surface electromagnetic waves thermally excited: Radiative heat transfer, coherence properties and Casimir forces revisited in the near field, *Surface Science Reports* **57**, 59-112, 2005.

[7] Biehs S.-A., Rousseau E. and Greffet J.-J., Mesoscopic description of radiative heat transfer at the nanoscale, *Physical Review Letters* **105**, 234301, 2010.

[8] Kittel A., Müller-Hirsch W., Parisi J., Biehs S.-A., Reddig D. and Holthaus M., Near-field radiative heat transfer in a scanning thermal microscope, *Physical Review Letters* **95**, 224301, 2005.

[9] Shen S., Narayanaswamy A. and Chen G., Surface phonon polaritons mediated energy transfer between nanoscale gaps, *Nano Letters* **9**(8), 2909-2913, 2009.

[10] Shen S., Mavrokefalos A., Sambegoro P. and Chen G., Nanoscale thermal radiation between two gold surfaces, *Applied Physics Letters* **100**, 233114, 2012.

[11] Hu L., Narayanaswamy A., Chen X.Y. and Chen G., Near-field thermal radiation between two closely spaced glass plates exceeding Planck's blackbody radiation law, *Applied Physics Letters* **92**, 133106, 2008.

[12] Rousseau E., Siria A., Jourdan G., Volz S., Comin F., Chevrier J. and Greffet J.-J., Radiative heat transfer at the nanoscale, *Nature Photonics* **3**(9), 514-517, 2009.

[13] Ottens R.S., Quetschke V., Wise S., Alemi A.A., Lundock R., Mueller G., Reitze D.H., Tanner D.B. and Whiting B.F., Near-field radiative heat transfer between macroscopic planar surfaces, *Physical Review Letters* **107**, 014301, 2011.

[14] Song B., Ganjeh Y., Sadat S., Thompson D., Fiorino A., Fernández-Hurtado V., Feist J., Garcia-Vidal F.J., Cuevas J.C., Reddy P. and Edgar M., Enhancement of near-field radiative heat transfer using polar dielectric thin films, *Nature Nanotechnology* **10**, 253–258 , 2015.

[15] Kim K., Song B., Fernández-Hurtado V., Lee W., Jeong W., Cui L., Thompson D.,

Feist J., Reid M.T.H., García-Vidal F.J., Carlos Cuevas J., Meyhofer E. and Reddy P., Radiative heat transfer in the extreme near field, *Nature* **528**, 387–391, 2015.

[16] Song B., Thompson D., Fiorino A., Ganjeh Y., Reddy P. and Meyhofer E., Radiative heat conductances between dielectric and metallic parallel plates with nanoscale gaps, *Nature Nanotechnology* **11**, 509–514, 2016.

[17] St-Gelais R., Zhu L., Fan S. and Lipson M., Near-field radiative heat transfer between parallel structures in the deep subwavelength regime, *Nature Nanotechnology* **11**, 515-519, 2016.

[18] Narayanaswamy A. and Chen G., Surface modes for near field thermophotovoltaics, *Applied Physics Letters* **82**(20), 3544-3546, 2003.

[19] Francoeur M., Mengüç M.P. and Vaillon R., Near-field radiative heat transfer enhancement via surface phonon polaritons coupling in thin films, *Applied Physics Letters* **93**, 043109, 2008.

[20] Mulet J.-P., Joulain K., Carminati R. and Greffet J-J., Enhanced radiative heat transfer at nanometric distances, *Nanoscale and Microscale Thermophysical Engineering* **6**, 209-222, 2002.

[21] Basu S., Lee B.J. and Zhang Z.M., Near-field radiation calculated with an improved dielectric function model for doped silicon, *ASME Journal of Heat Transfer* **132**, 023302, 2010.

[22] Rousseau E., Laroche M. and Greffet J.-J., Radiative heat transfer at nanoscale: Closed-form expression for silicon at different doping levels, *Journal of Quantitative Spectroscopy and Radiative Transfer* **111**, 1005-1014, 2010.

[23] De Wilde Y., Formanek F., Carminati R., Gralak B., Lemoine P.-A., Joulain K., Mulet J.-P., Chen Y. and Greffet J.-J., Thermal radiation scanning tunneling microscopy, *Nature* **444**, 740-743, 2006.

[24] Jones A.C. and Raschke M.B., Thermal infrared near-field spectroscopy, *Nano Letters* **12**, 1475-1481, 2012.

[25] Babuty A., Joulain K., Chapuis P.-O., Greffet J.-J. and De Wilde Y., Blackbody spectrum revisited in the near field, *Physical Review Letters* **110**, 146103, 2013.

[26] O'Callahan B.T., Lewis W.E., Jones A.C. and Raschke M.B., Spectral frustration and spatial coherence in thermal near-field spectroscopy, *Physical Review B* **89**, 245446, 2014.

[27] DiMatteo R.S., Greiff P., Finberg S.L., Young-Waithe K.A., Choy H.K.H., Masaki M.M. and Fonstad C.G., Enhanced photogeneration of carriers in a semiconductor via coupling across a nonisothermmal nanoscale vacuum gap, *Applied Physics Letters* **79**(12), 1894-1896, 2001.

[28] Whale M.D. and Cravalho E.G., Modeling and performance of microscale

thermophotovoltaic energy conversion devices, *IEEE Transactions on Energy Conversion* **17**(1), 130-142, 2002.

[29] Laroche M., Carminati R. and Greffet J-J., Near-field thermophotovoltaic energy conversion, *Journal of Applied Physics* **100**, 063704, 2006.

[30] Park K., Basu S., King W.P. and Zhang ZM. Performance analysis of near-field thermophotovoltaic devices considering absorption distribution, *Journal of Quantitative Spectroscopy and Radiative Transfer* **109**, 305-316, 2008.

[31] Francoeur M., Vaillon R., and Mengüç M.P., Thermal impacts on the performance of nanoscale-gap thermophotovoltaic power generators, *IEEE Transactions on Energy Conversion* **26**, 686-698, 2011.

[32] Bernardi M.P., Dupré O., Blandre E., Chapuis P.-O., Vaillon R. and Francoeur M., Impacts of propagating, frustrated and surface modes on radiative, electrical and thermal losses in nanoscale-gap thermophotovoltaic power generators, *Scientific Reports* **5**, 11626, 2015.

[33] Mamin H.J., Thermal writing using a heated atomic force microscope tip, *Applied Physics Letters* **69**, 433, 1996.

[34] Wilder K., Quate C.F., Adderton D., Bernstein R. and Elings V., Noncontact nanolithography using the atomic force microscope, *Applied Physics Letters* **73**, 2527, 1998.

[35] Hawes E.A., Hastings J.T., Crofcheck C. and Mengüç M.P., Spatially selective melting and evaporation of nanosized gold particles, *Optics Letters* **33**, 1383-1385, 2008.

[36] Loke V.L.Y. and Mengüç M.P., Surface waves and atomic force microscope probe-particle near-field coupling: discrete dipole approximation with surface interaction, *Journal of the Optical Society of America A* **27**(10), 2293-2203, 2010.

[37] Guha B., Otey C., Poitras C.B., Fan S. and Lipson M., Near-field radiative cooling of nanostructures, *Nano Letters* **12**, 4546-4550, 2012.

[38] Otey C.R., Lau W.T. and Fan S., Thermal rectification through vacuum, *Physical Review Letters* **104**, 154301, 2010.

[39] Basu S. and Francoeur M., Near-field radiative transfer based thermal rectification using doped silicon, *Applied Physics Letters* **98**, 113106, 2011.

[40] Greffet J.-J., Carminati R., Joulain K., Mulet J.-P., Mainguy S. and Chen Y., Coherent emission of light by thermal sources, *Nature* **416**, 61-64, 2002.

[41] Lee B.J., Wang L.P. and Zhang Z.M., Coherent thermal emission by excitation of magnetic polaritons between periodic strips and a metallic film, *Optics Express* **16**, 11328-11336, 2008.

[42] Francoeur M., Basu S. and Petersen S.J., Electric and magnetic surface polariton

mediated near-field radiative heat transfer between metamaterials made of silicon carbide particles, *Optics Express* **19**, 18774-18788, 2011.

[43] Francoeur M. and Mengüç M.P., Role of fluctuational electrodynamics in near-field radiative heat transfer, *Journal of Quantitative Spectroscopy and Radiative Transfer* **109**, 280-293, 2008.

[44] Basu S. and Zhang Z.M., Maximum energy transfer in near-field thermal radiation at nanometer distances, *Journal of Applied Physics* **105**, 093595, 2009.

[45] Fu C.J. and Zhang Z.M., Nanoscale radiation heat transfer for silicon at different doping levels, *International Journal of Heat and Mass Transfer* **49**, 1703-1718, 2006.

[46] Chapuis P.-O., Volz S., Henkel C., Joulain K. and Greffet J.-J., Effects of spatial dispersion in near-field radiative heat transfer between two parallel metallic surfaces, *Physical Review B* 77, 035431, 2008.

[47] Volokitin A.I. and Persson B.N.J., Radiative heat transfer between nanostructures, *Physical Review B* **63**, 205404, 2001.

[48] Francoeur M., Mengüç M.P. and Vaillon R., Spectral tuning of near-field radiative heat flux between two thin silicon carbide films, *Journal of Physics D: Applied Physics* **43**, 075501, 2010.

[49] Francoeur M., Mengüç M.P. and Vaillon R., Local density of electromagnetic states within a nanometric gap formed between two thin films supporting surface phonon polaritons, *Journal of Applied Physics* **107**, 034313, 2010.

[50] Francoeur M., Mengüç M.P. and Vaillon R., Control of near-field radiative heat transfer via surface phonon-polariton coupling in thin films, *Applied Physics A: Materials Science & Processing* **103**, 547-550, 2011.

[51] Francoeur M., Mengüç M.P. and Vaillon R., Coexistence of multiple regimes for near-field thermal radiation between two layers supporting surface phonon polaritons in the infrared, *Physical Review B* **84**, 075436, 2011.

[52] Ben-Abdallah P., Joulain K., Drevillon J. and Domingues G., Near-field heat transfer mediated by surface wave hybridization between two films, *Journal of Applied Physics* **106**, 044306, 2009.

[53] Biehs S.-A., Huth O. and Rüting F., Near-field radiative heat transfer for structured surfaces, *Physical Review B* **78**, 085414, 2008.

[54] Biehs S.-A., Ben-Abdallah P., Rosa F.S.S., Joulain K. and Greffet J.-J., Nanoscale heat flux between nanoporous materials, *Optics Express* **19**, A1088-A1103, 2011.

[55] Francoeur M., Mengüç M.P. and Vaillon R., Solution of near-field thermal radiation in one-dimensional layered media using dyadic Green's functions and the scattering matrix method, *Journal of Quantitative Spectroscopy and Radiative Transfer* **110**, 2002-2018, 2009.

[56] Narayanaswamy A. and Chen G., Direct computation of thermal emission from nanostructures, *Annual Reviews of Heat Transfer* **14**, 169-195, 2005.

[57] Zheng Z. and Xuan Y., Theory of near-field radiative heat transfer for stratified magnetic media, *International Journal of Heat and Mass Transfer* **54**, 1101-1110, 2011.

[58] Hammonds Jr. J.S., Thermal transport via surface phonon polaritons across a two-dimensional pore, *Applied Physics Letters* **88**, 041912, 2006.

[59] Domingues G., Volz S., Joulain K. and Greffet J.-J., Heat transfer between two nanoparticles through near field interaction, *Physical Review Letters* **94**, 085901, 2005.

[60] Chapuis P.-O., Laroche M., Volz S. and Greffet J.-J., Radiative heat transfer between metallic nanoparticles, *Applied Physics Letters* **92**, 201906, 2008.

[61] Chapuis P.-O., Laroche M., Volz S. and Greffet J.-J., Erratum: Radiative heat transfer between metallic nanoparticles, *Applied Physics Letters* **97**, 269903, 2010.

[62] Narayanaswamy A. and Chen G., Thermal near-field radiative transfer between two spheres, *Physical Review B* 77, 075125, 2008.

[63] Sasihithlu K. and Narayanaswamy A., Convergence of vector spherical wave expansion method applied to near-field radiative transfer, *Optics Express* **19**, 772-785, 2011.

[64] Sasihithlu K. and Narayanaswamy A., Proximity effects in radiative heat transfer, *Physical Review B* **83**, 161406(R), 2011.

[65] Mulet J.-P., Joulain K., Carminati R. and Greffet J.-J., Nanoscale radiative heat transfer between a small particle and a plane surface, *Applied Physics Letters* **78**(19), 2931-2933, 2001.

[66] Huth O., Rüting F., Biehs S.-A. and Holthaus M., Shape-dependence of near-field heat transfer between a spheroidal nanoparticle and a flat surface, *The European Physical Journal - Applied Physics* **50**, 10603, 2010.

[67] Biehs S.-A., Huth O., Rüting F. and Holthaus M., Spheroidal nanoparticles as thermal near-field sensors, *Journal of Applied Physics* **108**, 014312, 2010.

[68] Biehs S.-A. and Greffet J.-J., Near-field heat transfer between a nanoparticle and a rough surface, *Physical Review B* **81**, 245414, 2010.

[69] Krüger M., Emig T., and Kardar M., Nonequilibrium electromagnetic fluctuations: heat transfer and interactions, *Physical Review Letters* **106**, 210404, 2011.

[70] Otey C. and Fan S., Numerically exact calculation of electromagnetic heat transfer between a dielectric sphere and plate, *Physical Review B* **84**, 245431, 2011.

[71] Golyk V.A., Krüger M. and Kardar M., Heat radiation from long cylindrical objects, *Physical Review E* **85**, 046603, 2012.

[72] Carrillo C. and Bayazitoglu Y., Sphere approximation for nanorod near-field radiative heat exchange analysis, *Nanoscale and Microscale Thermophysical Engineering* **15**, 195-208, 2011.

[73] Carrillo L.Y. and Bayazitoglu, Nanorod near-field radiative heat exchange analysis, *Journal of Quantitative Spectroscopy and Radiative Transfer* **112**, 412-419, 2011.

[74] Biehs S.-A., Rosa F.S.S. and Ben-Abdallah P., Modulation of near-field heat transfer between two gratings, *Applied Physics Letters* **98**, 243102, 2011.

[75] Messina R., Tschikin M., Biehs S.-A., and Ben-Abdallah P., Fluctuation-electrodynamic theory and dynamics of heat transfer in systems of multiple dipoles, *Physical Review* B **88**, 104307, 2013.

[76] Wen S.-B., Direct numerical simulation of near field thermal radiation based on Wiener chaos expansion of thermal fluctuating current, *ASME Journal of Heat Transfer* **132**, 072704, 2010.

[77] Rodriguez A.J., Ilic O., Bermel P., Celanovic I., Joannopoulos J.D., Soljacic M. and Johnson S.G., Frequency-selective near-field radiative heat transfer between photonic crystal slabs: A computational approach for arbitrary geometries and materials, *Physical Review Letters* **107**, 114302, 2011.

[78] Liu B. and Shen S., Broadband near-field radiative thermal emitter/absorber based on hyperbolic metamaterials: Direct numerical simulation by the Wiener chaos expansion method, *Physical Review B* **87**, 115403, 2013.

[79] Datas A., Hirashima D. and Hanamura K., FDTD simulation of near-field radiative heat transfer between thin films supporting surface phonon polaritons: Lessons learned, *Journal of Thermal Science and Technology* **8**, 91-105, 2013.

[80] Didari A. and Mengüç M.P., Analysis of near-field radiation transfer within nano-gaps using FDTD method, *Journal of Quantitative Spectroscopy and Radiative Transfer* **146**, 214-226, 2014.

[81] Didari A. and Mengüç M.P., Near-field thermal emission between corrugated surfaces separated by nano-gaps, *Journal of Quantitative Spectroscopy and Radiative Transfer* **158**, 43-51, 2015.

[82] Didari A. and Mengüç M.P., Near- to far-field coherent thermal emission by surfaces coated by nanoparticles and the evaluation of effective medium theory, *Optics Express* **23**, A547-A552, 2015.

[83] Didari A. and Mengüç M.P., Near-field thermal radiation transfer by mesoporous metamaterials, *Optics Express* **23**, A1253-A1258, 2015.

[84] Rodriguez A.W., Reid M.T.H. and Johnson S.G, Fluctuating surface-current formulation of radiative heat transfer for arbitrary geometries, *Physical Review B* **86**, 220302(R), 2012.

[85] Polimeridis A.G., Reid M.T.H., Jin W., Johnson S.G., White J.K. and Rodriguez A.W., Fluctuating volume-current formulation of electromagnetic fluctuations in inhomogeneous media: Incandescence and luminescence in arbitrary geometries, *Physical Review B* **92**, 134202, 2015.

[86] McCauley A.P., Reid M.T.H., Krüger M. and Johnson S.G., Modeling near-field radiative heat transfer from sharp objects using a general three-dimensional numerical scattering technique, *Physical Review B* **85**, 165104, 2012.

[87] Zhang Z.M, *Micro/Nanoscale Heat Transfer*, McGraw-Hill, New York, 2007.

[88] Draine B.T., The discrete-dipole approximation and its application to interstellar graphite grains, *The Astrophysical Journal* **333**, 848-872, 1988.

[89] Draine B.T. and Flatau P.J., Discrete-dipole approximation for scattering calculations, *Journal of the Optical Society of America A* **11**, 1491-1499, 1994.

[90] Schmehl R., *The coupled-dipole method for light scattering from particles on plane surfaces*, MS Thesis, Arizona State University, 1994.

[91] Yurkin M.A. and Hoekstra A.G., The discrete dipole approximation: An overview and recent developments, *Journal of Quantitative Spectroscopy and Radiative Transfer* **106**, 558-589, 2007.

[92] Loke V.L.Y., Mengüç M.P. and Nieminen T.A., Discrete-dipole approximation with surface interaction: Computational toolbox for MATLAB, *Journal of Quantitative Spectroscopy and Radiative Transfer* **112**, 1711-1725, 2011.

[93] Sommerfeld A., On the propagation of waves in wireless telegraphy, *Annals of Physics* **81**, 1135, 1926.

CHAPTER 2

SIZE EFFECT ON THE EMISSIVITY OF THIN FILMS

Reprinted from Journal of Quantitative Spectroscopy and Radiative Transfer, 118, S. Edalatpour and M. Francoeur, Size effect on the emissivity of thin films, 75-85,

Journal of Quantitative Spectroscopy & Radiative Transfer 118 (2013) 75–85

Contents lists available at SciVerse ScienceDirect

Journal of Quantitative Spectroscopy & Radiative Transfer

journal homepage: www.elsevier.com/locate/jqsrt

Size effect on the emissivity of thin films

Sheila Edalatpour*, Mathieu Francoeur*

Radiative Energy Transfer Lab, Department of Mechanical Engineering, University of Utah, Salt Lake City, UT 84112, USA

ARTICLE INFO

Article history:
Received 9 August 2012
Received in revised form
4 December 2012
Accepted 18 December 2012
Available online 28 December 2012

Keywords:
Emissivity
Thin films
Size effect
Fluctuational electrodynamics

ABSTRACT

The size effect on the emissivity of thin films is analyzed. There are three methods for calculating film emissivity: the indirect method, the direct method based on the division of amplitude and the direct method based on Maxwell's equations combined with fluctuational electrodynamics. Traditional indirect approaches involve computation of absorption, and the emissivity is then predicted by invoking Kirchhoff's law. The direct method employed in this work, based on Maxwell's equations and fluctuational electrodynamics, does not require Kirchhoff's law. Instead, Kirchhoff's law emerges naturally from the mathematical model. A closed form expression for thickness-dependent emissivity of thin films is derived from the direct approach, and it is shown that the three existing methods lead to the same aforementioned expression. Simulation results reveal that the emissivity of metallic films increases above bulk values as the film thickness decreases. This counterintuitive behavior is due to the extraneous contributions of waves experiencing multiple reflections within the thin layer, which are usually internally absorbed for metallic bulks. Conversely, for dielectrics, the emissivity of films decreases as the film thickness decreases due to a loss of source volume. The critical thickness above which no size effect is observed for metals is about a hundred of nanometers, while it can be as large as a few centimeters for dielectrics. A simple approximate expression is finally suggested for evaluating the critical thickness; this criterion can be used as a quick reference to determine if the size effect on the emissivity of thin films should be considered.

1. Introduction

Thin films are employed in numerous engineering devices such as solar cells, optical filters and antireflection coatings [1]. In applications involving heat transfer and electromagnetic wave propagation, knowledge of the radiative properties of thin layers is crucial. Emissivity is a surface radiative property defined as the ratio of the emissive power of a surface to that of a blackbody at the same condition [2,3]. The concept of emissivity thus implies that thermal emission is a surface phenomenon. However, in reality, thermal radiation emission is a volumetric process that can often be approximated as a surface process. Waves leaving the surface of an emitting body are the result of various phenomena such as emission, absorption, transmission, and reflection. These phenomena occur throughout the entire volume of the emitter. On the other hand, only a small portion of volume below the emitting surface contributes significantly to the emitted spectrum; this small portion is defined as the critical thickness. The emissivity of a film with a thickness equal or greater than the critical thickness is referred to as the bulk emissivity. If the emitting medium is thinner than the critical thickness, the concept of emissivity, as defined in the classical theory of thermal radiation, is not valid anymore such that emissivity data reported in the literature may not be applicable to such thin layers.

* Corresponding authors. Tel.: +1 801 581 5721; fax: +1 801 585 9825.
E-mail addresses: sheila.edalatpour@utah.edu (S. Edalatpour), mfrancoeur@mech.utah.edu (M. Francoeur).

0022-4073/$ - see front matter © 2012 Elsevier Ltd. All rights reserved.
http://dx.doi.org/10.1016/j.jqsrt.2012.12.012

Nomenclature

c_0	speed of light in vacuum ($=2.998\times10^8$ m s^{-1})
e	electron charge ($=1.6022\times10^{-19}$ J eV^{-1})
E	wave energy ($=\hbar\omega/e$) (eV)
$\mathbf{E}$	electric field (V/m)
$\mathbf{H}$	magnetic field (A/m)
$\hbar$	reduced Planck's constant ($=1.0546\times10^{-34}$ J s)
i	complex constant ($=(-1)^{1/2}$)
$I_{b,\omega}$	spectral intensity of a blackbody (W m^{-2} sr^{-1} (rad/s)$^{-1}$)
I_ω	spectral intensity (W m^{-2} sr^{-1} (rad/s)$^{-1}$)
$\mathbf{J}'$	stochastic current density vector (A m^{-2})
k	magnitude of wavevector ($=k'+ik''$) (rad m^{-1})
k_B	Boltzmann constant ($=1.3807\times10^{-23}$ J K^{-1})
k_ρ	parallel component of wavevector (rad m^{-1})
k_x	x-component of wavevector (rad m^{-1})
k_z	normal component of wavevector (rad m^{-1})
k_v	magnitude of wavevector in vacuum (rad m^{-1})
$\mathbf{k}$	wavevector (rad m^{-1})
q''	total, hemispherical emissive power (W m^{-2})
q''_b	total, hemispherical emissive power of a blackbody (W m^{-2})
$q''_{b,\omega}$	spectral, hemispherical emissive power of a blackbody (W m^{-2} (rad/s)$^{-1}$)
q''_ω	spectral, hemispherical emissive power (W m^{-2} (rad/s)$^{-1}$)
r_{ij}	Fresnel's reflection coefficients at interface i–j
R_j	reflection coefficient of medium j
S_z	z-component of Poynting vector (W m^{-2})
t	time (s)
t_1	film thickness (m)
t_{cr}	critical thickness (m)
t^*_{cr}	approximate critical thickness (m)
t_{ij}	Fresnel's transmission coefficients at interface i–j
T	temperature (K)
T_j	transmission coefficient of medium j

Greek symbols

α	total, hemispherical absorptivity
α'_ω	spectral, directional absorptivity
δ_λ	radiation penetration depth (m)
ε	total, hemispherical emissivity
ε_∞	high frequency dielectric constant
ε_r	dielectric function ($=\varepsilon'_r+i\varepsilon''_r$)
ε_ω	spectral, hemispherical emissivity
ε'_ω	spectral, directional emissivity
ε_0	vacuum permittivity ($=8.854\times10^{-12}$ F m^{-1})
γ	polarization state
Γ	damping factor (s^{-1})
κ	imaginary part of refractive index
λ	wavelength (m)
Θ	mean energy of a Planck oscillator (J)
ρ, θ, z	polar coordinates
σ	Stefan–Boltzmann constant ($=5.67\times10^{-8}$ W m^{-2} K^{-4})
τ'_ω	spectral, directional transmissivity
ω	angular frequency (rad s^{-1})
ω_{LO}	longitudinal optical phonon frequency (rad s^{-1})
ω_p	plasma frequency (rad s^{-1})
ω_{TO}	transverse optical phonon frequency (rad s^{-1})

In this case, a thickness-dependent film emissivity can be defined as the emissive power of the layer to that of a blackbody at the same condition.

Indirect and direct methods have been proposed in the literature for predicting the emissivity of thin films. In the indirect method, the spectral, directional absorptivity α'_ω of the layer is calculated via a conservation of energy: $\alpha'_\omega=1-\rho'_\omega-\tau'_\omega$. In this expression, ρ'_ω and τ'_ω are the spectral, directional reflectivity and spectral, directional transmissivity, respectively, calculated by considering that the layer is illuminated by an external wave with specific frequency and direction. The spectral, directional emissivity ε'_ω is then determined by invoking Kirchhoff's law, which states that the spectral, directional emissivity equals the spectral, directional absorptivity for a body in thermodynamic equilibrium [2,3]. Wang et al. [4] recently used this approach to predict the emissivity of a Fabry–Perot cavity resonator. McMahon [5] proposed a direct method where the film is sub-divided into emitting elements. Radiation emitted by each element is traced within the layer in order to determine the portion transmitted outside the film. The emissive power is then computed by integrating over the layer thickness the contribution of each element. This approach, however, treats thermal radiation as incoherent such that possible interference effects are not accounted for. Consequently, the method cannot be applied to problems where the thickness of the film is of the same order of magnitude as the radiation wavelength, since interference effects play a non-negligible role in this case. Pigeat et al. [6] generalized McMahon's approach by considering wave interferences using the division of amplitude method. The authors claim that the method is applicable for estimating the emissivity of materials with inhomogeneities of the same order of magnitude as, or greater than, the radiation wavelength. However, the method has been tested only for homogeneous media. Shih and Andrews [7] applied this method to calculate the emissivity of an oil layer on water. Wang et al. [8] employed a direct method based on Maxwell's equations and fluctuational electrodynamics to model thermal emission from a layered medium with nonuniform temperature, and they demonstrated numerically the equivalence of indirect and direct approaches. Other papers in the literature studied thermal radiation emission from complex nanostructures, such as photonic crystals [9–11].

The objective of this paper is to investigate the size effect on the emissivity of thin films using a direct approach.

This direct model, based on Maxwell's equations and fluctuational electrodynamics [12], leads to a simple closed-form expression for computing the thickness-dependent emissivity of films. It is shown that this equation can also be derived from the other methods, thus demonstrating the equivalence of the three approaches proposed in the literature. The thickness-dependent emissivity equation is applied to investigate the size effect on the emissivity of a number of metals and dielectrics. For each material, the variation of emissivity against film thickness is calculated, and the critical thickness above which no size effect is observed is determined. Based on this analysis, an approximate expression is proposed for determining the critical thickness without performing extensive computations.

This paper is organized as follows. The problem under consideration, the underlying assumptions and the mathematical description are provided in Sections 2 and 3. Thickness-dependent emissivities for various metals and dielectrics are reported in Section 4 along with values of critical thicknesses. Finally, concluding remarks are provided. The equivalence between the direct approaches is rigorously demonstrated in Appendix A.

2. Description of the problem

Emissivity is calculated using a direct approach based on Maxwell's equations combined with fluctuational electrodynamics [3,12–16]. The specific problem under consideration is shown in Fig. 1. A film, denoted as medium 1, of thickness of t_1 and described by a frequency-dependent dielectric function $\varepsilon_{r1}(\omega)=\varepsilon'_{r1}(\omega)+i\varepsilon''_{r1}(\omega)$ is coated on a substrate referred to as medium 0. The layered medium, with perfectly smooth and parallel interfaces, is infinite along the ρ-direction and azimuthally symmetric. The emitting film at temperature T is assumed to be in local thermodynamic equilibrium, homogenous, isotropic, and non-magnetic. Room temperature emissivity is analyzed, such that T is fixed at 293 K. The wavevector $\mathbf{k}$ and its normal (k_z) and parallel (k_ρ) components with respect to the interfaces are shown in Fig. 1. The wavevector represents the periodicity of the wave in space and provides its direction of propagation. The parallel component of the wavevector k_ρ is a pure real number and is the same in all media [1]. However, since the wavevector varies with the dielectric function of the medium, the normal component of the wavevector k_z is different from one medium to another [17].

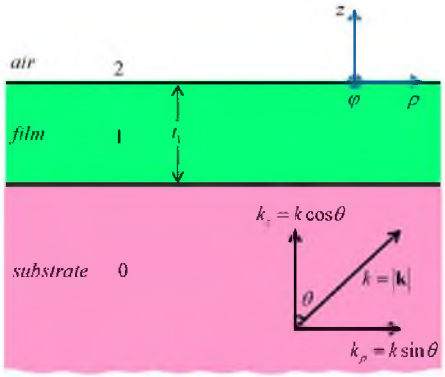

Fig. 1. Schematic representation of the problem: A thin film (medium 1) coated on a substrate (medium 0) is emitting in air (medium 2).

3. Mathematical formulation

Direct calculation of thermal emission is based on the fluctuational electrodynamics formalism introduced by Rytov [12]. According to Rytov's description, thermal emission is the result of random fluctuations of charges within a medium due to thermal agitation. Fluctuational electrodynamics is built on a macroscopic level, and the microscopic charge oscillations are modeled macroscopically via a stochastic current density $\mathbf{J}^r$. Since fluctuational electrodynamics is a macroscopic theory based on fluctuations around an equilibrium temperature, it is applicable to bodies in local thermodynamic equilibrium. Fluctuational electrodynamics may also be applied to non-equilibrium conditions provided that the energy emitted by the body is much greater than the energy required to maintain steady-state conditions [12].

The propagation of thermally generated electromagnetic waves is described by Maxwell's equations supplemented by the stochastic current $\mathbf{J}^r$ acting as a source term. Due to the fact that the current density is a stochastic variable, the Maxwell equations combined with fluctuational electrodynamics are also stochastic. After solving the stochastic Maxwell equations, the electromagnetic fields at the film surface are known, so that the emitted radiative heat flux can be calculated via the time-averaged Poynting vector. Since the film is infinite along the ρ-direction and symmetric with respect to the azimuthal angle φ, only the z-component of the time-averaged Poynting vector needs to be calculated [18]:

$$q''_{z,\omega}(z)=\mathbf{4}\cdot\frac{1}{2}\mathrm{Re}\left\{\left\langle E_\rho H^*_\varphi - E_\varphi H^*_\rho\right\rangle\right\} \tag{3.1}$$

It should be noted that the Poynting vector is four times larger than its customary definition, since only positive frequencies are taken into account in the Fourier decomposition of the time-dependent fields [1].

In order to calculate the radiative heat flux, it is necessary to correlate the stochastic current $\mathbf{J}^r$ to the local temperature of the medium. This link is provided by the fluctuation-dissipation theorem (FDT). Under the assumptions listed in Section 2, the FDT can be written as [12]:

$$\left\langle \left|J^r_\alpha(\mathbf{r},\omega)\right|^2\right\rangle = \frac{\omega\varepsilon_0\varepsilon''_r(\omega)}{\pi}\Theta(\omega,T) \tag{3.2}$$

where the subscript α refers to orthogonal components, and $\langle\ \rangle$ indicates an ensemble average. The term $\Theta(\omega,T)$, which is the mean energy of an electromagnetic state at frequency ω and temperature T, is the "driving force" for thermal emission and is given by [1]:

$$\Theta(\omega,T)=\frac{\hbar\omega}{\exp\left(\hbar\omega/k_B T\right)-1} \tag{3.3}$$

The spectral, hemispherical emissive power of the film is determined by solving the stochastic Maxwell equations using dyadic Green's functions for layered media [18,19]. The resulting expression is given by [20]:

$$q''_\omega = \frac{\Theta(\omega,T)}{4\pi^2}\int_0^{k_v} k_\rho dk_\rho \sum_{\gamma=TE,\ TM} \frac{\left(1-|r_{21}^\gamma|^2\right)a^\gamma - 4\mathrm{Im}(r_{21}^\gamma)b^\gamma}{\left|1-r_{01}^\gamma r_{21}^\gamma e^{2ik_{z1}t_1}\right|^2} \tag{3.4a}$$

where

$$a^\gamma = e^{-2k''_{z1}t_1}\left[|r_{01}^\gamma|^2\left(1-e^{-2k''_{z1}t_1}\right)-\left(1-e^{2k''_{z1}t_1}\right)\right] \tag{3.4b}$$

$$b^\gamma = e^{-2k''_{z1}t_1}\mathrm{Im}\left[r_{01}^\gamma\left(1-e^{2ik'_{z1}t_1}\right)\right] \tag{3.4c}$$

where k_v is the magnitude of wavevector in vacuum, γ represents the polarization state of the wave (TE: transverse electric and TM: transverse magnetic), and r_{ij}^γ is the Fresnel reflection coefficient at the interface i–j in polarization state γ. Fresnel's reflection coefficients are calculated as follows for non-magnetic materials [21]:

$$r_{ij}^{TE} = \frac{k_{zi}-k_{zj}}{k_{zi}+k_{zj}} \tag{3.5a}$$

$$r_{ij}^{TM} = \frac{\varepsilon_{rj}k_{zi}-\varepsilon_{ri}k_{zj}}{\varepsilon_{rj}k_{zi}+\varepsilon_{ri}k_{zj}} \tag{3.5b}$$

The numerator on the right-hand side of Eq. (3.4a) represents emission by the film, while the denominator accounts for multiple wave reflections and interference within the layer. The summation in the integrand is performed over both TE and TM polarization states, while the integration over k_ρ can be interpreted physically as an integration over the polar angle θ ($k_\rho = k_v \sin\theta$).

After some manipulation, Eq. (3.4a) can be re-written as [20]:

$$q''_\omega = \frac{\Theta(\omega,T)}{4\pi^2}\int_0^{k_v} k_\rho dk_\rho \sum_{\gamma=TE,\ TM}\left(1-|R_1^\gamma|^2-|T_1^\gamma|^2\right) \tag{3.6a}$$

where

$$|R_1^\gamma|^2 = \left|\frac{r_{21}^\gamma + r_{10}^\gamma e^{2ik_{z1}t_1}}{1+r_{21}^\gamma r_{10}^\gamma e^{2ik_{z1}t_1}}\right|^2 \tag{3.6b}$$

$$|T_1^{TE}|^2 = \frac{\mathrm{Re}(k_{z0})}{\mathrm{Re}(k_{z2})}\left|\frac{t_{21}^{TE}t_{10}^{TE}e^{ik_{z1}t_1}}{1+r_{21}^{TE}r_{10}^{TE}e^{2ik_{z1}t_1}}\right|^2 \tag{3.6c}$$

$$|T_1^{TM}|^2 = \frac{\mathrm{Re}(k_{z0}/\varepsilon_{r0})}{\mathrm{Re}(k_{z2}/\varepsilon_{r2})}\frac{|\varepsilon_{r0}|}{|\varepsilon_{r2}|}\left|\frac{t_{21}^{TM}t_{10}^{TM}e^{ik_{z1}t_1}}{1+r_{21}^{TM}r_{10}^{TM}e^{2ik_{z1}t_1}}\right|^2 \tag{3.6d}$$

In Eqs. (3.6c) and (3.6d), t_{ij}^γ is the Fresnel transmission coefficient at the interface i-j in polarization state γ calculated as follows for non-magnetic materials [21]:

$$t_{ij}^{TE} = \frac{2k_{zi}}{k_{zi}+k_{zj}} \tag{3.7a}$$

$$t_{ij}^{TE} = \frac{2\varepsilon_{rj}k_{zi}}{\varepsilon_{rj}k_{zi}+\varepsilon_{ri}k_{zj}}\sqrt{\frac{\varepsilon_{ri}}{\varepsilon_{rj}}} \tag{3.7b}$$

The terms R_1^γ and T_1^γ, given by Eqs. (3.6b) through (3.6d), are the field amplitude reflection and transmission coefficients for the film. The square of the magnitude of these coefficients, $|R_1^\gamma|^2$ and $|T_1^\gamma|^2$, represents the spectral, directional reflectivity and spectral, directional transmissivity of layer 1, respectively. Accordingly, in Eq. (3.6a), the term $1-|R_1^\gamma|^2-|T_1^\gamma|^2$ can be interpreted as the spectral, directional absorptivity of the film. From Eqs. (3.6b) through (3.6d), it can be seen that for a bulk, where t_1 goes to infinity, R_1^γ and T_1^γ reduce to r_{21}^γ and 0, respectively. Therefore, the spectral, directional absorptivity of a bulk material in polarization state γ is $\alpha_\omega^\gamma = 1-|r_{21}^\gamma|^2$.

3.1. Spectral, directional emissivity

The spectral, directional emissivity of the film is the ratio of its actual spectral, directional emissive power to that of a blackbody at the same condition [2]:

$$\varepsilon'_\omega = \frac{I_\omega}{I_{b,\omega}} \tag{3.8}$$

where I_ω and $I_{b,\omega}$ are the spectral intensities of the film and a blackbody, respectively. In order to determine an equation for the radiative intensity from Eq. (3.6a), the following expression relating the spectral, hemispherical emissive power to the spectral intensity is employed [2]:

$$q'_\omega = 2\pi\int_{\theta=0}^{\pi/2} I_\omega \cos\theta\sin\theta\, d\theta \tag{3.9}$$

where azimuthal symmetry is assumed (i.e., the integration over φ from 0 to 2π has been performed). By comparing Eq. (3.9) with Eq. (3.6a), and noting that $k_\rho = k_v\sin\theta$, the spectral intensity I_ω can be written as:

$$I_\omega = \Theta(\omega,T)\frac{\omega^2}{8\pi^3c_0^2}\sum_{\gamma=TE,TM}\left(1-|R_1^\gamma|^2-|T_1^\gamma|^2\right) \tag{3.10}$$

The spectral blackbody intensity is given by Planck's distribution [2]:

$$I_{b,\omega} = \Theta(\omega,T)\frac{\omega^2}{4\pi^3c_0^2} \tag{3.11}$$

Taking the ratio of Eqs. (3.10) and (3.11), the following expression for the spectral, directional emissivity is determined:

$$\varepsilon'_\omega = \frac{1}{2}\sum_{\gamma=TE,TM}\left(1-|R_1^\gamma|^2-|T_1^\gamma|^2\right) \tag{3.12}$$

Eq. (3.12) shows that for bodies in local thermodynamic equilibrium, the spectral, directional emissivity is equal to the spectral, directional absorptivity. In other words, Eq. (3.12) is Kirchhoff's law that has been rigorously derived from Maxwell's equations and fluctuational electrodynamics. This relation also implies that the direct and indirect methods are conceptually equivalent. Additionally, it is shown in Appendix A that the direct method based on the division of amplitude [6] also results in the same expression. Therefore, it can be concluded that all the three methods employed in the literature are equivalent. For a bulk material, Eq. (3.12)

reduces to:

$$\varepsilon'_\omega = \frac{1}{2}\sum_{\gamma=TE,TM}\left(1-|r^\gamma_{21}|^2\right) \tag{3.13}$$

3.2. Spectral, hemispherical emissivity

The spectral, hemispherical emissivity of the film is the ratio of its actual spectral, hemispherical emissive power to that of a blackbody at the same condition [2]:

$$\varepsilon_\omega = \frac{q''_\omega}{q''_{b,\omega}} \tag{3.14}$$

where q''_ω is calculated from Eq. (3.6a), and $q''_{b,\omega}$ $(=\pi I_{b\omega})$ is the spectral, hemispherical emissive power of a blackbody. The spectral, hemispherical emissivity can thus be written as:

$$\varepsilon_\omega = \frac{k_y^2}{2}\int_0^{k_y} k_\rho dk_\rho \sum_{\gamma=TE,\,TM}\left(1-|R^\gamma_1|^2-|T^\gamma_1|^2\right) \tag{3.15}$$

3.3. Total, hemispherical emissivity

The total, hemispherical emissivity of the film is defined as the ratio of its actual total, hemispherical emissive power to that of a blackbody at the same condition [2]:

$$\varepsilon = \frac{q''}{q''_b} \tag{3.16}$$

The total, hemispherical emissive power of a blackbody is given by the Stefan–Boltzmann law ($q''_b = n_2^2\sigma T^4$, where n_2 is the refractive index of medium 2), while the total emissive power of the film, q'', is obtained by integrating Eq. (3.6a) over all frequencies:

$$q'' = \int_0^\infty q'_\omega d\omega \tag{3.17}$$

Note that the integrals in Eqs. (3.6a) and (3.17) are solved numerically via a fifth order accurate Boole integration rule.

4. Results

4.1. Verification of the model

The method described in Section 3 is verified against results reported by Nayaranaswamy and Chen [9] and by Pigeat et al. [6]. The spectral, hemispherical emissivity of silver (Ag) is calculated for a 10-nm-thick film and for a bulk in the spectral band of from 0.4 μm to 4 μm. For these simulations, the dielectric function of Ag is assumed to be $5.17+i-9.013^2/(E(E+i0.018))$, where E is the wave energy in electron volt (eV) and is equal to $2\pi c_0\hbar(e\lambda)^{-1}$. The results from the current method and those from Ref. [9] are compared in Fig. 2(a), where a good agreement between both sets of results is observed. Additionally, the spectral, normal emissivity of a diamond film deposited on a silicon substrate is calculated at a wavelength of 2.3 μm for various film thicknesses. The film temperature is assumed to be 1073 K. The refractive indices of diamond and silicon used in the model are $1.45+i0.13$ and $2.65+i0.08$, respectively. The results of the current method are compared against those from Ref. [6] in Fig. 2(b), where, again, a good agreement is observed.

4.2. Analysis of spectral, hemispherical emissivity

The spectral, hemispherical emissivity of films is investigated for various metals (gold (Au), silver (Ag), aluminum (Al), copper (Cu)) and dielectrics (silicon carbide (SiC), cubic boron nitride (cBN)). From now on, the substrate is assumed to be a lossless medium with a frequency-independent unit dielectric function. The emissivity is calculated in the spectral band from 2.2×10^{13} rad/s to 6.9×10^{14} rad/s where more than 99% of the blackbody emissive power is contained at room temperature [2]. The frequency-dependent dielectric function of metals is approximated via a Drude model [1,22]:

$$\varepsilon_r(\omega) = 1-\frac{\omega_p^2}{\omega(\omega+i\Gamma)} \tag{4.1}$$

where ω_p is the plasma frequency and Γ is the damping factor. These parameters are reported in Table 1 for Au, Ag, Al and Cu.

The frequency-dependent dielectric function of dielectric materials is modeled using a damped harmonic oscillator [22,23]:

$$\varepsilon_r(\omega) = \varepsilon_\infty\left(\frac{\omega^2-\omega_{LO}^2+i\Gamma\omega}{\omega^2-\omega_{TO}^2+i\Gamma\omega}\right) \tag{4.2}$$

where ε_∞ is the high frequency dielectric constant, and ω_{LO} and ω_{TO} are the frequencies of longitudinal and transverse optical phonons, respectively. These parameters are listed in Table 1 for SiC and cBN.

The spectral, hemispherical emissivity and emissive power of Au are shown in Fig. 3(a) and (b), respectively, for various film thicknesses; the results are compared against bulk predictions.

As it can be seen from Fig. 3(a), the emissivity does not vary significantly with frequency ω. However, the emissivity decreases significantly when the thickness of the film increases until it converges to the emissivity of the bulk. For a 81-nm-thick film, the difference between the emissivity of the film and the bulk is less than 1% for all frequencies; this thickness above which the emissivity does not exhibit any size effect is called the critical thickness t_{cr}. The counterintuitive behavior of the spectral, hemispherical emissivity reported for Au was also observed for Ag, Al and Cu (results not shown).

The spectral, hemispherical emissivity and emissive power of SiC are shown in Fig. 4(a) and (b), respectively, for various film thicknesses; the results are again compared against bulk predictions.

Conversely to the case of metals, the emissivity decreases when decreasing the thickness of the emitter. According to Wien's law ($\lambda_{max}T=2898$ μm K) [2,3], the dominant emitted wavelength for a body at 293 K is about 10 μm (corresponds to a frequency of 1.88×10^{14} rad/s). Since wave interference becomes important when the film thickness is approximately equal to the wavelength [25], some oscillations of the emissivity are observed when the thickness of the film corresponds to the dominant emitted wavelength of 10 μm. The dip in emissivity between ω_{LO} and ω_{TO} is due to the fact that the real part of the dielectric constant is negative in that bandwidth, thus resulting in a region of high reflection. Note also that surface phonon-polaritons,

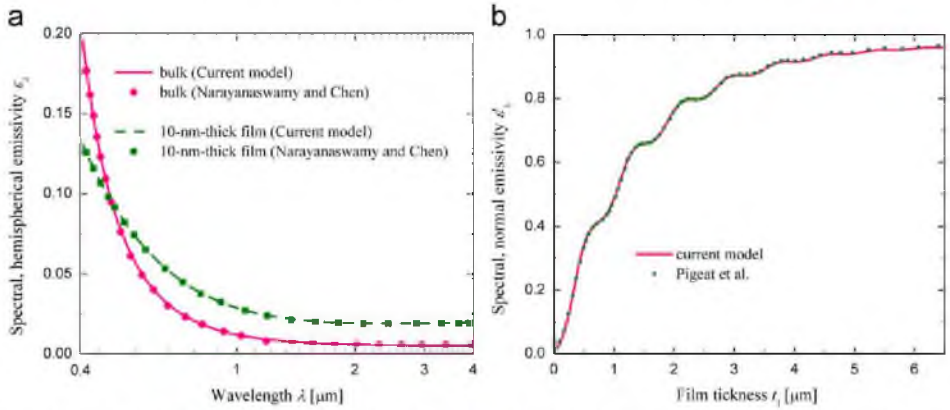

Fig. 2. Comparison between the direct method and the results from Refs. [6,9]: (a) spectral, hemispherical emissivity of a 10-nm-thick Ag film and a bulk of Ag, and (b) spectral, normal emissivity of a diamond layer deposited on a silicon substrate.

Table 1
Parameters used for calculating the dielectric functions of metals (see Eq. (4.1)) and dielectrics (see Eq. (4.2)).

Materials	ε_∞ (–)	ω_{LO} (10^{14} rad/s)	ω_{TO} (10^{14} rad/s)	Γ (10^{11} s^{-1})	ω_p (10^{15} rad/s)
Metals					
Au [22]	–	–	–	405	13.71
Ag [22]	–	–	–	273	13.69
Al [22]	–	–	–	1243	22.42
Cu [22]	–	–	–	138	11.23
Dielectrics					
SiC [23]	6.7	1.494	1.825	8.966	–
cBN [24]	4.46	1.985	2.451	9.934	–

resulting in quasi-monochromatic heat exchange in the near field, exist within that spectral band [20]. Here, the critical thickness t_{cr} is estimated to be 6 cm. Note that the conclusions stated for the case of SiC are also applicable for cBN (results not shown).

The opposite trends observed for metals and dielectrics may be interpreted by analyzing the film interface reflectivity and internal absorption. Bulk metals are generally poor thermal emitters in the spectral band of interest. According to Kirchhoff's law, emissivity is equal to absorptivity, and thus the absorptivity of metals is also low in this frequency band. For a bulk of metal where the energy can only be reflected and absorbed (no transmission), the reflectivity ρ is equal to $1-\alpha$, where α is the absorptivity. Since α is low, the reflectivity of metals is high. The low absorptivity of a metallic surface, however, does not mean that metals are internally poor absorbers. Indeed, the imaginary part of the refractive index, κ, is high in metals [3], such that they internally absorb radiation transmitted at their interface within approximately a hundred of nanometers. In Fig. 5, the path of a wave emitted inside a metal is schematically shown for a thin and a thick film. The emitted wave propagates in the film until it is incident at the film-air interface, where a portion of the wave is transmitted in air, while the remaining portion is reflected back in the film. Since metals are good reflectors, the reflected portion is considerable. The probability of a reflected wave to come back again at the film-air interface is less likely in the thicker film than in the thinner one. This is due to the fact that the wave has to travel a longer distance in the thicker film in order to come back at the film-air interface, and since metals are internally highly absorptive, the wave is likely to be internally absorbed. On the other hand, the thicker film has a greater source volume (see Fig. 5(b)). However, this extraneous source volume, which is far away from the film-air interface, does not play a significant role in thermal radiation emission due to high internal absorption within the metal. Therefore, the emissivity of metals increases as the film thickness decreases because of the supplementary contribution of waves experiencing multiple reflections at the film interfaces.

Comparing the emissivity of a bulk of SiC and a bulk of Au, it is obvious that the reflectivity of dielectrics is not as large as that of metals. Additionally, the imaginary part of the refractive index of dielectrics is generally much smaller than for metals, such that dielectrics are internally poorly absorptive. Therefore, the contribution from waves experiencing multiple reflections within dielectrics exists in both thin and thick films, and is nearly unaffected by the size of the layer. Additionally, the waves emitted by the extraneous source volume within a thicker film are not significantly attenuated in dielectrics, such that they have a strong effect on the emissivity. As a consequence, the emissivity of dielectric films is a pure volumetric phenomenon.

4.3. Analysis of total, hemispherical emissivity

The total, hemispherical emissivity versus the film thickness of all materials reported in Table 1 is shown in Fig. 6.

By increasing the size of a metal film, its emissivity decreases rapidly such that it reaches the bulk value for a thickness of about 100 nm. Inversely, the emissivity of dielectric films increases with increasing the layer thickness, and the speed of convergence to the bulk emissivity is much

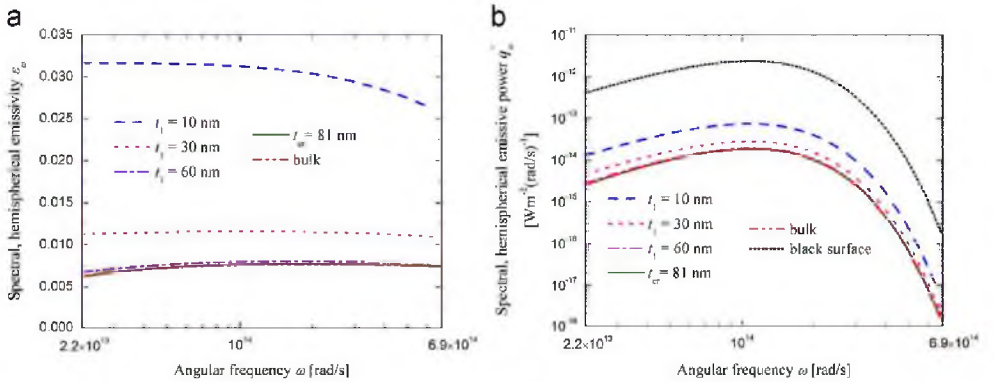

Fig. 3. Spectral, hemispherical: (a) emissivity, and (b) emissive power of an Au film for various thicknesses.

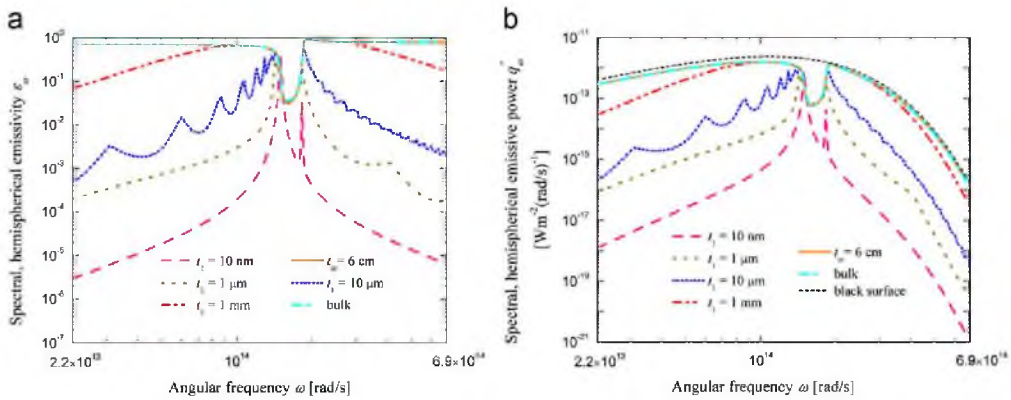

Fig. 4. Spectral, hemispherical: (a) emissivity, and (b) emissive power of a SiC film for various thicknesses.

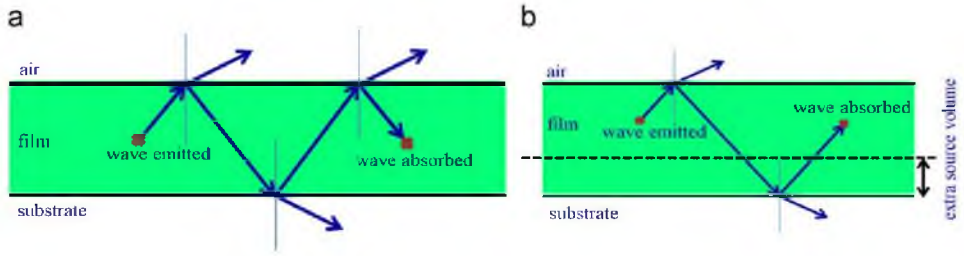

Fig. 5. Wave propagation in : (a) thin film, and (b) thick film.

slower than for metals. As a result, a film as thick as a few centimeters is required for the film emissivity to be 99% of the bulk emissivity. Note that the non-monotonic variations of emissivity observed for film thicknesses between 10 nm and 300 nm are due to surface phonon-polariton coupling within the SiC and cBN layers [20]. It can also be seen in Fig. 6 that the emissivity of a metal bulk is generally much smaller than the bulk emissivity of dielectrics. However, for thicknesses below approximately 500 nm, the emissivity of metals can exceed the emissivity of dielectrics.

4.4. Critical thickness

Table 2 shows critical thicknesses for Au, Ag, Al, Cu, SiC and cBN based on spectral, hemispherical and total, hemispherical emissivities. The critical thicknesses are calculated for two levels of accuracy: 1% and 0.1%. The 1% accuracy means that the critical thickness is reached if the difference between film and bulk emissivities is less than 1%; the same explanation holds for the 0.1% accuracy. Note that the results provided in Table 2

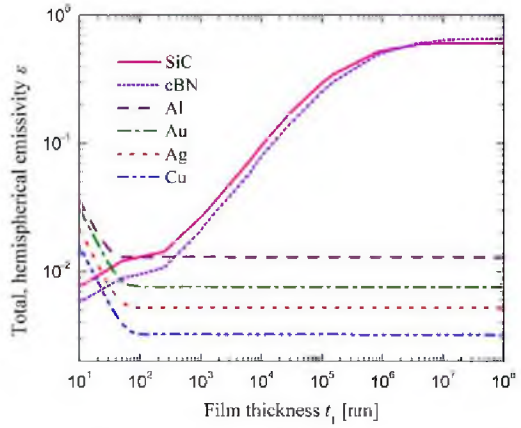

Fig. 6. Total, hemispherical emissivity of various materials as a function of the film thickness.

Table 2
Critical thicknesses of films.

Materials	Critical thickness t_{cr} (nm)			
	1% accuracy		0.1% accuracy	
	ε_ω	ε	ε_ω	ε
Metals				
Au	81	80	129	104
Ag	81	81	149	107
Al	116	47	135	87
Cu	99	99	133	133
Dielectrics				
SiC	6.0×10^7	9.1×10^6	9.2×10^7	3.0×10^7
cBN	11.3×10^7	1.7×10^7	17.2×10^7	4.7×10^7

are valid at room temperature, as the emission spectrum and dielectric function are temperature-dependent.

As expected, the critical thickness based on the spectral, hemispherical emissivity is larger than the critical thickness based on the total, hemispherical emissivity. Indeed, in the former case, the spectral emissivity should satisfy the accuracy condition at each frequency. As discussed previously, the critical thickness of metals is about a hundred of nanometers, while it is as large as a few centimeters for dielectrics. These results suggest that special care should be taken when dealing with dielectric films. Indeed, while a dielectric layer with a thickness of a few millimeters is considered as physically thick, it may exhibit size effect.

It is helpful to have a simple criterion for evaluating the critical thickness. In this way, one can determine quickly if the size effect on the emissivity of film should be accounted for. Two approximations are often used in the literature for this purpose [1]. The first approximation assumes the critical thickness to be equal to the wavelength of radiation. Based on the calculated values of critical thickness, it is found that this approximation may be unreliable. Indeed, using the Wien wavelength, this method would suggest that a layer with thickness of 10 μm does not exhibit size effect. The results of Table 2 show clearly that this is not the case. Another criterion suggests that the critical thickness is approximately equal to the coherence length. This approximation is difficult to apply in practice, because the coherence length of a blackbody cannot be easily determined. As a first order approximation, it is possible to estimate the coherence length equal to the Wien wavelength [25]. Again, this method is not in agreement with the rigorous approach proposed in this work.

An approximated critical thickness, denoted by t_{cr}^*, can be determined using the radiation penetration depth δ_λ [26]. According to Beer's law [2], the energy of a wave is exponentially attenuated along its path: $I_i/I_0=\exp(-d/\delta_\lambda)$, where $\delta_\lambda=\lambda/4\pi\kappa$, d is the distance traveled along the propagation direction, I_i is the intensity of the wave after a travel path d and I_0 is the initial intensity. Therefore, the distance through which the intensity of the wave is absorbed by a specific ratio I_i/I_0 can be calculated as:

$$d=-\ln(I_i/I_0)\,\delta_\lambda \tag{4.3}$$

Eq. (4.3) can be used to determine the location of the farthest emitting dipoles having non-negligible contribution to far-field emission; this location thus corresponds to the critical thickness t_{cr}^*. The contribution of an emitting dipole can be ignored when the intensity of the radiated wave by that dipole at the film-air interface is a negligible fraction of its initial intensity. This fraction can take different values based on the desired accuracy. In this paper, t_{cr} has been calculated for two accuracy levels (1% and 0.1%). The same levels of accuracy are used for predicting t_{cr}^*. Therefore, t_{cr}^* can be expressed via the following general expression:

$$t_{cr}^*=-\ln(Ac)\,\delta_\lambda \tag{4.4}$$

where Ac is the desired accuracy.

The values of t_{cr} and t_{cr}^* for the materials investigated in this paper are presented and compared in Table 3. Since the critical thicknesses t_{cr} based on spectral, hemispherical emissivity are compared with t_{cr}^*, the largest t_{cr}^* in the thermal spectrum at room temperature is reported in Table 3.

It can be seen in Table 3 that t_{cr} and t_{cr}^* are of the same order of magnitude for both accuracy levels. The maximum relative difference between t_{cr} and t_{cr}^* is about 30%. Consequently, Eq. (4.4) provides a reasonable approximation for the thickness above which no size effect on the emissivity of thin film is observed.

5. Conclusions

The objective of this paper was to study the size effect on the emissivity of thin films. This was accomplished via a direct model based on the solution of Maxwell's equations combined with fluctuational electrodynamics. The closed-form expression obtained for the thickness-dependent emissivity demonstrated the validity of Kirchhoff's law from a mathematical standpoint. The model was employed for predicting the behavior of spectral, hemispherical and total, hemispherical emissivities of a number of metals and dielectrics. The results showed that the emissivity of dielectrics decreases with decreasing the layer thickness, while the emissivity of metals increases with decreasing the film thickness. The counterintuitive behavior observed for metals

Table 3
Comparison between the critical thickness calculated via Maxwell's equations and fluctuational electrodynamics, t_{cr}, against the approximate critical thickness, t_{cr}^{*}, evaluated via Eq. (4.4). Critical thicknesses are calculated at room temperature.

Materials	1% accuracy			0.1% accuracy		
	t_{cr} (nm)	t_{cr}^{*} (nm)	$\frac{\lvert(t_{cr}^{*}-t_{cr})\rvert}{t_{cr}}\times 100$ (%)	t_{cr} (nm)	t_{cr}^{*} (nm)	$\frac{\lvert(t_{cr}^{*}-t_{cr})\rvert}{t_{cr}}\times 100$ (%)
Metals						
Au	81	85	4.9	129	127	1.6
Ag	81	71	12.3	149	106	28.9
Al	116	96	17.2	135	144	6.7
Cu	99	69	30.3	133	104	21.8
Dielectrics						
SiC	6.0×10^{7}	6.5×10^{7}	8.3	9.2×10^{7}	9.7×10^{7}	5.4
cBN	11.3×10^{7}	12.2×10^{7}	8.0	17.2×10^{7}	18.3×10^{7}	6.4

is due to the extraneous contribution from waves experiencing multiple reflections within the thin film. For dielectrics, the size effect on the emissivity is a pure volumetric phenomenon, such that decreasing the source volume for thermal radiation emission decreases the emissivity. Simulation results also revealed that the critical thickness above which no size effect is observed for metals and dielectrics have different orders of magnitude. In metals, the critical thickness is about a hundred of nanometers, while it is as large as a few centimeters in dielectrics. Finally, a simple expression based on the radiation penetration depth was suggested for estimating the critical thickness without performing extensive numerical simulations. In a future research effort, the case of a film coated on a lossy substrate will be considered.

Appendix A. Equivalence of direct methods based on division of amplitude and Maxwell's equations combined with fluctuational electrodynamics

The objective of this Appendix is to demonstrate via a rigorous mathematical derivation that the direct method based on division of amplitude [6] is equivalent to the direct method based on Maxwell's equations and fluctuational electrodynamics [12]. For this purpose, an expression for the spectral, directional emissivity of the film is derived starting from the division of amplitude method.

In the division of amplitude approach discussed in Ref. [6], the film is discretized into volume elements, considered as independent and incoherent radiative sources. Waves emitted by each volume element are then traced within the film in order to determine the portion transmitted in air (medium 2). This transmitted energy is finally normalized by the blackbody radiation to obtain the film emissivity.

The traveling paths of two waves emitted by a volume element (dV) located at a distance d along the z-axis are depicted in Fig. A.1. One of the waves is emitted along the z-positive direction (upward wave), while the other wave is emitted along the z-negative direction (downward wave). The total field transmitted in air due to emission by this volume element is the summation of the contributions from upward and downward waves. Without loss of generality, it is assumed in the following derivation that the waves are traveling in the x–z plane.

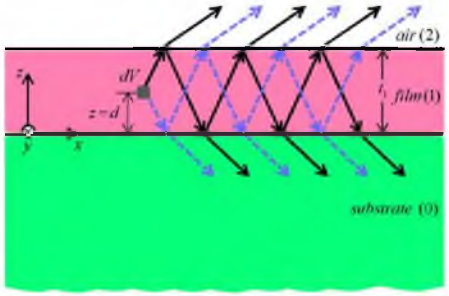

Fig. A.1. Schematic representation of the division of amplitude method. Solid and dashed lines show the path of upward and downward emitted waves, respectively.

A.1. Poynting vector in TE polarization

By tracing the path of the upward wave, it is possible to find an expression for the electric field transmitted in air in TE polarization:

$$\begin{aligned}\mathbf{E}_2^{u}=\hat{\mathbf{y}}E_{y2}^{u}=\hat{\mathbf{y}}E_2e^{-i\omega t}e^{ik_x x}\\ \times\Big(t_{12}^{TE}e^{ik_{z1}(t_1-d)}+t_{12}^{TE}e^{ik_{z1}(t_1-d)}r_{12}^{TE}r_{10}^{TE}e^{2ik_{z1}t_1}\\ +t_{12}^{TE}e^{ik_{z1}(t_1-d)}\left(r_{12}^{TE}\right)^2\left(r_{10}^{TE}\right)^2e^{4ik_{z1}t_1}+\ldots\Big)\end{aligned}\tag{A.1}$$

where the superscript u refers to an upward emitted wave. The electric field E_{y2}^{u} can be written as an infinite geometric series:

$$E_{y2}^{u}=E_2t_{12}^{TE}e^{-i\omega t}e^{ik_x x}e^{ik_{z1}(t_1-d)}\sum_{m=0}^{\infty}\left(r_{12}^{TE}\right)^m\left(r_{10}^{TE}\right)^me^{2mik_{z1}t_1}\tag{A.2}$$

The geometric series on the right-hand side of Eq. (A.2) converges to:

$$\sum_{m=0}^{\infty}\left(r_{12}^{TE}\right)^m\left(r_{10}^{TE}\right)^me^{2mik_{z1}t_1}=\frac{1}{1-r_{12}^{TE}r_{10}^{TE}e^{2ik_{z1}t_1}}\tag{A.3}$$

Substitution of Eq. (A.3) into Eq. (A.2) leads to the following TE-polarized electric field for the upward emitted wave:

$$E_{y2}^{u}=E_2e^{-i\omega t}e^{ik_x x}e^{ik_{z1}(t_1-d)}\frac{t_{12}^{TE}}{1-r_{12}^{TE}r_{10}^{TE}e^{2ik_{z1}t_1}}\tag{A.4}$$

Similarly, the electric field emerging in air due to a downward emitted wave is:

$$E_{y2}^{d} = E_2 e^{-i\omega t} e^{ik_x x} e^{ik_{z1}(t_1+d)} \frac{t_{12}^{TE} r_{10}^{TE}}{1-r_{12}^{TE} r_{10}^{TE} e^{2ik_{z1}t_1}} \tag{A.5}$$

where the superscript d refers to downward emitted wave. The total electric field in air due to a volume element dV is the sum of Eqs. (A.4) and (A.5):

$$E_{y2} = E_{y2}^{u} + E_{y2}^{d} = E_2 e^{-i\omega t} e^{ik_x x} e^{ik_{z1}t_1} \times \left(e^{-ik_{z1}d} + r_{10}^{TE} e^{ik_{z1}d}\right) \frac{t_{12}^{TE}}{1-r_{12}^{TE} r_{10}^{TE} e^{2ik_{z1}t_1}} \tag{A.6}$$

The x- and z-components of the magnetic field are related to the y-component of the electric field via Maxwell's equations [17]:

$$H_{x2} = -\frac{k_{z2}}{\omega} E_{y2} \tag{A.7a}$$

$$H_{z2} = \frac{k_x}{\omega} E_{y2} \tag{A.7b}$$

Note that it is assumed in the above equations that the materials are non-magnetic ($\mu_i = 1$).

In this paper, only the z-component of the Poynting vector in medium 2 (air) is of interest:

$$S_{z2} = E_{x2} H_{y2}^{*} - E_{y2} H_{x2}^{*} \tag{A.8}$$

where the superscript * refers to complex conjugate. Substituting Eq. (A.7a) into Eq. (A.8) provides the TE-polarized Poynting vector due to emission by a volume element dV:

$$S_{z2}^{TE,dV} = \frac{k_{z2}''}{\omega} |E_{y2}|^2 \tag{A.9}$$

The Poynting vector due to emission by the entire film is calculated by integrating Eq. (A.9) over the film thickness:

$$S_{z2}^{TE} = \int_0^{t_1} S_{z2}^{TE,dV} dz = \frac{k_{z2}''}{\omega} \int_0^{t_1} |E_{y2}|^2 dz \tag{A.10}$$

Substitution of E_{y2} given by Eq. (A.6) into Eq. (A.10) leads to the following expression for the Poynting vector in TE polarization after performing the integration:

$$S_{z2}^{TE} = \frac{E_2^2 k_{z2}''}{\omega} \frac{|t_{12}^{TE}|^2}{|1-r_{12}^{TE} r_{10}^{TE} e^{2ik_{z1}t_1}|^2} \left(\frac{a^{TE}}{2k_{z1}''} + \frac{b^{TE}}{k_{z1}'}\right) \tag{A.11}$$

where the coefficients a and b are given by Eqs. (3.4b) and (3.4c), respectively.

A.2. Poynting vector in TM polarization

Using the same procedure as for the TE-polarized case, the electric field in TM polarization due to upward and downward emitted waves is given by:

$$\mathbf{E}_2 = E_{x2}\hat{\mathbf{x}} + E_{z2}\hat{\mathbf{z}} = \frac{E_2}{k_2}\left(-k_{z2}\hat{\mathbf{x}} + k_x\hat{\mathbf{z}}\right) e^{-i\omega t} e^{ik_x x} e^{ik_{z1}t_1} \times \left(e^{-ik_{z1}d} + r_{10}^{TM} e^{ik_{z1}d}\right) \frac{t_{12}^{TM}}{1-r_{12}^{TM} r_{10}^{TM} e^{2ik_{z1}t_1}} \tag{A.12}$$

The magnetic field H_{y2} can be calculated in terms of the x-component of the electric field using Maxwell's equations:

$$H_{y2} = \frac{\omega\varepsilon_{r2}}{k_{z2}} E_{x2} \tag{A.13}$$

The Poynting vector in TM polarization due to emission by a volume element dV is calculated by substituting Eq. (A.13) into Eq. (A.8):

$$S_{z2}^{TM,dV} = \frac{\omega\varepsilon_{r2}''}{k_{z2}^{*}} |E_{x2}|^2 \tag{A.14}$$

Using Eq. (A.12), and performing the spatial integration of Eq. (A.14) over t_1, the Poynting vector due to the emission by the entire film is given by:

$$S_{z2}^{TM} = \frac{E_2^2 \omega \varepsilon_{r2}'' k_{z2}}{|k_2|^2} \frac{|t_{12}^{TM}|^2}{|1-r_{12}^{TM} r_{10}^{TM} e^{2ik_{z1}t_1}|^2} \left(\frac{a^{TM}}{2k_{z1}''} + \frac{b^{TM}}{k_{z1}'}\right) \tag{A.15}$$

A.3. Spectral, directional emissivity

The spectral, directional emissivity is calculated as the ratio of the actual spectral, directional emissive power of the film to that of a blackbody at the same condition. For a given polarization state γ, the spectral, directional emissivity is calculated as follows [6]:

$$\varepsilon_{\omega}^{\gamma} = \left\langle \frac{S_{z2}^{\gamma}}{S_{z2,b}^{\gamma}} \right\rangle \tag{A.16}$$

where $\langle\rangle$ indicates a time average. The spectral, directional emissivity of the film is determined by averaging spectral, directional emissivity over the two polarization states:

$$\varepsilon_{\omega}' = \frac{1}{2}\left(\varepsilon_{\omega}'^{TE} + \varepsilon_{\omega}'^{TM}\right) \tag{A.17}$$

The Poynting vectors in TE and TM polarizations due to blackbody radiation are [6]:

$$S_{z2,b}^{TE} = \frac{E_2^2 k_{z1}''}{2\omega k_{z1}'} \tag{A.18a}$$

$$S_{z2,b}^{TM} = \frac{E_2^2 \omega \varepsilon_{r1}'' k_{z1}}{2|k_1|^2 k_{z1}''} \tag{A.18b}$$

The spectral, directional emissivity in TE polarization is obtained by substituting Eqs. (A.11) and (A.18a) into Eq. (A.16):

$$\varepsilon_{\omega}'^{TE} = 2k_{z1}'' \mathrm{Re}\left\{\frac{k_{z2}}{k_{z1}}\right\} \frac{|t_{12}^{TE}|^2}{|1-r_{12}^{TE} r_{10}^{TE} e^{2ik_{z1}t_1}|^2} \left(\frac{a^{TE}}{2k_{z1}''} + \frac{b^{TE}}{k_{z1}'}\right) \tag{A.19}$$

Eq. (A.19) can be re-arranged using $\mathrm{Re}\{k_{z2}/k_{z1}\}|t_{12}^{TE}|^2 = 1-|r_{12}^{TE}|^2$ [22]:

$$\varepsilon_{\omega}'^{TE} = \frac{\left(1-|r_{12}^{TE}|^2\right) a^{TE} + 2k_{z1}''/k_{z1}' \left(1-|r_{12}^{TE}|^2\right) b^{TE}}{|1-r_{12}^{TE} r_{10}^{TE} e^{2ik_{z1}t_1}|^2} \tag{A.20}$$

Additionally, it is possible to show that:

$$k_{z1}''/k_{z1}' \left(1-|r_{12}^{TE}|^2\right) = -2\mathrm{Im}\{r_{12}^{TE}\} \tag{A.21}$$

The spectral, directional emissivity in TE polarization is finally determined by substituting Eq. (A.21) into

Eq. (A.20):

$$\varepsilon'^{TE}_{\omega} = \frac{\left(1-\left|r^{TE}_{12}\right|^2\right)a^{TE} - 4\mathrm{Im}\{r^{TE}_{12}\}b^{TE}}{\left|1-r^{TE}_{12}r^{TE}_{10}e^{2ik_{z1}t_1}\right|^2} \tag{A.22}$$

Following the same procedure as for the TE-polarized case, an expression for the spectral, directional emissivity of the film in TM polarization is determined by substituting Eqs. (A.15) and (A.18b) into Eq. (A.16):

$$\varepsilon'^{TM}_{\omega} = 2k''_{z1}\frac{|k_1|^2}{|k_2|^2}\mathrm{Re}\left\{\frac{\varepsilon^*_{r2}k_{z2}}{\varepsilon^*_{r1}k_{z1}}\right\}\frac{|t^{TM}_{12}|^2}{\left|1-r^{TM}_{12}r^{TM}_{10}e^{2ik_{z1}t_1}\right|^2}\left(\frac{a^{TM}}{2k'_{z1}}+\frac{b^{TM}}{k'_{z1}}\right) \tag{A.23}$$

where

$$\mathrm{Re}\left\{\frac{\varepsilon^*_{r2}k_{z2}}{\varepsilon^*_{r1}k_{z1}}\right\} = \mathrm{Re}\left\{\frac{\varepsilon_{r2}k^*_{z2}}{\varepsilon_{r1}k^*_{z1}}\right\} \tag{A.24a}$$

and

$$\frac{|k_1|^2}{|k_2|^2} = \frac{|\varepsilon_{r1}|}{|\varepsilon_{r2}|} \tag{A.24b}$$

Substituting Eqs. (A.24a) and (A.24b) into Eq. (A.23) leads to:

$$\varepsilon'^{TM}_{\omega} = 2k''_{z1}\frac{|\varepsilon_{r1}|}{|\varepsilon_{r2}|}\mathrm{Re}\left\{\frac{\varepsilon_{r2}k^*_{z2}}{\varepsilon_{r1}k^*_{z1}}\right\}\frac{|t^{TM}_{12}|^2}{\left|1-r^{TM}_{12}r^{TM}_{10}e^{2ik_{z1}t_1}\right|^2}\left(\frac{a^{TM}}{2k'_{z1}}+\frac{b^{TM}}{k'_{z1}}\right) \tag{A.25}$$

Equation. (A.25) can be simplified via the identity $|\varepsilon_{r1}|/|\varepsilon_{r2}|\ \mathrm{Re}\{\varepsilon_{r2}k^*_{z2}/\varepsilon_{r1}k^*_{z1}\}|t^{TM}_{12}|^2 = 1-|r^{TM}_{12}|^2$ [22]:

$$\varepsilon'^{TM}_{\omega} = \frac{\left(1-\left|r^{TM}_{12}\right|^2\right)a^{TM} + 2k'_{z1}/k'_{z1}\left(1-\left|r^{TM}_{12}\right|^2\right)b^{TM}}{\left|1-r^{TM}_{12}r^{TM}_{10}e^{2ik_{z1}t_1}\right|^2} \tag{A.26}$$

Using the identity given by Eq. (A.21), the spectral, directional emissivity in TM polarization has the exact same form as the spectral, directional emissivity in TE polarization:

$$\varepsilon'^{TM}_{\omega} = \frac{\left(1-\left|r^{TM}_{12}\right|^2\right)a^{TM} - 4\mathrm{Im}\{r^{TM}_{12}\}b^{TM}}{\left|1-r^{TM}_{12}r^{TM}_{10}e^{2ik_{z1}t_1}\right|^2} \tag{A.27}$$

Finally, the spectral, directional emissivity of the film is determined by substituting Eqs. (A.22) and (A.27) into Eq. (A.17):

$$\varepsilon'_{\omega} = \frac{1}{2}\sum_{\gamma=TE,TM}\frac{\left(1-\left|r^{\gamma}_{12}\right|^2\right)a^{\gamma} - 4\mathrm{Im}\{r^{\gamma}_{12}\}b^{\gamma}}{\left|1-r^{\gamma}_{12}r^{\gamma}_{10}e^{2ik_{z1}t_1}\right|^2} \tag{A.28}$$

After some manipulations outlined in reference [20], Eq. (A.28) reduces to Eq. (3.12) derived from Maxwell's equations and fluctuational electrodynamics. It is therefore possible to conclude that the direct method of Ref. [6] is equivalent to the direct approach employed in this work.

References

[1] Zhang ZM. Micro/Nanoscale Heat Transfer. New York: McGraw-Hill; 2007.
[2] Modest MF. Radiative Heat Transfer. 2nd ed.. San Diego: Academic Press; 2003.
[3] Howell JR, Siegel R, Mengüç MP. Thermal Radiation Heat Transfer. 5th ed.. New York: Taylor and Francis; 2010.
[4] Wang LP, Basu S, Zhang ZM. Direct measurement of thermal emission from a Fabry–Perot Cavity resonator. J Heat Transfer 2012;134:072701.
[5] McMahon HO. Thermal radiation from partially transparent reflecting bodies. J Opt Soc Am 1950;40:376–80.
[6] Pigeat P, Rouxel D, Weber B. Calculation of thermal emissivity for thin films by a direct method. Phys Rev B 1998;57:9293–300.
[7] Shih WC, Andrews AB. Modeling of thickness dependent infrared adiance contrast of native and crude oil covered water surfaces. Opt Express 2008;16:10535–42.
[8] Wang LP, Basu S, Zhang ZM. Direct and indirect methods for calculating thermal emission from layered structures with nonuniform temperatures. J Heat Transfer 2011;133:072701.
[9] Narayanaswamy A, Chen G. Thermal emission control with one-dimensional metallodielectric photonic crystals. Phys Rev B 2004;70:125101.
[10] Luo C, Narayanaswamy A, Chen G, Joannopoulos JD. Thermal radiation from photonic crystals: a direct calculation. Phys Rev Lett 2004;93:213905.
[11] Chan DLC, Soljačić M, Joannopoulos JD. Direct calculation of thermal emission for three-dimensionally periodic photonic crystal slabs. Phys Rev E 2006;74:036615.
[12] Rytov SM, Kravtsov YA, Tatarskii VI. Principles of statistical radiophysics 3: elements of random fields.Berlin, Heidelbergs, NewYork: Springer; 1989.
[13] Polder D, van Hove M. Theory of radiative heat transfer between closely spaced bodies. Phys Rev B 1971;4:3303–14.
[14] Basu S, Zhang ZM, Fu CJ. Review of near-field thermal radiation and its application to energy conversion. Int J Energy Res 2009;33:1202–32.
[15] Joulain K. Radiative transfer on short length scales.Topics in applied physics: microscale and nanoscale heat transfer, vol. 107. Berlin/Heidelberg: Springer; 2007 107–131.
[16] Joulain K, Mulet JP, Marquier F, Carminati R, Greffet JJ. Surface electromagnetic waves thermally excited: radiative heat transfer, coherence properties and Casimir forces revisited in the near field. Surf Sci Rep 2005;57:59–112.
[17] Balanis CA. Advanced Engineering Electromagnetics. 2nd ed.New York: John Wiley and Sons; 2012.
[18] Francoeur M. Near-field radiative transfer: Thermal radiation, thermophotovoltaic power generation and optical characterization. Ph.D. dissertation, University of Kentucky, Lexington, Kentucky; 2010.
[19] Francoeur M, Mengüç MP, Vaillon R. Solution of near-field thermal radiation in one-dimensional layered media using dyadic Green's functions and the scattering matrix method. J Quant Spectrosc Radiat Transfer 2009;110:2002–18.
[20] Francoeur M, Mengüç MP, Vaillon R. Spectral tuning of near-field radiative heat flux between two thin silicon carbide films. J Phys D: Appl Phys 2010;43:075501.
[21] Hecht E. Optics. 4th ed.San Francisco: Addison Wesley; 2002.
[22] Mulet J.-P. Modélisation du rayonnement thermique par une approche électromagnétique. Rôle des ondes de surfaces dans le transfert d'énergie aux courtes échelles et dans les forces de Casimir. PhD thesis, Université Paris-Sud 11, Paris; 2003 [in French].
[23] Palik ED. Handbook of optical constants of solids, vol 1. San Diego: Academic Press; 1998.
[24] Narayanaswamy A, Chen G. Surface modes for near field thermophotovoltaics. Appl Phys Lett 2003;82:3544–6.
[25] Chen G. Nanoscale Energy Transport and Conversion. New York.Oxford Press; 2005.
[26] Basu S, Wang LP, Zhang ZM. Direct calculation of energy streamlines in near-field thermal radiation. J Quant Spectrosc Radiat Transfer 2011;112:1149–55.

CHAPTER 3

THE THERMAL DISCRETE DIPOLE APPROXIMATION (T-DDA) FOR NEAR-FIELD RADIATIVE HEAT TRANSFER SIMULATIONS IN THREE-DIMENSIONAL ARBITRARY GEOMETRIES

Reprinted from Journal of Quantitative Spectroscopy and Radiative Transfer, 113, S. Edalatpour and M. Francoeur, The Thermal Discrete Dipole Approximation (T-DDA) for near-field radiative heat transfer simulations in three-dimensional arbitrary geometries, 346-373, Copyright (2014), with permission from Elsevier.

Journal of Quantitative Spectroscopy & Radiative Transfer 133 (2014) 364–373

Contents lists available at ScienceDirect

Journal of Quantitative Spectroscopy & Radiative Transfer

journal homepage: www.elsevier.com/locate/jqsrt

The Thermal Discrete Dipole Approximation (T-DDA) for near-field radiative heat transfer simulations in three-dimensional arbitrary geometries

Sheila Edalatpour*, Mathieu Francoeur*

Radiative Energy Transfer Lab, Department of Mechanical Engineering, University of Utah, Salt Lake City, UT 84112, USA

ARTICLE INFO

Article history:
Received 8 May 2013
Received in revised form
12 July 2013
Accepted 29 August 2013
Available online 4 September 2013

Keywords:
Near-field thermal radiation
Thermal Discrete Dipole Approximation (T-DDA)
Three-dimensional arbitrary geometries
Numerical solution of the stochastic Maxwell equations

ABSTRACT

A novel numerical method called the Thermal Discrete Dipole Approximation (T-DDA) is proposed for modeling near-field radiative heat transfer in three-dimensional arbitrary geometries. The T-DDA is conceptually similar to the Discrete Dipole Approximation, except that the incident field originates from thermal oscillations of dipoles. The T-DDA is described in details in the paper, and the method is tested against exact results of radiative conductance between two spheres separated by a sub-wavelength vacuum gap. For all cases considered, the results calculated from the T-DDA are in good agreement with those from the analytical solution. When considering frequency-independent dielectric functions, it is observed that the number of sub-volumes required for convergence increases as the sphere permittivity increases. Additionally, simulations performed for two silica spheres of 0.5 μm-diameter show that the resonant modes are predicted accurately via the T-DDA. For separation gaps of 0.5 μm and 0.2 μm, the relative differences between the T-DDA and the exact results are 0.35% and 6.4%, respectively, when 552 sub-volumes are used to discretize a sphere. Finally, simulations are performed for two cubes of silica separated by a sub-wavelength gap. The results revealed that faster convergence is obtained when considering cubical objects rather than curved geometries. This work suggests that the T-DDA is a robust numerical approach that can be employed for solving a wide variety of near-field thermal radiation problems in three-dimensional geometries.

1. Introduction

Radiation heat transfer between bodies separated by distances greater than the dominant thermal wavelength is limited by Planck's blackbody distribution. In this far-field regime, radiative heat exchange predictions in three-dimensional (3D) complex geometries are tractable using well-established numerical techniques such as the discrete ordinates method and Monte Carlo approaches [1,2]. In the near-field regime of thermal radiation, which refers to the case where bodies are separated by sub-wavelength gaps, heat transfer can exceed by several orders of magnitude the blackbody limit [1,3–14]. The enhancement beyond Planck's distribution is due to the extraneous contribution to energy transport by waves evanescently confined within a distance of about a wavelength normal to the surface of a thermal source. These modes include evanescent waves generated by total internal reflection of a propagating wave at the material–gap interface as well as resonant surface waves such as surface phonon-polaritons and surface plasmon-polaritons.

To account for tunneling of evanescent modes and wave interference, near-field heat transfer problems are

* Corresponding authors. Tel.: +1 801 581 5721; fax: +1 801 585 9825.
E-mail addresses: sheila.edalatpour@utah.edu (S. Edalatpour), mfrancoeur@mech.utah.edu (M. Francoeur).

0022-4073/$ - see front matter © 2013 Elsevier Ltd. All rights reserved.
http://dx.doi.org/10.1016/j.jqsrt.2013.08.021

modeled using fluctuational electrodynamics [1,3,15]. In this formalism, thermal emission is modeled in Maxwell's equations by stochastic currents that are related to the local temperature of the source via the fluctuation-dissipation theorem. So far, the vast majority of near-field radiative heat transfer predictions have been restricted to simple canonical geometries. This is due to the fact that near-field thermal radiation problems have been mainly solved by deriving analytical expressions for dyadic Green's functions (DGFs); this approach is referred to as the DGF method. The DGF method provides exact results, but becomes intractable when dealing with 3D arbitrarily-shaped objects. Over the past years, the DGF approach has been applied to various cases: two bulks [4–6,15–19], two films [20–23], two structured surfaces [24], two nanoporous materials [25], one-dimensional layered media [26–28], cylindrical cavity [29], two dipoles [30–32], two large spheres [33,34], dipole-surface [35], dipole-structured surface [36], sphere-surface [34,37], two long cylinders [38], two nanorods [39,40], two gratings [41] and N small objects (compared to the wavelength) modeled as electric point dipoles [42].

With the rapid advances in nanofabrication, near-field thermal radiation is becoming an important part of heat transfer engineering. Indeed, near-field thermal radiation may find application in imaging [43], thermophotovoltaic power generation [44–48], nanomanufacturing [49,50], thermal management of electronic devices [51], thermal rectification through a vacuum gap [52,53] and radiative property control [54–56] to name only a few. Due to these numerous potential applications, there is a need for predicting near-field heat exchange in 3D complex geometries. Numerical procedures, namely the finite-difference time-domain (FDTD) method [57–59], the finite-difference frequency-domain (FDFD) method [60] and the boundary element method (BEM) [61] have been applied recently to near-field thermal radiation calculations. Both FDTD and FDFD approaches suffer from large computational time, while the BEM is difficult to apply when dealing with heterogeneous materials. In this work, the Thermal Discrete Dipole Approximation (T-DDA) is proposed for simulating near-field heat transfer between 3D arbitrarily-shaped objects. The Discrete Dipole Approximation (DDA), extensively used for predicting electromagnetic wave scattering by particles, is based on discretizing objects into cubical sub-volumes behaving as electric point dipoles [62–66]. The T-DDA follows the same general procedure as the DDA, except that the incident field is induced by thermal fluctuations of dipoles instead of being produced by an external illumination.

The objective of this paper is to formulate the T-DDA and to test the method against exact results obtained from the DGF approach. In Section 2, the physical and mathematical formulation of the problem is provided. Next, the T-DDA is derived starting from the stochastic Maxwell equations and the associated solution procedure is detailed. In the fourth section, the T-DDA is verified against exact results for two spheres separated by a sub-wavelength vacuum gap; a problem involving two cubes is presented afterwards. Concluding remarks are finally provided.

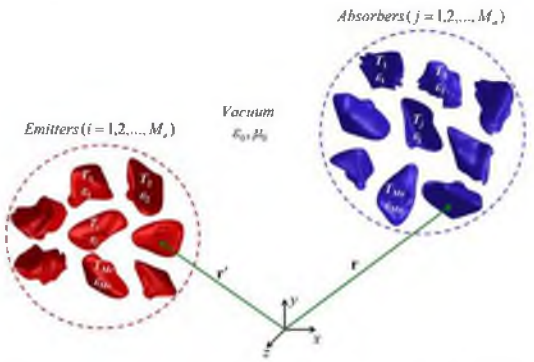

Fig. 1. Schematic representation of the problem under consideration.

2. Physical and mathematical formulation of the problem

The problem under consideration is shown schematically in Fig. 1. A total of $m=1, 2,\ldots, M$ objects at temperatures T_m are submerged in vacuum (medium 0) and are exchanging thermal radiation. The M_e emitters are made up of source points $\mathbf{r}'$ while the M_a absorbers are composed of points $\mathbf{r}$ where the fields are calculated. The bodies are assumed to be in local thermodynamic equilibrium, isotropic, non-magnetic and their electromagnetic responses are described by frequency-dependent dielectric functions $\varepsilon_m = \varepsilon_m' + i\varepsilon_m''$ local in space. No assumptions are made on the shape and size of the objects as well as on their separation distances.

Thermal emission is the result of random fluctuations of charged particles inside a body caused by thermal agitation [3]. On a macroscopic level, this chaotic motion of charged particles is modeled via a stochastic current density $\mathbf{J}^r$ which is added in Maxwell's equations to model thermal emission. The random nature of the thermal current thus makes the Maxwell equations stochastic. Assuming $e^{-i\omega t}$ for the time harmonic fields, the stochastic Maxwell equations in the frequency domain are written as follows [67]:

$$\nabla \times \mathbf{E}(\mathbf{r},\omega) = i\omega\mu_0 \mathbf{H}(\mathbf{r},\omega) \tag{2.1a}$$

$$\nabla \times \mathbf{H}(\mathbf{r},\omega) = -i\omega\varepsilon_0\varepsilon \mathbf{E}(\mathbf{r},\omega) + \mathbf{J}^r(\mathbf{r},\omega) \tag{2.1b}$$

where ε_0 and μ_0 are the vacuum permittivity and permeability, respectively, $\mathbf{E}$ is the electric field and $\mathbf{H}$ denotes the magnetic field.

The first moment of the thermal current is zero (i.e., $\langle \mathbf{J}^r(\mathbf{r},\omega)\rangle = 0$), which implies that the mean radiated fields are also zero [3]. In heat transfer analysis, the quantities of interest are not the mean radiated fields, but the flux and the energy density which are proportional to the ensemble average of the spatial correlation function of currents. This correlation function is provided by the fluctuation-dissipation theorem linking the thermal current to the local temperature of the emitter [3]:

$$\langle \mathbf{J}^r(\mathbf{r}',\omega) \otimes \mathbf{J}^r(\mathbf{r}'',\omega)\rangle = \frac{4\omega\varepsilon_0\varepsilon''}{\pi}\Theta(\omega,T)\delta(\mathbf{r}'-\mathbf{r}'')\bar{\bar{\mathbf{I}}} \tag{2.2}$$

The symbol $\otimes$ represents the outer product defined as $\mathbf{J}^r(\mathbf{r}',\omega)\otimes\mathbf{J}^r(\mathbf{r}'',\omega)=\mathbf{J}^r(\mathbf{r}',\omega)\cdot(\mathbf{J}^r(\mathbf{r}'',\omega))^\dagger$, where the superscript † indicates the Hermitian operator (conjugate transpose). In Eq. (2.2), $\overline{\overline{\mathbf{I}}}$ is the unit dyadic and Θ is the mean energy of an electromagnetic state given by [68]:

$$\Theta(\omega,T)=\frac{\hbar\omega}{\exp(\hbar\omega/k_BT)-1} \tag{2.3}$$

where $\hbar$ is the reduced Planck's constant ($=1.0546\times10^{-34}$ J s) while k_B ($=1.3807\times10^{-22}$ J K^{-1}) is the Boltzmann constant. Note that a factor four is included in the fluctuation-dissipation theorem to account for the fact that only positive frequencies are considered when passing from the time to the frequency domain [68].

In the next section, a general formulation is proposed for modeling near-field radiative heat transfer via the T-DDA.

3. Description of the T-DDA

3.1. Volume integral equation for radiation problems

The starting point of the T-DDA formulation is to decompose the (total) electric field $\mathbf{E}$ as the sum of an incident field, $\mathbf{E}_{inc}$, and a scattered field, $\mathbf{E}_{sca}$:

$$\mathbf{E}(\mathbf{r},\omega)=\mathbf{E}_{inc}(\mathbf{r},\omega)+\mathbf{E}_{sca}(\mathbf{r},\omega) \tag{3.1}$$

The incident field can be interpreted as the field thermally generated by point sources that is propagating in free space in the absence of scatterers. A volume integral equation for the electric field $\mathbf{E}$ can be determined by first taking the curl of both sides of Eq. (2.1a):

$$\nabla\times\mathbf{H}(\mathbf{r},\omega)=-\frac{i}{\omega\mu_0}\nabla\times\nabla\times\mathbf{E}(\mathbf{r},\omega) \tag{3.2}$$

The vector wave equation is determined by substituting Eq. (3.2) into Eq. (2.1b):

$$\nabla\times\nabla\times\mathbf{E}(\mathbf{r},\omega)-k^2\mathbf{E}(\mathbf{r},\omega)=i\omega\mu_0\mathbf{J}^r(\mathbf{r},\omega) \tag{3.3}$$

where k ($=\omega\sqrt{\varepsilon\varepsilon_0\mu_0}$) is the magnitude of the wavevector. A free space form of the vector wave equation is obtained by subtracting $k_0^2\mathbf{E}$ from both sides of Eq. (3.3):

$$\nabla\times\nabla\times\mathbf{E}(\mathbf{r},\omega)-k_0^2\mathbf{E}(\mathbf{r},\omega)=(k^2-k_0^2)\mathbf{E}(\mathbf{r},\omega)+i\omega\mu_0\mathbf{J}^r(\mathbf{r},\omega) \tag{3.4}$$

where k_0 is the magnitude of the wavevector in vacuum. In typical DDA formulations where particles are illuminated by an external source, the incident field satisfies $\nabla\times\nabla\times\mathbf{E}_{inc}-k_0^2\mathbf{E}_{inc}=0$. In radiation heat transfer, the situation is different as the incident field is generated by thermally fluctuating currents. As such, the thermally generated incident field propagating in free space satisfies the following vector wave equation:

$$\nabla\times\nabla\times\mathbf{E}_{inc}(\mathbf{r},\omega)-k_0^2\mathbf{E}_{inc}(\mathbf{r},\omega)=i\omega\mu_0\mathbf{J}^r(\mathbf{r},\omega) \tag{3.5}$$

The vector wave equation for the scattered field can then be obtained by subtracting Eq. (3.5) from Eq. (3.4):

$$\nabla\times\nabla\times\mathbf{E}_{sca}(\mathbf{r},\omega)-k_0^2\mathbf{E}_{sca}(\mathbf{r},\omega)=(k^2-k_0^2)\mathbf{E}(\mathbf{r},\omega) \tag{3.6}$$

The scattered field in Eq. (3.6) can be interpreted as the field generated by an equivalent source function, $(k^2-k_0^2)\mathbf{E}$, propagating in free space. Solutions for Eqs. (3.5) and (3.6) are obtained using the free space DGF denoted by $\overline{\overline{\mathbf{G}}}$ [64]:

$$\mathbf{E}_{inc}(\mathbf{r},\omega)=i\omega\mu_0\int_{V_e}\overline{\overline{\mathbf{G}}}(\mathbf{r},\mathbf{r}',\omega)\cdot\mathbf{J}^r(\mathbf{r}',\omega)dV' \tag{3.7a}$$

$$\mathbf{E}_{sca}(\mathbf{r},\omega)=\int_V(k^2-k_0^2)\overline{\overline{\mathbf{G}}}(\mathbf{r},\mathbf{r}',\omega)\cdot\mathbf{E}(\mathbf{r}',\omega)dV' \tag{3.7b}$$

where V_e is the volume of the emitting bodies, while V ($=V_e+V_a$) is the total volume where V_a is the volume of the absorbing bodies. It can be seen in Eq. (3.7a) that the integration is performed over V_e only where the thermal source is non-zero, while the integration in Eq. (3.7b) is performed over the total volume V to account for the interactions between all objects. The free space DGF is given by [69]:

$$\overline{\overline{\mathbf{G}}}(\mathbf{r},\mathbf{r}',\omega)=\frac{e^{ik_0R}}{4\pi R}\left[\left(1-\frac{1}{(k_0R)^2}+\frac{i}{k_0R}\right)\overline{\overline{\mathbf{I}}}-\left(1-\frac{3}{(k_0R)^2}+\frac{3i}{k_0R}\right)\hat{\mathbf{R}}\otimes\hat{\mathbf{R}}\right] \tag{3.8}$$

where $R=|\mathbf{r}-\mathbf{r}'|$ and $\hat{\mathbf{R}}=(\mathbf{r}-\mathbf{r}')/|\mathbf{r}-\mathbf{r}'|$.

A volume integral equation for the electric field is obtained by substituting the scattered field given by Eq. (3.7b) into Eq. (3.1):

$$\mathbf{E}(\mathbf{r},\omega)-k_0^2\int_V[\varepsilon(\mathbf{r}')-1]\overline{\overline{\mathbf{G}}}(\mathbf{r},\mathbf{r}',\omega)\cdot\mathbf{E}(\mathbf{r}',\omega)dV'=\mathbf{E}_{inc}(\mathbf{r},\omega) \tag{3.9}$$

The DGF has a singularity at $\mathbf{r}=\mathbf{r}'$, such that the principal value method is used to circumvent this problem. In this approach, an infinitesimal volume containing the singularity point is excluded from the integral. For a spherical or cubic exclusion volume, the application of the principal value method leads to [64,70]:

$$k_0^2\int_V[\varepsilon(\mathbf{r}')-1]\overline{\overline{\mathbf{G}}}(\mathbf{r},\mathbf{r}',\omega)\cdot\mathbf{E}(\mathbf{r}',\omega)dV'=k_0^2P.V.\int_V[\varepsilon(\mathbf{r}')-1]\overline{\overline{\mathbf{G}}}(\mathbf{r},\mathbf{r}',\omega)\cdot\mathbf{E}(\mathbf{r}',\omega)dV'-\frac{\varepsilon(\mathbf{r})-1}{3}\mathbf{E}(\mathbf{r},\omega) \tag{3.10}$$

where $P.V.$ stands for principal value. The core equation underlying the T-DDA method is finally obtained by substituting Eq. (3.10) into Eq. (3.9):

$$\frac{\varepsilon(\mathbf{r})+2}{3}\mathbf{E}(\mathbf{r},\omega)-k_0^2P.V.\int_V[\varepsilon(\mathbf{r}')-1]\overline{\overline{\mathbf{G}}}(\mathbf{r},\mathbf{r}',\omega)\cdot\mathbf{E}(\mathbf{r}',\omega)dV'=\mathbf{E}_{inc}(\mathbf{r},\omega) \tag{3.11}$$

where the incident electric field $\mathbf{E}_{inc}$ is specified by Eq. (3.7a). In the next section, Eq. (3.11) is discretized in order to derive a system of linear equations.

3.2. Discretization of the volume integral equation

The first step toward the numerical solution of Eq. (3.11) is the discretization of the emitting and absorbing objects into N cubical sub-volumes on a cubical lattice. The first N_e sub-volumes are located in the emitters, while the N_a ($=N-N_e$) remaining sub-volumes are allocated to the absorbers. The discretization should be fine enough such that the dimension of each sub-volume is small compared to the radiation wavelength (more details about the discretization are provided in Section 4) [63]. If this

condition is satisfied, it can be assumed that the electromagnetic properties and the electric field are uniform inside each sub-volume. Eq. (3.11) evaluated at the center $\mathbf{r}_i$ of a sub-volume i can therefore be written as:

$$\frac{\varepsilon_i+2}{3}\mathbf{E}_i-k_0^2\sum_{j=1}^{N}(\varepsilon_j-1)\left(P.V.\int_{\Delta V_j}\overline{\overline{\mathbf{G}}}(\mathbf{r}_i,\mathbf{r}',\omega)dV'\right)\cdot\mathbf{E}_j=\mathbf{E}_{inc,i},\ i=1,2,\ldots,N \tag{3.12}$$

where the subscripts i and j refer to sub-volumes. In Eq. (3.12), when $i\neq j$, the DGF has no singularity, such that the principal value can be approximated as [64]:

$$P.V.\int_{\Delta V_j}\overline{\overline{\mathbf{G}}}(\mathbf{r}_i,\mathbf{r}',\omega)dV'=\overline{\overline{\mathbf{G}}}_{ij}\Delta V_j,\ i\neq j \tag{3.13}$$

where $\overline{\overline{\mathbf{G}}}_{ij}$ is an abbreviation for $\overline{\overline{\mathbf{G}}}(\mathbf{r}_i,\mathbf{r}_j)$. For $i=j$, the principal value integral is given by [64]:

$$P.V.\int_{\Delta V_j}\overline{\overline{\mathbf{G}}}(\mathbf{r}_i,\mathbf{r}',\omega)dV'=\frac{2}{3k_0^2}\left[e^{ik_0a_i}(1-ik_0a_i)-1\right]\overline{\overline{\mathbf{I}}},\ i=j \tag{3.14}$$

where a_i is the effective radius of sub-volume i defined as $(3\Delta V_i/4\pi)^{1/3}$. The discretized version of the volume integral equation is obtained by substituting Eqs. (3.13) and (3.14) into Eq. (3.12):

$$\left[\frac{\varepsilon_i+2}{3}-\frac{2(\varepsilon_i-1)}{3}(e^{ik_0a_i}(1-ik_0a_i)-1)\right]\mathbf{E}_i-k_0^2\sum_{\substack{j=1\\ j\neq i}}^{N}(\varepsilon_j-1)\Delta V_j\overline{\overline{\mathbf{G}}}_{ij}\cdot\mathbf{E}_j=\mathbf{E}_{inc,i},\ i=1,2,\ldots,N \tag{3.15}$$

Eq. (3.15) is a system of N vector equations where the electric field in each sub-volume is the unknown. It is important to keep in mind that $\mathbf{E}_i$ is stochastic since the incident field is generated by random currents. The incident field, given by Eq. (3.7a), is approximated as follows after discretization into sub-volumes:

$$\mathbf{E}_{inc,i}=\begin{cases}0 & i=1,2,\ldots N_e\\ i\omega\mu_0\sum_{k=1}^{N_e}\overline{\overline{\mathbf{G}}}_{ik}\cdot\mathbf{J}_k^r\Delta V_k & i=N_e+1,\ N_e+2,\ldots,N\end{cases} \tag{3.16}$$

Eq. (3.16) stipulates that the thermally generated incident field is nil in the emitters ($i=1, 2, \ldots, N_e$), while the incident field within the absorbers ($i=N_e+1, N_e+2, \ldots, N$) is due to the $k=1, 2, \ldots, N_e$ emitting dipoles.

From now on, it is assumed that each sub-volume is behaving as an electric point dipole, such that Eq. (3.15) can be re-written in terms of unknown equivalent dipole moments $\mathbf{p}_i$ instead of unknown electric fields $\mathbf{E}_i$ using the relation [64]:

$$\mathbf{E}_i=\frac{3}{\alpha_i^{CM}(\varepsilon_i+2)}\mathbf{p}_i \tag{3.17}$$

where α_i^{CM} is the Clausius–Mossotti polarizability defined as:

$$\alpha_i^{CM}=3\varepsilon_0\frac{\varepsilon_i-1}{\varepsilon_i+2}\Delta V_i \tag{3.18}$$

The random current density $\mathbf{J}_k^r$ in Eq. (3.16) can also be expressed in terms of a thermally fluctuating dipole moment $\mathbf{p}_k^r$ representing thermal emission [69]:

$$\mathbf{J}_k^r=\frac{-i\omega}{\Delta V_k}\mathbf{p}_k^r \tag{3.19}$$

As for the random current, the mean of the thermally fluctuating dipole moment is equal to zero. The random dipole moments are related to the local temperature of the medium via a modified version of the fluctuation-dissipation theorem (see Eq. (2.2)) [71]:

$$\langle\mathbf{p}_k^r\otimes\mathbf{p}_k^r\rangle=\frac{4\varepsilon_0\mathrm{Im}(\alpha_k^{CM})}{\pi\omega}\Theta(\omega,T)\overline{\overline{\mathbf{I}}} \tag{3.20}$$

Using Eqs. (3.17)–(3.19), the system of equations given by Eq. (3.15) can be re-written in terms of unknown dipole moments $\mathbf{p}_i$:

$$\frac{1}{\alpha_i}\mathbf{p}_i-\frac{k_0^2}{\varepsilon_0}\sum_{\substack{j=1\\ j\neq i}}^{N}\overline{\overline{\mathbf{G}}}_{ij}\cdot\mathbf{p}_j=\mathbf{E}_{inc,i},\ i=1,2,\ldots,N \tag{3.21}$$

where

$$\mathbf{E}_{inc,i}=\begin{cases}0 & i=1,2,..,N_e\\ \mu_0\omega^2\sum_{k=1}^{N_e}\overline{\overline{\mathbf{G}}}_{ik}\cdot\mathbf{p}_k^r & i=N_e+1,\ N_e+2,\ldots,N\end{cases} \tag{3.22}$$

The variable α_i in Eq. (3.21) is referred to as the radiative polarizability of dipole i, and is defined as [64]:

$$\alpha_i=\frac{\alpha_i^{CM}}{1-\alpha_i^{CM}/2\pi\varepsilon_0a_i^3[e^{ik_0a_i}(1-ik_0a_i)-1]} \tag{3.23}$$

Eq. (3.21) can be interpreted as follows. The first term on the left-hand side represents the interaction of dipole i with itself (i.e., self-interaction term), while the second term accounts for the interactions of dipole i with all other dipoles except $j=i$. The right-hand side of Eq. (3.21) is the incident field in the absorbing dipoles ($i=N_e+1, N_e+2, \ldots, N$) due to thermal emission by the emitting dipoles ($i=1, 2, \ldots, N_e$). The system of $3N$ scalar equations with $3N$ unknowns (each dipole i has three orthogonal components) can also be written in a compact form using the following matrix notation:

$$\overline{\overline{\mathbf{A}}}\cdot\overline{\mathbf{p}}=\overline{\mathbf{E}}_{inc} \tag{3.24}$$

where $\overline{\mathbf{p}}$ is the $3N$ stochastic column vector containing the unknown dipole moments $\mathbf{p}_i$, $\overline{\mathbf{E}}_{inc}$ is the $3N$ stochastic column vector containing the known incident fields $\mathbf{E}_{inc,i}$, while $\overline{\overline{\mathbf{A}}}$ is the $3N$ by $3N$ deterministic interaction matrix consisting of N^2 3 by 3 sub-matrices. Each sub-matrix $\overline{\overline{\mathbf{A}}}_{ij}$ represents the interactions between dipoles i and j. For clarity, the expanded form of Eq. (3.24) is also given:

$$\begin{bmatrix}\overline{\overline{\mathbf{A}}}_{11} & \overline{\overline{\mathbf{A}}}_{12} & \cdots & \overline{\overline{\mathbf{A}}}_{1N}\\ \overline{\overline{\mathbf{A}}}_{21} & \overline{\overline{\mathbf{A}}}_{22} & \cdots & \overline{\overline{\mathbf{A}}}_{2N}\\ \vdots & \vdots & \ddots & \vdots\\ \overline{\overline{\mathbf{A}}}_{N1} & \overline{\overline{\mathbf{A}}}_{N2} & \cdots & \overline{\overline{\mathbf{A}}}_{NN}\end{bmatrix}\begin{bmatrix}\mathbf{p}_1\\ \mathbf{p}_2\\ \vdots\\ \mathbf{p}_N\end{bmatrix}=\begin{bmatrix}\mathbf{E}_{inc,1}\\ \mathbf{E}_{inc,2}\\ \vdots\\ \mathbf{E}_{inc,N}\end{bmatrix} \tag{3.25}$$

For $i \neq j$, the sub-matrix $\overline{\overline{\mathbf{A}}}_{ij}$ is derived from Eq. (3.21) combined with Eq. (3.8):

$$\overline{\overline{\mathbf{A}}}_{ij} = C_{ij}\begin{bmatrix} \beta_{ij}+\gamma_{ij}\hat{r}_{ij,x}^2 & \gamma_{ij}\hat{r}_{ij,x}\hat{r}_{ij,y} & \gamma_{ij}\hat{r}_{ij,x}\hat{r}_{ij,z} \\ \gamma_{ij}\hat{r}_{ij,y}\hat{r}_{ij,x} & \beta_{ij}+\gamma_{ij}\hat{r}_{ij,y}^2 & \gamma_{ij}\hat{r}_{ij,y}\hat{r}_{ij,z} \\ \gamma_{ij}\hat{r}_{ij,z}\hat{r}_{ij,x} & \gamma_{ij}\hat{r}_{ij,z}\hat{r}_{ij,y} & \beta_{ij}+\gamma_{ij}\hat{r}_{ij,z}^2 \end{bmatrix}, \; i \neq j \tag{3.26}$$

where

$$\hat{r}_{ij,\alpha} = \frac{r_{ij,\alpha}}{r_{ij}}, \; \alpha = x, y, z \tag{3.27a}$$

$$C_{ij} = -\frac{k_0^2}{4\pi\varepsilon_0}\frac{e^{ik_0 r_{ij}}}{r_{ij}} \tag{3.27b}$$

$$\beta_{ij} = \left[1 - \frac{1}{(k_0 r_{ij})^2} + \frac{i}{k_0 r_{ij}}\right] \tag{3.27c}$$

$$\gamma_{ij} = -\left[1 - \frac{3}{(k_0 r_{ij})^2} + \frac{3i}{k_0 r_{ij}}\right] \tag{3.27d}$$

Note that r_{ij} is the magnitude of the distance vector $\mathbf{r}_{ij}$ between dipoles i and j, while $\hat{\mathbf{r}}_{ij}$ is the unit vector along $\mathbf{r}_{ij}$.

For the self-interaction term ($i=j$), the sub-matrix $\overline{\overline{\mathbf{A}}}_{ii}$ is given by:

$$\overline{\overline{\mathbf{A}}}_{ii} = \frac{1}{\alpha_i}\overline{\overline{\mathbf{I}}} \tag{3.28}$$

In the next section, the solution of the stochastic system of equations is discussed.

3.3. Heat transfer calculations

The main objective in heat transfer calculations is to compute the radiative power exchanged between objects. The mean energy dissipated in the absorbers ($i=N_e+1$, N_e+2, ..., N) at a given frequency is calculated as [63,64]:

$$\langle Q_{abs,\omega}\rangle = \frac{\omega}{2}\sum_{i=N_e+1}^{N}\left(\mathrm{Im}[(\alpha_i^{-1})^*] - \frac{2}{3}k_0^2\right)\mathrm{tr}(\langle \mathbf{p}_i \otimes \mathbf{p}_i\rangle) \tag{3.29}$$

According to Eq. (3.29), the unknown dipole moments $\mathbf{p}_i$ do not need to be calculated directly. Instead, the trace of the dipole auto-correlation function, $\mathrm{tr}(\langle \mathbf{p}_i \otimes \mathbf{p}_i\rangle)$, is needed in order to compute the power absorbed. The procedure for calculating the auto-correlations is described hereafter.

If the interaction matrix $\overline{\overline{\mathbf{A}}}$ is invertible, the dipole moment vector $\overline{\mathbf{P}}$ can be determined from Eq. (3.24):

$$\overline{\mathbf{P}} = \overline{\overline{\mathbf{A}}}^{-1} \cdot \overline{\mathbf{E}}_{inc} \tag{3.30}$$

where $\overline{\overline{\mathbf{A}}}^{-1}$ is the inverse of matrix $\overline{\overline{\mathbf{A}}}$. The mean value of $\overline{\mathbf{P}}$ can then be determined from Eq. (3.30):

$$\langle \overline{\mathbf{P}}\rangle = \overline{\overline{\mathbf{A}}}^{-1} \cdot \langle \overline{\mathbf{E}}_{inc}\rangle \tag{3.31}$$

where $\overline{\overline{\mathbf{A}}}^{-1}$ is taken out of the mean operator since it is a deterministic matrix. Using Eq. (3.22), the mean of the incident field at a given dipole i is:

$$\langle \mathbf{E}_{inc,i}\rangle = \begin{cases} 0 & i = 1, 2, .., N_e \\ \mu_0\omega^2 \sum_{k=1}^{N_e} \overline{\overline{\mathbf{G}}}_{ik} \cdot \langle \mathbf{p}_k^r\rangle = 0 & i = N_e+1, \; N_e+2, \ldots, N \end{cases} \tag{3.32}$$

where the linear property of mean operator has been utilized. Eq. (3.32) shows that the mean incident field is zero regardless of i, since the first moment of the thermally fluctuating dipoles is zero. As a result, the mean of the dipole moment vector, $\langle \overline{\mathbf{P}}\rangle$, is equal to zero.

Eq. (3.30) is also used to calculate the correlation matrix of $\overline{\mathbf{P}}$. The correlation matrix of the zero-mean dipole moment vector is defined as [72,73]:

$$\overline{\overline{\mathbf{R}}}_{\mathbf{PP}} = \langle \overline{\mathbf{P}} \otimes \overline{\mathbf{P}}\rangle \tag{3.33}$$

where $\overline{\overline{\mathbf{R}}}_{\mathbf{PP}}$ is a $3N$ by $3N$ matrix consisting of N^2 sub-matrices:

$$\overline{\overline{\mathbf{R}}}_{\mathbf{PP}} = \begin{bmatrix} \overline{\overline{\mathbf{R}}}_{\mathbf{p}_1\mathbf{p}_1} & \overline{\overline{\mathbf{R}}}_{\mathbf{p}_1\mathbf{p}_2} & \cdots & \overline{\overline{\mathbf{R}}}_{\mathbf{p}_1\mathbf{p}_N} \\ \overline{\overline{\mathbf{R}}}_{\mathbf{p}_2\mathbf{p}_1} & \overline{\overline{\mathbf{R}}}_{\mathbf{p}_2\mathbf{p}_2} & \cdots & \overline{\overline{\mathbf{R}}}_{\mathbf{p}_2\mathbf{p}_N} \\ \vdots & \vdots & \ddots & \vdots \\ \overline{\overline{\mathbf{R}}}_{\mathbf{p}_N\mathbf{p}_1} & \overline{\overline{\mathbf{R}}}_{\mathbf{p}_N\mathbf{p}_2} & \cdots & \overline{\overline{\mathbf{R}}}_{\mathbf{p}_N\mathbf{p}_N} \end{bmatrix} \tag{3.34}$$

A given 3 by 3 sub-matrix, $\overline{\overline{\mathbf{R}}}_{\mathbf{p}_i\mathbf{p}_j} = \langle \mathbf{p}_i \otimes \mathbf{p}_j\rangle$, is the correlation matrix of the dipole moments $\mathbf{p}_i$ and $\mathbf{p}_j$. For calculating the power absorbed, only the traces of the correlation matrices $\overline{\overline{\mathbf{R}}}_{\mathbf{p}_i\mathbf{p}_i}$ are needed, such that Eq. (3.29) can be re-written as:

$$\langle Q_{abs,\omega}\rangle = \frac{\omega}{2}\sum_{i=N_e+1}^{N}\left(\mathrm{Im}[(\alpha_i^{-1})^*] - \frac{2}{3}k_0^2\right)\mathrm{tr}\left(\overline{\overline{\mathbf{R}}}_{\mathbf{p}_i\mathbf{p}_i}\right) \tag{3.35}$$

Substitution of Eq. (3.30) into Eq. (3.33), and using the identity $(\overline{\overline{\mathbf{A}}}^{-1} \cdot \mathbf{E}_{inc})^\dagger = \mathbf{E}_{inc}^\dagger \cdot (\overline{\overline{\mathbf{A}}}^{-1})^\dagger$, the correlation matrix of $\overline{\mathbf{P}}$ can be written as:

$$\overline{\overline{\mathbf{R}}}_{\mathbf{PP}} = \overline{\overline{\mathbf{A}}}^{-1} \cdot \overline{\overline{\mathbf{R}}}_{\mathbf{EE}} \cdot \left(\overline{\overline{\mathbf{A}}}^{-1}\right)^\dagger \tag{3.36}$$

where $\overline{\overline{\mathbf{R}}}_{\mathbf{EE}}$ is the $3N$ by $3N$ correlation matrix of the incident field consisting of N^2 sub-matrices. Using the fact that the mean value of the incident field is zero, $\overline{\overline{\mathbf{R}}}_{\mathbf{EE}}$ is calculated as:

$$\overline{\overline{\mathbf{R}}}_{\mathbf{EE}} = \langle \overline{\mathbf{E}}_{inc} \otimes \overline{\mathbf{E}}_{inc}\rangle = \begin{bmatrix} \overline{\overline{\mathbf{R}}}_{\mathbf{E}_1\mathbf{E}_1} & \overline{\overline{\mathbf{R}}}_{\mathbf{E}_1\mathbf{E}_2} & \cdots & \overline{\overline{\mathbf{R}}}_{\mathbf{E}_1\mathbf{E}_N} \\ \overline{\overline{\mathbf{R}}}_{\mathbf{E}_2\mathbf{E}_1} & \overline{\overline{\mathbf{R}}}_{\mathbf{E}_2\mathbf{E}_2} & \cdots & \overline{\overline{\mathbf{R}}}_{\mathbf{E}_2\mathbf{E}_N} \\ \vdots & \vdots & \ddots & \vdots \\ \overline{\overline{\mathbf{R}}}_{\mathbf{E}_N\mathbf{E}_1} & \overline{\overline{\mathbf{R}}}_{\mathbf{E}_N\mathbf{E}_2} & \cdots & \overline{\overline{\mathbf{R}}}_{\mathbf{E}_N\mathbf{E}_N} \end{bmatrix} \tag{3.37}$$

where the 3 by 3 sub-matrix, $\overline{\overline{\mathbf{R}}}_{\mathbf{E}_i\mathbf{E}_j} = \langle \mathbf{E}_{inc,i} \otimes \mathbf{E}_{inc,j}\rangle$, is the correlation matrix of the incident fields in dipoles i and j. A given sub-matrix is calculated by substituting $\mathbf{E}_{inc,i}$ and $\mathbf{E}_{inc,j}$ given by Eq. (3.22):

$$\overline{\overline{\mathbf{R}}}_{\mathbf{E}_i\mathbf{E}_j} = \mu_0^2\omega^4 \sum_{k=1}^{N_e}\sum_{n=1}^{N_e} \overline{\overline{\mathbf{G}}}_{ik} \cdot \langle \mathbf{p}_k^r \otimes \mathbf{p}_n^r\rangle \cdot \overline{\overline{\mathbf{G}}}_{jn}^\dagger, \; i, j \geq N_e+1 \tag{3.38}$$

where $\langle \mathbf{p}_k^r \otimes \mathbf{p}_n^r\rangle$ is non-zero only for $n=k$, and is given by the fluctuation-dissipation theorem (Eq. (3.20)). Substitution of Eq. (3.20) into Eq. (3.38) leads to the following

correlation matrix for the incident field:

$$\overline{\overline{\mathbf{R}}}_{\mathbf{E}_i\mathbf{E}_j}=\frac{4\varepsilon_0\mu_0^2\omega^3\Theta(\omega,T)}{\pi}\sum_{k=1}^{N_e}\mathrm{Im}(\alpha_k^{CM})\overline{\overline{\mathbf{G}}}_{ik}\cdot\overline{\overline{\mathbf{G}}}_{jk}^{\dagger},\ i,j\geq N_e+1 \tag{3.39}$$

The DGFs in Eq. (3.39) have already been calculated when determining the interaction matrix (see Eqs. (3.21) and (3.25)). As such, there is no need to re-compute these DGFs. The DGF $\overline{\overline{\mathbf{G}}}_{lk}$ for $l\neq k$ ($l=i, j$) is related to the interaction sub-matrix $\overline{\overline{\mathbf{A}}}_{lk}$ as follows:

$$\overline{\overline{\mathbf{G}}}_{lk}=-\frac{\varepsilon_0}{k_0^2}\overline{\overline{\mathbf{A}}}_{lk},\ l\neq k \tag{3.40}$$

The incident field correlation sub-matrix is thus expressed in terms of interaction sub-matrices instead of DGFs by substituting Eq. (3.40) into Eq. (3.39):

$$\overline{\overline{\mathbf{R}}}_{\mathbf{E}_i\mathbf{E}_j}=\frac{4\varepsilon_0\Theta(\omega,T)}{\pi\omega}\sum_{k=1}^{N_e}\mathrm{Im}(\alpha_k^{CM})\overline{\overline{\mathbf{A}}}_{ik}\cdot\overline{\overline{\mathbf{A}}}_{jk}^{\dagger},\ i,j\geq N_e+1 \tag{3.41}$$

Eq. (3.41) is employed to populate the correlation matrix given by Eq. (3.37). The correlation matrix $\overline{\overline{\mathbf{R}}}_{\mathbf{EE}}$ is in turn substituted into Eq. (3.36) in order to compute $\overline{\overline{\mathbf{R}}}_{\mathbf{PP}}$. The diagonal elements of $\overline{\overline{\mathbf{R}}}_{\mathbf{PP}}$, corresponding to the auto-correlation of the dipole moments, are finally used for calculating the power absorbed by the M_a objects via Eq. (3.35). From this result, the power absorbed by the M_e objects caused by thermal emission from the M_a bodies can easily be obtained due to the reciprocity of the DGF. As such, the net radiative heat transfer between the emitters and the absorbers can be calculated.

The description of the T-DDA is completed. For clarity, the algorithm for near-field radiation heat transfer predictions via the T-DDA is summarized below.

1. Discretize the emitters and the absorbers into N_e and N_a cubical sub-volumes ΔV_i conceptualized as electric point dipoles with effective radius a_i.
2. Assign a dielectric function ε_i and a temperature T_i to each sub-volume.
3. Calculate the polarizability α_i of each sub-volume using Eqs. (3.18) and (3.23).
4. Calculate the interaction matrix $\overline{\overline{\mathbf{A}}}$ using Eqs. (3.25)–(3.28).
5. Calculate the inverse of the interaction matrix $\overline{\overline{\mathbf{A}}}^{-1}$.
6. Calculate the correlation matrix of the incident field vector $\overline{\overline{\mathbf{R}}}_{\mathbf{EE}}$ using Eqs. (3.37) and (3.41).
7. Calculate the correlation matrix of the dipole moment vector $\overline{\overline{\mathbf{R}}}_{\mathbf{PP}}$ using Eq. (3.36).
8. Calculate the power absorbed $\langle Q_{abs,i}\rangle$ using Eq. (3.35).

4. Results and discussion

4.1. Accuracy of the T-DDA

The accuracy of the T-DDA is subjected to the same validity criteria as the DDA. According to Draine [62], there are three validity criteria associated with the DDA. The first condition stipulates that the number of sub-volumes should be large enough in order to describe the geometries of objects accurately [62]. The error introduced by this effect is known as the shape error. A general quantitative criterion providing the minimum number of sub-volumes to maintain the shape error within an acceptable range has not been established. Yurkin et al. [74] showed that shape error for a specific sub-volume size is bounded by a summation of a_i and a_i^3 terms (a_i is the effective dipole radius associated with a cubical sub-volume), but no information has been provided regarding the coefficients of these error terms. Draine [62] suggested a minimum number of sub-volumes for a sphere in the zero-frequency limit:

$$N_{min}\approx 60|n-1|^3\left(\frac{\Delta}{0.1}\right)^{-3} \tag{4.1}$$

where $n=\sqrt{\varepsilon}$ is the complex refractive index of the material while Δ is the desired fractional accuracy. Eq. (4.1) shows that the minimum number of sub-volumes increases as the refractive index increases for a given Δ value.

According to the second criterion, the discretization should be small enough when compared to the wavelength in the material ($2\pi/n'k_0$) and when compared to the attenuation length of the wave inside the material ($2\pi/n''k_0$) [62]. The latter becomes more important for highly absorptive materials such as metals. A simple criterion for satisfying this condition has been suggested [62,63,75]:

$$N_{min}\approx\frac{4\pi}{3}|n|^3(k_0a_{eff})^3\left(\frac{\Delta}{0.1}\right)^{-3} \tag{4.2}$$

where a_{eff} is the effective radius of the object defined as $a_{eff}=(3V/4\pi)^{1/3}$.

The last condition is concerned with the fact that magnetic dipole effects are neglected when discretizing objects into sub-volumes behaving as electric point dipoles. Indeed, even for non-magnetic materials, magnetic dipole absorption might be comparable, or even greater, than electric dipole absorption when dealing with conductive media such as metals [62,76]. The relative importance of magnetic dipole effects reduces with decreasing the size of the sub-volumes [62]. Therefore, the T-DDA can be applied to conductive media provided that the discretization is fine enough. Draine [62] suggested a criterion that combines Eq. (4.2) with $C_{abs}^m/C_{abs}^e<\Delta$, where C_{abs}^m and C_{abs}^e are the magnetic dipole absorption cross-section and the electric dipole absorption cross-section, respectively. This criterion is given by:

$$N_{min}\approx\frac{4\pi}{3}|n|^3(k_0a_{eff})^3\left(\frac{\Delta}{0.1}\right)^{-3}\left[1+\frac{|n|^3}{36\pi}\left(\frac{\Delta}{0.1}\right)^{3/2}\right] \tag{4.3}$$

By comparing Eq. (4.3) against Eq. (4.2), it is clear that magnetic dipole effects should be considered in the discretization if the following condition is satisfied:

$$|n|\geq(36\pi)^{1/3}\left(\frac{\Delta}{0.1}\right)^{-1/2} \tag{4.4}$$

The T-DDA is evaluated next for different material properties, separation gaps and object shapes.

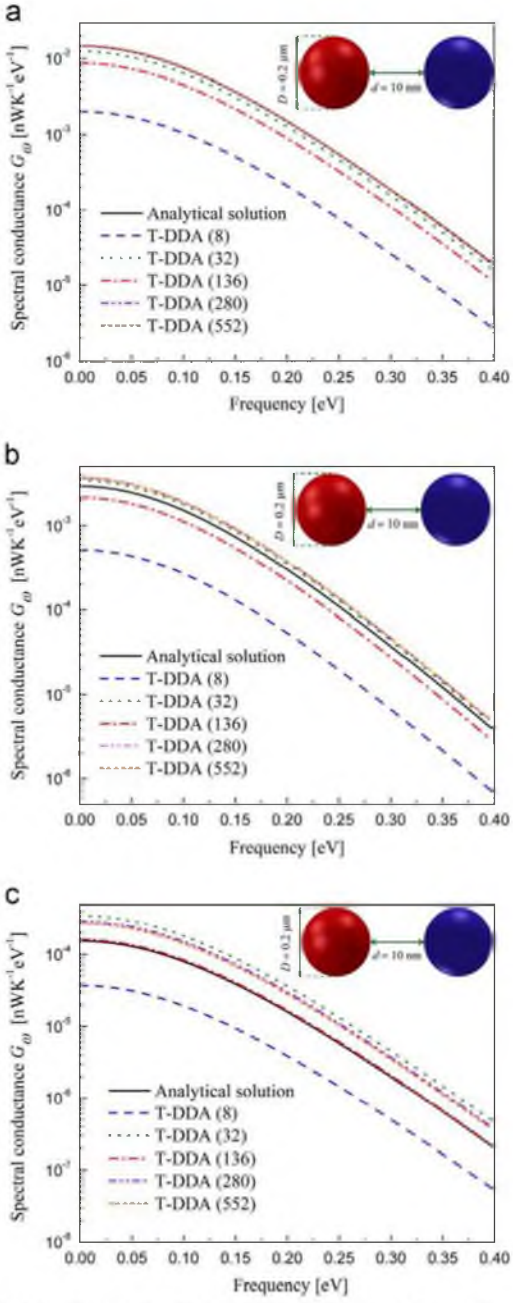

Fig. 2. Verification of the T-DDA against analytical results for two spheres with dielectric functions of: (a) $\varepsilon = 1.2 + 0.1i$, (b) $\varepsilon = 2.5 + 0.1i$, and (c) $\varepsilon = 7.0 + 0.1i$. In all panels, the temperature T is fixed at 400 K.

4.2. Verification of the T-DDA

The T-DDA is first tested by computing the spectral radiative conductance between two spheres and by comparing the results against those obtained from the analytical solution of Narayanaswamy and Chen [33]. The thermal conductance between two objects is defined as follows. Assuming that the first object is at temperature T while the second object is at temperature $T+\delta T$, the spectral conductance G_ω is calculated as:

$$G_\omega = \lim_{\delta T \to 0} \frac{\langle Q_{net,\omega} \rangle}{\delta T} \tag{4.5}$$

where $Q_{net,\omega}$ is the net spectral heat transfer rate between the two objects. The case of two spheres of diameter $D=200$ nm separated by a distance $d=10$ nm is analyzed in Fig. 2; the temperature is fixed at 400 K in all cases considered. The spheres of Fig. 2(a) have a frequency-independent dielectric function of $\varepsilon = 1.2+0.1i$, while the dielectric functions of the spheres in Fig. 2(b) and (c) are assumed to be $\varepsilon = 2.5+0.1i$ and $\varepsilon = 7.0+0.1i$, respectively. The minimum number of sub-volumes, N_{min}, required for satisfying the criteria discussed in Section 4.1 are shown in Table 1 for an accuracy $\Delta = 0.01$. It can be seen in Table 1 that the criterion given by Eq. (4.1) dictates the minimum number of sub-volumes required. Furthermore, the condition given by Eq. (4.3) is ignored since Eq. (4.4) is never satisfied for all cases treated in this paper. The T-DDA simulations have been performed for five different numbers of sub-volumes, from 8 to 552 in each sphere (shown in parentheses in the figures).

Table 1
Minimum number of sub-volumes required for satisfying the criteria given by Eqs. (4.1) and (4.2).

	N_{min} from Eq. (4.1)	N_{min} from Eq. (4.2)
Fig. 2(a)	72	46
Fig. 2(b)	11850	138
Fig. 2(c)	267530	645
Fig. 3(a) and (b)	688160	1193
Fig. 4	N/A	2279

Fig. 2(a) shows that for spheres with dielectric functions close to unity, the T-DDA approaches the analytical solution as the number of sub-volumes increases, and eventually converges to the exact results for 280 sub-volumes. This number is greater than the predicted value given in Table 1. A different behavior is observed in Fig. 2 (b) for a larger dielectric function. As the number of sub-volumes increases, the T-DDA oscillates around the analytical solution. Fig. 2(b) shows that the best results are obtained for 32 sub-volumes. This behavior is in agreement with the observations reported by Yurkin et al. [74], where results showed that the error does not monotonically decreases as the sub-volume size decreases. Instead, the error as a function of the spatial discretization displays a local minimum. For the largest dielectric function, an oscillatory behavior can again be observed in Fig. 2(c). The amplitude of these oscillations is larger than in the previous case of Fig. 2(b). There is a nearly perfect match between the T-DDA and the analytical solution when 136 sub-volumes are used. The comments made for Fig. 2(b) are therefore applicable to the case of Fig. 2(c).

The T-DDA is also applied for calculating the conductance between two spheres made of silica. The diameters of the spheres are fixed at 0.5 μm while the temperature is kept at 400 K. Fig. 3(a) and (b) shows conductance profiles

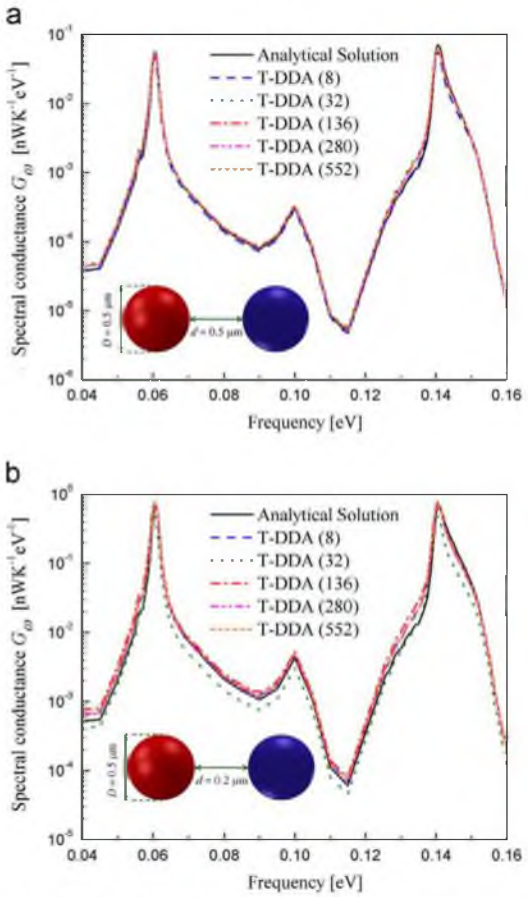

Fig. 3. Spectral conductance between two silica spheres for separation gaps of: (a) 0.5 μm, and (b) 0.2 μm. In both panels, the T-DDA is compared against analytical results and the temperature T is fixed at 400 K.

for separation gaps of 0.5 μm and 0.2 μm, respectively. The frequency-dependent dielectric function of silica has been extracted from the data reported in Ref. [77]. According to the criteria given by Eqs. (4.1) and (4.2), a minimum number of 688,160 and 1193 sub-volumes in each sphere is required to ensure an accuracy of $\Delta=0.01$, respectively, regardless of the separation gap d. However, it can be seen in Fig. 3(a) and (b) that a good agreement between the T-DDA and the analytical solution is achieved for a significantly smaller number of sub-volumes. Additionally, the resonant frequencies are predicted accurately via the T-DDA. For 552 sub-volumes in each sphere, the relative differences between the total conductances calculated from the T-DDA and the analytical solution within the spectral band of from 0.04 eV to 0.16 eV are 0.35% and 6.4% for separation gaps of 0.5 μm and 0.2 μm, respectively. The criteria discussed in Section 4.1 are therefore of little help for the cases treated here. Also, these criteria do not account for the separation distance between the objects, while the results of Fig. 3(a) and (b) suggest that for a fixed number of sub-volumes, the error increases as the separation gap decreases. Further investigation is needed for developing criteria more appropriate to near-field thermal radiation calculations; this is left as a future research effort as it is beyond the scope of this paper.

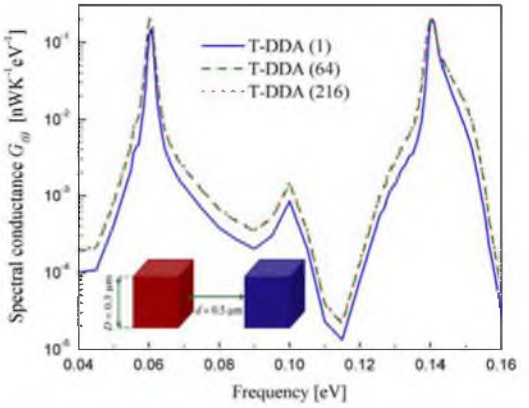

Fig. 4. Spectral conductance between two silica cubes separated by a 0.5 μm-thick gap. The temperature T is fixed at 400 K.

Finally, the spectral conductance between two cubes of silica calculated with the T-DDA is shown in Fig. 4. Both cubes have side lengths of 0.5 μm and are separated by a distance of 0.5 μm; as before, the temperature is fixed at 400 K. Note that an analytical solution does not exist for this problem. Additionally, Eq. (4.1) cannot be applied to cubes for estimating the minimum number of sub-volumes required to ensure an accuracy of $\Delta=0.01$. Nevertheless, a fast convergence of the T-DDA is observed in Fig. 4. Indeed, the relative difference between the total conductances for 64 and 216 sub-volumes in each cube is 1.5%, while the relative difference is 0.6% between 216 and 512 sub-volumes (result not shown). This is in agreement with Yurkin et al. [74], where it was shown that the error associated with cubically shaped objects is smaller than for curved geometries.

5. Conclusions

A new method called the Thermal Discrete Dipole Approximation (T-DDA) was proposed for modeling near-field thermal radiation in three-dimensional arbitrary geometries. The T-DDA is conceptually similar to the Discrete Dipole Approximation, except that the incident field originates from thermal oscillations of dipoles rather than by an external radiation source. The T-DDA was verified against exact results for two spheres separated by a sub-wavelength gap for various dielectric functions and separation distances. In all cases considered, the results obtained from the T-DDA were in good agreement with the exact results. Moreover, the resonant frequencies arising between two silica spheres were predicted accurately. For this last case, the relative errors between the analytical and the T-DDA results of total conductance were 0.35% and 6.4% for two 0.5 μm-diameter spheres separated by gaps of 0.5 μm and 0.2 μm, respectively. The T-DDA results exhibited an oscillatory behavior when the dielectric function of the materials is far from unity. It was also

observed that for a fixed number of sub-volumes, the error increases as the separation gap decreases. Additionally, faster convergence was achieved when considering two cubes rather than two spheres.

This paper suggests that the T-DDA is a robust, relatively simple simulation tool for predicting near-field radiative heat exchange. The convergence and the accuracy of the T-DDA need further investigation, and this is left as a future research effort.

Acknowledgment

This work was partially supported by the US Army Research Office under Grant no. W911NF-12-1-0422 Mod. 1.

References

[1] Howell JR, Siegel R, Mengüç MP. Thermal radiation heat transfer. 5th ed. Boca Raton, FL: CRC Press; 2010.
[2] Modest MF. Radiative heat transfer. 3rd ed.. Oxford, UK: Elsevier; 2013.
[3] Rytov SM, Kravtsov YA, Tatarskii VI. Principles of statistical radiophysics 3: Elements of random fields. New York: Springer; 1989.
[4] Polder D, Van Hove M. Theory of radiative heat transfer between closely spaced bodies. Phys Rev B 1971;4(10):3303–14.
[5] Loomis JJ, Maris HJ. Theory of heat transfer by evanescent electromagnetic waves. Phys Rev B 1994;50(24):18517–24.
[6] Joulain K, Mulet J-P, Marquier F, Carminati R, Greffet J-J. Surface electromagnetic waves thermally excited: radiative heat transfer, coherence properties and Casimir forces revisited in the near field. Surf Sci Rep 2005;57:59–112.
[7] Biehs S-A, Rousseau E, Greffet J-J. Mesoscopic description of radiative heat transfer at the nanoscale. Phys Rev Lett 2010;105:234301.
[8] Kittel A, Müller-Hirsch W, Parisi J, Biehs S-A, Reddig D, Holthaus M. Near-field radiative heat transfer in a scanning thermal microscope. Phys Rev Lett 2005;95:224301.
[9] Shen S, Narayanaswamy A, Chen G. Surface phonon polaritons mediated energy transfer between nanoscale gaps. Nano Lett 2009;9(8):2909–13.
[10] Shen S, Mavrokefalos A, Sambegoro P, Chen G. Nanoscale thermal radiation between two gold surfaces. Appl Phys Lett 2012;100:233114.
[11] Hu L, Narayanaswamy A, Chen XY, Chen G. Near-field thermal radiation between two closely spaced glass plates exceeding Planck's blackbody radiation law. Appl Phys Lett 2008;92:133106.
[12] Rousseau E, Siria A, Jourdan G, Volz S, Comin F, Chevrier J, et al. Radiative heat transfer at the nanoscale. Nat Photonics 2009;3(9):514–7.
[13] Ottens RS, Quetschke V, Wise S, Alemi AA, Lundock R, Mueller G, et al. Near-field radiative heat transfer between macroscopic planar surfaces. Phys Rev Lett 2011;107:014301.
[14] Biehs S-A, Tschikin M, Ben-Abdallah P. Hyperbolic metamaterials as an analog of a blackbody in the near field. Phys Rev Lett 2012;109:104301.
[15] Francoeur M, Mengüç MP. Role of fluctuational electrodynamics in near-field radiative heat transfer. J Quant Spectrosc Radiat Transfer 2008;109:280–93.
[16] Mulet J-P, Joulain K, Carminati R, Greffet J-J. Enhanced radiative heat transfer at nanometric distances. Nanoscale Microscale Thermophys Eng 2002;6:209–22.
[17] Fu CJ, Zhang ZM. Nanoscale radiation heat transfer for silicon at different doping levels. Int J Heat Mass Transfer 2006;49:1703–18.
[18] Chapuis P-O, Volz S, Henkel C, Joulain K, Greffet J-J. Effects of spatial dispersion in near-field radiative heat transfer between two parallel metallic surfaces. Phys Rev B 2008;77:035431.
[19] Volokitin AI, Persson BNJ. Radiative heat transfer between nanostructures. Phys Rev B 2001;63:205404.
[20] Francoeur M, Mengüç MP, Vaillon R. Spectral tuning of near-field radiative heat flux between two thin silicon carbide films. J Phys D Appl Phys 2010;43:075501.
[21] Francoeur M, Mengüç MP, Vaillon R. Local density of electromagnetic states within a nanometric gap formed between two thin films supporting surface phonon polaritons. J Appl Phys 2010;107:034313.
[22] Francoeur M, Mengüç MP, Vaillon R. Coexistence of multiple regimes for near-field thermal radiation between two layers supporting surface phonon polaritons in the infrared. Phys Rev B 2011;84:075436.
[23] Ben-Abdallah P, Joulain K, Drevillon J, Domingues G. Near-field heat transfer mediated by surface wave hybridization between two films. J Appl Phys 2009;106:044306.
[24] Biehs S-A, Huth O, Ruting F. Near-field radiative heat transfer for structured surfaces. Phys Rev B 2008;78:085414.
[25] Biehs S-A, Ben-Abdallah P, Rosa FSS, Joulain K, Greffet J-J. Nanoscale heat flux between nanoporous materials. Opt Express 2011;19:A1088–103.
[26] Narayanaswamy A, Chen G. Direct computation of thermal emission from nanostructures. Ann Rev Heat Transfer 2005;14:169–95.
[27] Francoeur M, Mengüç MP, Vaillon R. Solution of near-field thermal radiation in one-dimensional layered media using dyadic Green's functions and the scattering matrix method. J Quant Spectrosc Radiat Transfer 2009;110:2002–18.
[28] Zheng Z, Xuan Y. Theory of near-field radiative heat transfer for stratified magnetic media. Int J Heat Mass Transfer 2011;54:1101–10.
[29] Hammonds Jr. JS. Thermal transport via surface phonon polaritons across a two-dimensional pore. Appl Phys Lett 2006;88:041912.
[30] Domingues G, Volz S, Joulain K, Greffet J-J. Heat transfer between two nanoparticles through near field interaction. Phys Rev Lett 2005;94:085901.
[31] Chapuis P-O, Laroche M, Volz S, Greffet J-J. Radiative heat transfer between metallic nanoparticles. Appl Phys Lett 2008;92:201906.
[32] Chapuis P-O, Laroche M, Volz S, Greffet J-J. Erratum: radiative heat transfer between metallic nanoparticles. Appl Phys Lett 2010;97:269903.
[33] Narayanaswamy A, Chen G. Thermal near-field radiative transfer between two spheres. Phys Rev B 2008;77:075125.
[34] Krüger M, Bimonte G, Emig T, Kardar M. Trace formulas for nonequilibrium Casimir interactions, heat radiation, and heat transfer for arbitrary objects. Phys Rev B 2012;86:115423.
[35] Mulet J-P, Joulain K, Carminati R, Greffet J-J. Nanoscale radiative heat transfer between a small particles and a plane surface. Appl Phys Lett 2001;78(19):2931–3.
[36] Biehs S-A, Greffet J-J. Near-field heat transfer between a nanoparticle and a rough surface. Phys Rev B 2010;81:245414.
[37] Otey C, Fan S. Numerically exact calculations of electromagnetic heat transfer between a dielectric sphere and a plate. Phys Rev B 2011;84:245431.
[38] Golyk VA, Krüger M, Kardar M. Heat radiation from long cylindrical objects. Phys Rev E 2012;85:046603.
[39] Carrillo C, Bayazitoglu Y. Sphere approximation for nanorod near-field radiative heat exchange analysis. Nanoscale Microscale Thermophys Eng 2011;15:195–208.
[40] Carrillo LY, Bayazitoglu. Nanorod near-field radiative heat exchange analysis. J Quant Spectrosc Radiat Transfer 2011;112:412–9.
[41] Biehs S-A, Rosa FSS, Ben-Abdallah P. Modulation of near-field heat transfer between two gratings. Appl Phys Lett 2011;98:243102.
[42] Ben-Abdallah P, Biehs S-A, Joulain K. Many-body radiative heat transfer theory. Phys Rev Lett 2011;107:114301.
[43] De Wilde Y, Formanek F, Carminati R, Gralak B, Lemoine P-A, Joulain K, et al. Thermal radiation scanning tunneling microscopy. Nature 2006;444:740–3.
[44] DiMatteo RS, Greiff P, Finberg SL, Young-Waithe KA, Choy HKH, Masaki MM, et al. Enhanced photogeneration of carriers in a semiconductor via coupling across a nonisothermmal nanoscale vacuum gap. Appl Phys Lett 2001;79(12):1894–6.
[45] Whale MD, Cravalho EG. Modeling and performance of microscale thermophotovoltaic energy conversion devices. IEEE Trans Energy Convers 2002;17(1):130–42.
[46] Laroche M, Carminati R, Greffet J-J. Near-field thermophotovoltaic energy conversion. J Appl Phys 2006;100:063704.
[47] Park K, Basu S, King WP, Zhang ZM. Performance analysis of near-field thermophotovoltaic devices considering absorption distribution. J Quant Spectrosc Radiat Transfer 2008;109:305–16.
[48] Francoeur M, Vaillon R, Mengüç MP. Thermal impacts on the performance of nanoscale-gap thermophotovoltaic power generators. IEEE Trans Energy Convers 2011;26:686–98.
[49] Hawes EA, Hastings JT, Crofcheck C, Mengüç MP. Spatially selective melting and evaporation of nanosized gold particles. Opt Lett 2008;33:1383–5.
[50] Loke VLY, Mengüç MP. Surface waves and atomic force microscope probe-particle near-field coupling: discrete dipole approximation with surface interaction. J Opt Soc Am A 2010;27(10):2293–303.

[51] Guha B, Otey C, Poitras CB, Fan S, Lipson M. Near-field radiative cooling of nanostructures. Nano Lett 2012;12:4546–50.
[52] Otey CR, Lau WT, Fan S. Thermal rectification through vacuum. Phys Rev Lett 2010;104:154301.
[53] Basu S, Francoeur M. Near-field radiative transfer based thermal rectification using doped silicon. Appl Phys Lett 2011;98:113106.
[54] Greffet J-J, Carminati R, Joulain K, Mulet J-P, Mainguy S, Chen Y. Coherent emission of light by thermal sources. Nature 2002;416:61–4.
[55] Lee BJ, Wang LP, Zhang ZM. Coherent thermal emission by excitation of magnetic polaritons between periodic strips and a metallic film. Opt Express 2008;16:11328–36.
[56] Francoeur M, Basu S, Petersen SJ. Electric and magnetic surface polariton mediated near-field radiative heat transfer between metamaterials made of silicon carbide particles. Opt Express 2011;19:18774–88.
[57] Rodriguez AJ, Ilic O, Bermel P, Celanovic I, Joannopoulos JD, Soljacic M, et al. Frequency-selective near-field radiative heat transfer between photonic crystal slabs: A computational approach for arbitrary geometries and materials. Phys Rev Lett 2011;107:114302.
[58] Liu B, Shen S. Broadband near-field radiative thermal emitter/absorber based on hyperbolic metamaterials: direct numerical simulation by the Wiener chaos expansion method. Phys Rev B 2013;87:115403.
[59] Datas A, Hirashima D, Hanamura K. FDTD simulation of near-field radiative heat transfer between thin films supporting surface phonon polaritons: Lessons learned. J Therm Sci Technol 2013;8:91–105.
[60] Wen S-B. Direct numerical simulation of near field thermal radiation based on Wiener chaos expansion of thermal fluctuating current. ASME J Heat Transfer 2010;132:072704.
[61] Rodriguez AW, Reid MTH, Johnson SG. Fluctuating surface-current formulation of radiative heat transfer for arbitrary geometries. Phys Rev B 2012;86:220302(R).
[62] Draine BT. The discrete-dipole approximation and its application to interstellar graphite grains. Astrophys J 1988;333:848–72.
[63] Draine BT, Flatau PJ. Discrete-dipole approximation for scattering calculations. J the Opt Soc Am A 1994;11:1491–9.
[64] Schmehl R. The coupled-dipole method for light scattering from particles on plane surfaces. Arizona State University; 1994 ([MS thesis]).
[65] Yurkin MA, Hoekstra AG. The discrete dipole approximation: an overview and recent developments. J Quant Spectrosc Radiat Transfer 2007;106:558–89.
[66] Loke VLY, Mengüç MP, Nieminen TA. Discrete-dipole approximation with surface interaction: computational toolbox for MATLAB. J Quant Spectrosc Radiat Transfer 2011;112:1711–25.
[67] Balanis CA. Advanced engineering electromagnetics. 2nd ed. Hoboken, NJ: John Wiley & Sons; 2012.
[68] Zhang ZM. Micro/nanoscale heat transfer.New York: McGraw-Hill; 2007.
[69] Novotny L, Hecht B. Principles of nano-optics.New York: Cambridge University Press; 2006.
[70] Chew WC. Waves and fields in inhomogeneous media. Piscataway, NJ: IEEE Press; 1995.
[71] Mulet J.-P., Modèlisation du rayonnement thermique par une approche électromagnétique. Rôle des ondes de surfaces dans le transfert d'énergie aux courtes échelles et dans les forces de Casimir, Université Paris-Sud 11, Paris. .[Ph.D. thesis, in French], 2003.
[72] Yates RD, Goodman DJ. Probability and stochastic processes. 2nd ed. Wiley; 2005.
[73] Schreir PJ. Correlation coefficients for complex random vectors. Signals Syst Comput 2007:577–81.
[74] Yurkin MA, Maltsev VP, Hoekstra AG. Convergence of the discrete dipole approximation. I. Theoretical analysis. J Opt Soc Am A 2006:23:2578–91.
[75] Zubko E, Petrov D, Grynko Y, Shkuratov Y, Okamoto H, Muinonen K, et al. Validity criteria of the discrete dipole approximation. Appl Opt 2010;49:1267–79.
[76] Draine BT, Lee HM. Optical properties of interstellar graphite and silicate grains. Astrophys J 1984;285:89–108.
[77] Sasihithlu K, Narayanaswamy A. Convergence of vector spherical wave expansion method applied to near-field radiative transfer. Opt Express 2011;19:772–85.

CHAPTER 4

CONVERGENCE ANALYSIS OF THE THERMAL DISCRETE DIPOLE APPROXIMATION

PHYSICAL REVIEW E 91, 063307 (2015)

Convergence analysis of the thermal discrete dipole approximation

Sheila Edalatpour,[1,*] Martin Čuma,[2] Tyler Trucax,[1] Roger Backman,[1] and Mathieu Francoeur[1,†]
[1]*Radiative Energy Transfer Lab, Department of Mechanical Engineering, University of Utah, Salt Lake City, Utah 84112, USA*
[2]*Center for High Performance Computing, University of Utah, Salt Lake City, Utah 84112, USA*
(Received 7 February 2015; published 15 June 2015)

The thermal discrete dipole approximation (T-DDA) is a numerical approach for modeling near-field radiative heat transfer in complex three-dimensional geometries. In this work, the convergence of the T-DDA is investigated by comparison against the exact results for two spheres separated by a vacuum gap. The error associated with the T-DDA is reported for various sphere sizes, refractive indices, and vacuum gap thicknesses. The results reveal that for a fixed number of subvolumes, the accuracy of the T-DDA degrades as the refractive index and the sphere diameter to gap ratio increase. A converging trend is observed as the number of subvolumes increases. The large computational requirements associated with increasing the number of subvolumes, and the shape error induced by large sphere diameter to gap ratios, are mitigated by using a nonuniform discretization scheme. Nonuniform discretization is shown to significantly accelerate the convergence of the T-DDA, and is thus recommended for near-field thermal radiation simulations. Errors less than 5% are obtained in 74% of the cases studied by using up to 82 712 subvolumes. Additionally, the convergence analysis demonstrates that the T-DDA is very accurate when dealing with surface polariton resonant modes dominating radiative heat transfer in the near field.

DOI: 10.1103/PhysRevE.91.063307 PACS number(s): 02.70.−c, 44.40.+a, 42.25.Bs

I. INTRODUCTION

Near-field thermal radiation has recently attracted significant interest due to potential applications in thermal management of nanoscale devices [1], imaging [2], nanomanufacturing [3,4], thermal rectification [5,6], near-field thermal spectroscopy [7–9], and thermophotovoltaic power generation [10–12]. In the near-field regime, arising when the distance between bodies is smaller than Wien's wavelength, radiative heat transfer exceeds the far-field blackbody limit due to tunneling of evanescent modes [13–15]. As such, the classical theory based on Planck's blackbody distribution cannot be applied to near-field thermal radiation predictions. Instead, near-field radiative heat transfer problems are modeled using fluctuational electrodynamics where stochastic current densities representing thermal radiation sources are added to the Maxwell equations [16]. A significant amount of research has been devoted to the analysis of near-field radiative heat transfer in one-dimensional layered geometry for which an exact solution can be derived using dyadic Green's functions (DGFs) [17–21]. Exact solutions have also been derived for configurations such as near-field radiative heat transfer between nanoparticles [22], between two spheres [23–25], and between a sphere and a surface [26,27]. When dealing with three-dimensional complex geometries, it is necessary to employ numerical techniques. So far, a few numerical methods have been proposed for solving the thermal stochastic Maxwell equations [28–34]. Edalatpour and Francoeur [35] presented a relatively simple approach called the thermal discrete dipole approximation (T-DDA). The T-DDA is based on the discrete dipole approximation (DDA), which is a well-known method for modeling light absorption and scattering by particles with size comparable to, or smaller than, the wavelength [36–38]. In both the T-DDA and the DDA, objects are discretized into cubical subvolumes conceptualized as electric point dipoles. The main distinctive feature of the T-DDA is that the dipole moments in the subvolumes are induced not only by an external illumination but also by thermally fluctuating dipoles arising from thermal agitation of charges.

The accuracy and convergence of the DDA have been studied extensively in the literature, and a detailed, comprehensive discussion of this topic can be found in Ref. [38]. The accuracy of the DDA is a function of three main parameters, namely the shape, the size, and the refractive index of the objects [38,39]. The convergence of the DDA has been empirically analyzed using analytical solutions for a single, isolated sphere (Mie theory) [37,39–41] and for two spheres in contact [37,42,43]. In general, the accuracy of the DDA degrades as the refractive index and/or the size increase [37,39,40,44], while it improves as the number of subvolumes increases [37,39,44–46]. The computational requirements associated with the DDA grow as the number of subvolumes increases, such that the maximum size and refractive index that can be modeled are limited by the available computational resources. Traditionally, the DDA is said to be suitable for objects with refractive index m satisfying the relation $|m-1| \leqslant 2$ [47,48]. Larger refractive indices can also be handled with the DDA by utilizing techniques such as the weighted discretization approach [49,50] and the filtered coupled-dipole method [50–52]. Draine and Flatau [47] recommend using the DDA for objects of normalized size $k_0 D_{\text{eff}}$ less than 50, where k_0 is the magnitude of the wave vector in free space and D_{eff} is the effective diameter of the object. However, this is an approximate criterion since the DDA has been applied to objects as large as $k_0 D_{\text{eff}} = 640$ for near unity refractive indices [48]. Additionally, the convergence of the DDA is much faster for cubically shaped objects that can be represented exactly by cubical subvolumes than for spheres due to the absence of shape error [44,45,53]. Based on an empirical analysis, Draine [39] proposed three criteria for determining the minimum number of subvolumes required to achieve a desired fractional error. These criteria are concerned with the shape error, the variation of the electric field

*Corresponding author: sheila.edalatpour@utah.edu
†Corresponding author: mfrancoeur@mech.utah.edu

inside the objects, and the minimum subvolume size to ensure that the contribution of the magnetic dipoles to the absorption is negligible when compared to the contribution from the electric dipoles. Zubko *et al.* [54] pointed out that the second criterion ensuring negligible variation of the electric field overestimates the number of subvolumes required for modeling irregular objects with surface roughness. Yurkin *et al.* [44,45] analyzed theoretically the convergence of the DDA. It was shown that the error associated with any quantity of interest (e.g., absorption and scattering cross sections) is delimited by a summation of a linear and a quadratic term in the discretization parameter. An extrapolation technique providing an estimation of the error as a function of the discretization parameter was proposed. The superposition of the estimated error and the DDA solution for a cube improved the accuracy of the results by two orders of magnitude. Using this approach, improvement of the accuracy of the DDA was also observed for other shapes.

For thermal radiation problems treated by the T-DDA, the separation gap between the objects is a supplementary parameter that must be accounted for. Indeed, the gap to wavelength ratio and the object size to gap ratio determine the relative contributions of propagating and evanescent modes to radiative heat transfer, and thus the variation of the electric field within the objects. The shape error associated with the T-DDA is also a strong function of the object size to gap ratio. Additionally, Edalatpour and Francoeur [35] showed that Draine's criteria [39] discussed in the previous paragraph largely overestimate the number of subvolumes required to achieve a desired accuracy when applied to the T-DDA. There is therefore a strong motivation for analyzing the accuracy and the convergence of the T-DDA, as near-field thermal radiation simulations differ significantly from traditional scattering and absorption calculations performed with the DDA.

In this work, the convergence of the T-DDA is studied by computing the relative error between the thermal conductance obtained using the exact solution for two spheres separated by a vacuum gap [23–25] and the thermal conductance from T-DDA simulations for the same configuration. The analysis is performed for three types of sizes, namely $k_0 D \ll 1$, $k_0 D \approx 1$, and $k_0 D \gg 1$ (D is the diameter of the sphere). For each size, the distance between the spheres is varied such that the performances of the T-DDA are evaluated in all near-field radiative transfer regimes. As in the DDA, the refractive index of the spheres is expected to have a significant impact on the T-DDA performances. Therefore, various refractive indices, including large and small real and imaginary parts, and a refractive index corresponding to a resonant mode, are examined. A nonuniform discretization scheme is also proposed for accelerating the convergence of the T-DDA.

This paper is organized as follows. The T-DDA described in Ref. [35] has been slightly modified, such that the main steps and equations of the updated formulation are provided in Sec. II. The approximations made in the T-DDA are listed in Sec. III. The convergence analysis is afterwards presented and is followed by concluding remarks in Sec. V. Finally, the Appendix demonstrates that the T-DDA reduces to the previously published dipole approximation [55] in the limit that the sphere diameter is much smaller than the gap size and the wavelength.

II. DESCRIPTION OF THE T-DDA FORMALISM

The T-DDA framework is established by considering L bodies, with frequency-dependent dielectric functions local in space $\varepsilon_l = \varepsilon_l' + i\varepsilon_l''$ and temperatures T_l, submerged in the free space. All bodies are assumed to be in local thermodynamic equilibrium, isotropic, and nonmagnetic. L_e bodies emit thermal radiation ($T_l > 0$ K, $l = 1,2,\ldots,L_e$) while the remaining L_a bodies are pure absorbers ($T_l = 0$ K, $l = L_e + 1, L_e + 2, \ldots, L$). The objective is to calculate the radiative energy transferred to the absorbers. Thermal emission is due to random fluctuations of charges inside the bodies and is modeled using fluctuational electrodynamics [16]. For nonmagnetic materials, as considered here, a fluctuating electric current $\mathbf{J}^{fl}$ is added to Ampère's law in the Maxwell equations. The ensemble average of the fluctuating current (first moment) is zero while the ensemble average of its spatial correlation function (second moment) is given by the fluctuation-dissipation theorem [16]:

$$\langle \mathbf{J}^{fl}(\mathbf{r}',\omega) \otimes \mathbf{J}^{fl}(\mathbf{r}'',\omega') \rangle = \frac{4\omega\varepsilon_0\varepsilon''}{\pi}\Theta(\omega,T)\delta(\mathbf{r}' - \mathbf{r}'')\delta(\omega - \omega')\bar{\bar{\mathbf{I}}}, \tag{1}$$

where $\otimes$ denotes the outer product defined as the multiplication of the first vector by the conjugate transpose of the second vector, $\bar{\bar{\mathbf{I}}}$ is the unit dyadic and $\Theta(\omega,T)$ is the mean energy of an electromagnetic state given by $\hbar\omega/[\exp(\hbar\omega/k_B T) - 1]$. Due to the random nature of the fluctuating current, near-field thermal radiation problems are stochastic and are mathematically described by the thermal stochastic Maxwell equations.

The total electric field at location $\mathbf{r}$ and frequency ω is the sum of contributions from fluctuating, scattered, and incident fields. The fluctuating field is generated by thermal excitation of charges in bodies with temperature larger than absolute zero, while the scattered field is due to multiple electromagnetic interactions between the bodies. The incident field is produced by an external source such as thermal emission by the surroundings (sometimes referred to as the bosonic field or the thermal bath) and/or illumination by a laser. The following free-space vector wave equation for the total electric field $\mathbf{E}$ is derived from the thermal stochastic Maxwell equations:

$$\nabla \times \nabla \times \mathbf{E}(\mathbf{r},\omega) - k_0^2 \mathbf{E}(\mathbf{r},\omega) = i\omega\mu_0 \mathbf{J}(\mathbf{r},\omega). \tag{2}$$

The current $\mathbf{J}$ is an equivalent source function producing scattered and fluctuating fields:

$$\mathbf{J}(\mathbf{r},\omega) = -i\omega\varepsilon_0(\varepsilon - 1)\mathbf{E}(\mathbf{r},\omega) + \mathbf{J}^{fl}(\mathbf{r},\omega), \tag{3}$$

where the first term on the right-hand side of Eq. (3) is the source function for the scattered field [35]. The incident field is generated by an external source and satisfies the homogenous vector wave equation in free space $\nabla \times \nabla \times \mathbf{E}^{inc}(\mathbf{r},\omega) - k_0^2 \mathbf{E}^{inc}(\mathbf{r},\omega) = \mathbf{0}$. The total electric field at location $\mathbf{r}$ and

frequency ω can thus be written as follows:

$$\mathbf{E}(\mathbf{r},\omega) = i\omega\mu_0 \int_V \overline{\overline{\mathbf{G}}}(\mathbf{r},\mathbf{r}',\omega)\cdot\mathbf{J}(\mathbf{r}',\omega)dV' + \mathbf{E}^{inc}(\mathbf{r},\omega), \quad (4)$$

where V is the total volume of the emitting and absorbing bodies and $\overline{\overline{\mathbf{G}}}$ is the free-space DGF defined as [56]:

$$\overline{\overline{\mathbf{G}}}(\mathbf{r},\mathbf{r}',\omega) = \frac{e^{ik_0R}}{4\pi R}\left[\left(1-\frac{1}{(k_0R)^2}+\frac{i}{k_0R}\right)\overline{\overline{\mathbf{I}}} - \left(1-\frac{3}{(k_0R)^2}+\frac{3i}{k_0R}\right)\hat{\mathbf{R}}\otimes\hat{\mathbf{R}}\right]. \quad (5)$$

The first term on the right-hand side of Eq. (4) is the sum of the fluctuating field ($i\omega\mu_0\int_V \overline{\overline{\mathbf{G}}}(\mathbf{r},\mathbf{r}',\omega)\cdot\mathbf{J}^{fl}(\mathbf{r}',\omega)dV'$), due to thermal fluctuations everywhere in V where $T > 0$ K, and the scattered field ($k_0^2\int_V \overline{\overline{\mathbf{G}}}(\mathbf{r},\mathbf{r}',\omega)\cdot(\varepsilon-1)\mathbf{E}(\mathbf{r}',\omega)dV'$). In Eq. (5), $R = |\mathbf{r}-\mathbf{r}'|$ and $\hat{\mathbf{R}} = (\mathbf{r}-\mathbf{r}')/|\mathbf{r}-\mathbf{r}'|$.

Equation (4) is discretized by dividing the L objects into N cubical subvolumes on a cubical lattice. The electric field at the center point $\mathbf{r}_i$ of subvolume i ($i = 1, 2, \ldots, N$) can be written as:

$$\mathbf{E}(\mathbf{r}_i,\omega) = i\omega\mu_0\sum_{j\neq i}\int_{\Delta V_j}\overline{\overline{\mathbf{G}}}(\mathbf{r}_i,\mathbf{r}',\omega)\cdot\mathbf{J}(\mathbf{r}',\omega)dV' + i\omega\mu_0\int_{\Delta V_i}\overline{\overline{\mathbf{G}}}(\mathbf{r}_i,\mathbf{r}',\omega)\cdot\mathbf{J}(\mathbf{r}',\omega)dV' + \mathbf{E}^{inc}(\mathbf{r}_i,\omega). \quad (6)$$

The integration over ΔV_i in Eq. (6) is treated separately since the DGF has a singularity at $\mathbf{r}' = \mathbf{r}_i$. Next, it is assumed that the free-space DGF and the electric field are constant within each subvolume. The only exception arises for the integration of the DGF over ΔV_i, where the principal value method is used [57]. Note that the validity of these approximations is discussed in Sec. III. Equation (6) then becomes:

$$\mathbf{E}_i = i\omega\mu_0\sum_{j\neq i}\overline{\overline{\mathbf{G}}}_{ij}\cdot\int_{\Delta V_j}\mathbf{J}(\mathbf{r}',\omega)dV' + \frac{i}{3\omega\varepsilon_0}[2(e^{ik_0a_i}(1-ik_0a_i)-1)-1] \times\left[\frac{1}{\Delta V_i}\int_{\Delta V_i}\mathbf{J}(\mathbf{r}',\omega)dV'\right] + \mathbf{E}_i^{inc}, \quad (7)$$

where $\overline{\overline{\mathbf{G}}}_{ij}$ is the free-space DGF between $\mathbf{r}_i$ and $\mathbf{r}_j$, and a_i [$=(3\Delta V_i/4\pi)^{1/3}$] is the effective radius of subvolume i. When evaluating the integration over ΔV_i in Eq. (6), two assumptions are made. First, the current $\mathbf{J}$ inside subvolume i is approximated by its volumetric average. Second, when applying the principal value method, subvolume i is approximated as a sphere of equivalent volume. The validity of this approximation has been verified by comparison against an exact method [58]. A more rigorous approach for treating the singularity of the DGF can be found in Refs. [58,59].

Under the assumption that the subvolumes are small compared to the wavelength, it is reasonable to model a subvolume as an electric point dipole. A given subvolume i is therefore characterized by a total dipole moment $\mathbf{p}_i$ that is related to the equivalent current via the relation $\mathbf{p}_i = i\int_{\Delta V_i}\mathbf{J}(\mathbf{r}',\omega)dV'/\omega$ [60]. After substitution of Eq. (3), the following expression for the total dipole moment is determined:

$$\mathbf{p}_i = \Delta V_i\varepsilon_0(\varepsilon_i-1)\mathbf{E}_i + \frac{i}{\omega}\int_{\Delta V_i}\mathbf{J}^{fl}(\mathbf{r}',\omega)dV'. \quad (8)$$

The first term on the right-hand side of Eq. (8) is the induced dipole moment $\mathbf{p}_i^{ind}$ while the second term is the thermally fluctuating dipole moment $\mathbf{p}_i^{fl}$. Since the fluctuating current is converted into a thermally fluctuating dipole moment, it is more appropriate to express the fluctuation-dissipation theorem as follows:

$$\langle\mathbf{p}_i^{fl}(\omega)\otimes\mathbf{p}_i^{fl}(\omega')\rangle = \frac{4\varepsilon_0\varepsilon_i''\Delta V_i}{\pi\omega}\Theta(\omega,T)\delta(\omega-\omega')\overline{\overline{\mathbf{I}}}. \quad (9)$$

The main equation of the T-DDA is derived by writing Eq. (7) in terms of dipole moments:

$$\frac{1}{\alpha_i}\mathbf{p}_i - \frac{k_0^2}{\varepsilon_0}\sum_{j\neq i}\overline{\overline{\mathbf{G}}}_{ij}\cdot\mathbf{p}_j = \frac{3}{(\varepsilon_i+2)}\frac{1}{\alpha_i^{CM}}\mathbf{p}_i^{fl} + \mathbf{E}_i^{inc}. \quad (10)$$

The variables α_i^{CM} and α_i are the Clausius–Mossotti and radiative polarizabilities of dipole i given by:

$$\alpha_i^{CM} = 3\varepsilon_0\Delta V_i\frac{\varepsilon_i-1}{\varepsilon_i+2}, \quad (11a)$$

$$\alpha_i = \frac{\alpha_i^{CM}}{1-(\alpha_i^{CM}/2\pi\varepsilon_0a_i^3)[e^{ik_0a_i}(1-ik_0a_i)-1]}, \quad (11b)$$

Note that the fluctuation-dissipation theorem for the fluctuating dipole moment given by Eq. (9) is different from the expression previously reported in the literature [55]. This is explained by the fact that the induced dipole moment due to the interaction of subvolume i with itself is implicitly included in the fluctuation-dissipation theorem of Ref. [55]. In the current formulation, the induced dipole moment due to self-interaction of subvolume i is accounted for in the first term on the left-hand side of Eq. (10). It is shown in the Appendix that the fluctuation-dissipation theorem given by Eq. (9) combined with Eq. (10) is equivalent to the formulation presented in Ref. [55].

Equation (10) is a system of $3N$ scalar equations that can be written in a compact matrix form as follows:

$$\overline{\overline{\mathbf{A}}}\cdot\overline{\mathbf{P}} = \overline{\mathbf{E}}^{fdt} + \overline{\mathbf{E}}^{inc}, \quad (12)$$

where $\overline{\overline{\mathbf{A}}}$ is the $3N$ by $3N$ deterministic interaction matrix [35], $\overline{\mathbf{E}}^{fdt}$ is a $3N$ stochastic column vector containing the first term on the right-hand side of Eq. (10) and its correlation matrix is obtained using the fluctuation-dissipation theorem, $\overline{\mathbf{E}}^{inc}$ is a $3N$ deterministic column vector containing the incident field and $\overline{\mathbf{P}}$ is a $3N$ stochastic column vector containing the unknown total dipole moments.

The monochromatic power dissipated in the absorbers is given by [37,61]:

$$\langle Q_{abs,\omega}\rangle = \frac{\omega}{2}\sum_{i\in abs}\left(\mathrm{Im}\left[\left(\alpha_i^{-1}\right)^*\right]-\frac{2}{3}k_0^3\right)\mathrm{tr}\langle\mathbf{p}_i^{ind}\otimes\mathbf{p}_i^{ind}\rangle, \quad (13)$$

where the superscript * denotes complex conjugate while $\mathrm{tr}\langle \mathbf{p}_i^{ind} \otimes \mathbf{p}_i^{ind*} \rangle$ is the trace of the autocorrelation function of the induced dipole moment of subvolume i. The summation in Eq. (13) is performed strictly over the subvolumes contained within the absorbers. Since the absorbers are at a temperature of 0 K, $\mathbf{p}_i^{fl} = \mathbf{0}$ and $\langle \mathbf{p}_i \otimes \mathbf{p}_j \rangle = \langle \mathbf{p}_i^{ind} \otimes \mathbf{p}_j^{ind*} \rangle$ such that Eq. (13) can be calculated directly from the system of equations (12). The trace of the autocorrelation function of the total dipole moment is determined using the correlation matrix of $\overline{\mathbf{P}}$ obtained from Eq. (12) [35,62]:

$$\langle \overline{\mathbf{P}} \otimes \overline{\mathbf{P}}^{\dagger} \rangle = \overline{\overline{\mathbf{A}}}^{-1} \cdot \left(\langle \overline{\mathbf{E}}^{fdt} \otimes \overline{\mathbf{E}}^{fdt\dagger} \rangle + \langle \overline{\mathbf{E}}^{inc} \otimes \overline{\mathbf{E}}^{inc\dagger} \rangle \right) \cdot \left(\overline{\overline{\mathbf{A}}}^{-1} \right)^{\dagger}, \tag{14}$$

where the superscript † is the Hermitian operator. The fact that $\overline{\mathbf{E}}^{fdt}$ and $\overline{\mathbf{E}}^{inc}$ are uncorrelated (i.e., $\langle \mathbf{E}^{fdt} \otimes \mathbf{E}^{inc\dagger} \rangle = \overline{\overline{\mathbf{0}}}$) has been used when deriving Eq. (14). The correlation matrix $\langle \overline{\mathbf{E}}^{fdt} \otimes \overline{\mathbf{E}}^{fdt\dagger} \rangle$ is derived by applying the fluctuation-dissipation theorem given by Eq. (9).

The difference between the T-DDA framework described here and in Ref. [35] comes from the splitting of the fluctuating field and the incident field. In this paper, the incident field represents solely the field produced by external sources. Additionally, the system of equations (12) is written in terms of total dipole moments rather than in terms of induced dipole moments.

As a final remark, it is important to recognize that the system of equations (12) is stochastic and can be solved in different ways. Hereafter, the computations are performed in a deterministic manner by calculating directly the dipole autocorrelation function from Eq. (14). Alternatively, Eq. (12) can be solved directly by assuming that only one subvolume is thermally emitting while all other subvolumes are at a temperature of 0 K. These calculations need to be repeated for each subvolume contained in the emitters, and the dipole autocorrelation function can thus be determined. The correlation matrix method is attractive as it does not involve multiple solutions of a system of equations. On the other hand, this methodology is computationally expensive due to large memory requirements when dealing with a large number of subvolumes. More details on this topic will be provided in Sec. IV.

III. APPROXIMATIONS ASSOCIATED WITH THE T-DDA

Following the derivation presented in Sec. II, the approximations made in the T-DDA can be summarized into four points.

(i) *Discretization of the objects into cubical subvolumes.* The error introduced by this approximation is called the shape error [39,44]. The shape error is nonexistent for objects that can be represented exactly by a cubical lattice such as a cube [44], while it can be large for curved objects such as a sphere. The shape error for multiple objects closely spaced from each other, or in contact, is larger than for a single object. As discussed later, this is related to the importance of representing accurately the gap size between discretized objects. The extent to which the shape error negatively affects the accuracy of the results is a strong function of the refractive index of the object [39]. A large refractive index implies a high contrast between the object and the free space, which amplifies the shape error. Approximating objects by a cubical lattice is valid when the size of the subvolumes is small compared to the characteristic lengths of the problem, namely the size of the objects and their separation distance.

(ii) *Constant electric field in each subvolume.* Radiative heat transfer in the near field occurs via propagating and evanescent modes. When dealing with propagating modes, approximating the electric field as constant within a subvolume is acceptable when the size of the subvolume is smaller than the free-space wavelength (λ), smaller than the material wavelength [$\lambda_m = \lambda/\mathrm{Re}(m)$], and smaller than the decay length of the electric field [$\lambda/\mathrm{Im}(m)$]. For evanescent modes, the approximation of constant electric field within a subvolume is acceptable when the size of the subvolume is small compared to the radiation penetration depth. The penetration depth of evanescent modes ranges from λ_m to the thickness of the gap separating the objects. Furthermore, for objects with sharp edges such as cubes, the size of the subvolumes must be small compared to the characteristic length of the object, even if the object is much smaller than the wavelength. This ensures that the large electric field gradients near the edges are accurately represented [53].

(iii) *Constant free-space DGF inside each subvolume.* The variations of the free-space DGF $\overline{\overline{\mathbf{G}}}(\mathbf{r},\mathbf{r}',\omega)$ inside the objects are proportional to λ/R, where R is the distance between points $\mathbf{r}$ and $\mathbf{r}'$ [59]. When the size of the object is much smaller than the wavelength (Rayleigh regime), sharp variations of the free-space DGF arise inside the object. As such, the validity of this assumption becomes questionable in the Rayleigh regime [58]. In addition, the free-space DGF in Eq. (10) is multiplied by the dielectric function ε, such that the accuracy of this approximation degrades with increasing the refractive index m ($m = \sqrt{\varepsilon}$).

(iv) *Integration of the free-space DGF, $\overline{\overline{\mathbf{G}}}(\mathbf{r}_i,\mathbf{r}',\omega)$, over the subvolume ΔV_i where the singularity of the DGF is located [second term on the right-hand side of Eq. (6)].* To be able to perform the principal volume integral analytically, the cubical subvolume i is approximated by a sphere of equivalent volume [57,63]. The radiative polarizability discussed in Sec. II [Eq. (11b)] is a result of this assumption [35]. Rather than performing the principal volume integration, different polarizability models based on physical arguments have been proposed [39,64–69].

The impact of these approximations on the accuracy of the T-DDA depends on the specific parameters of the problem. This is discussed in the next section.

IV. ACCURACY OF THE T-DDA

The accuracy of the T-DDA is assessed by comparison against exact results for two spheres [23–25]. As shown in Fig. 1, two spheres of same diameter D and same refractive index m are separated by a distance $X(y,z)$ and are exchanging thermal radiation in the free space. The minimum gap size between the spheres is denoted by $d\,[=X(0,0)]$. For simplicity, it is assumed that there is no incident field. Sphere 1 is at a temperature $T + \delta T$, while sphere 2 is maintained

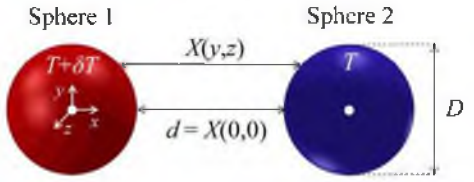

FIG. 1. (Color online) Schematic of the problem under consideration: two spheres of diameter D separated by a distance $X(y,z)$ are exchanging thermal radiation. The minimum distance between the spheres is $d\,[=X(0,0)]$.

at a temperature T. The spectral thermal conductance at temperature T and angular frequency ω is given by:

$$G_\omega(T) = \lim_{\delta T \to 0} \frac{\langle Q_{net,\omega} \rangle}{\delta T}, \tag{15}$$

where $\langle Q_{net,\omega} \rangle = \langle Q_{abs,\omega,12} \rangle - \langle Q_{abs,\omega,21} \rangle$ is the net spectral heat rate. The power dissipated in sphere 2 due to thermal emission by sphere 1, $\langle Q_{abs,\omega,12} \rangle$, is calculated from Eq. (13). Due to reciprocity, the power dissipated in sphere 1 due to thermal emission by sphere 2 can be computed as $\langle Q_{abs,\omega,21} \rangle = \langle Q_{abs,\omega,12} \rangle \frac{\Theta(\omega,T)}{\Theta(\omega,T+\delta T)}$. Therefore, the spectral conductance at temperature T is obtained solely from $\langle Q_{abs,\omega,12} \rangle$:

$$G_\omega(T) = \frac{\langle Q_{abs,\omega,12} \rangle}{\Theta(\omega,T)} \frac{\partial \Theta(\omega,T)}{\partial T}. \tag{16}$$

Hereafter, sphere 1 is referred to as the emitter while sphere 2 is called the absorber. The spectral thermal conductance is calculated at a temperature of 300 K and at an angular frequency of 1.884×10^{14} rad/s. This corresponds to a vacuum wavelength of 10 μm, which is roughly the dominant wavelength emitted by a body at 300 K.

Approximate solutions for the two-sphere problem have been proposed in the literature for two limiting cases. The proximity approximation is applicable when the size of the spheres is much larger than their separation gap ($D \gg d$) [25,27]. For this case, the conductance between the spheres is calculated as a summation of local heat transfer coefficients between two semi-infinite media separated by different gap sizes. The second limiting case is the dipole approximation, which is valid when the size of the spheres is much smaller than the wavelength while their separation gap is a few times larger than their diameter ($D \ll \lambda$ and $d \gg D$) [55]. In the dipole approximation, the contributions from the quadrupoles and higher order poles as well as multiple scattering between the spheres are neglected. The Appendix demonstrates that the T-DDA reduces to the dipole approximation when $D \ll \lambda$ and $d \gg D$.

The accuracy of the T-DDA is evaluated for three sizes, $k_0 D \ll 1$, $k_0 D \approx 1$, and $k_0 D \gg 1$. For each size, various gap distances in the near-field regime of thermal radiation (i.e., $d < \lambda$) are considered. Overall, a total of seven cases, summarized in Table I, are investigated. For each case listed in Table I, the convergence of the T-DDA is analyzed for six different refractive indices (see Table II), including high and low real and imaginary parts, and a refractive index corresponding to surface phonon-polariton resonance of a silica sphere. The spectral thermal conductance between the spheres is calculated with the T-DDA using various discretization sizes and is compared against exact results. All computations were performed with a hybrid OpenMP-MPI parallel T-DDA FORTRAN code utilizing the SCALAPACK library as implemented in the Intel Math Kernel Library for the interaction matrix inversion. The computational time for the largest number of subvolumes used in case 1 (73 824) is approximately 18.7 hours when run on 150 nodes each having two six-core Intel Xeon X5660 processors with a speed of 2.80 GHz. This amounts in a total of 33 660 service units (i.e., core hours). Note that 99.8% of the aforementioned time is devoted to the calculation of the inverse of the interaction matrix.

TABLE I. Cases investigated in the convergence analysis.

	$k_0 D$ (D)	d/λ (d)
Case 1	0.00 628 (10 nm)	0.00 100 (10 nm)
Case 2	0.0943 (150 nm)	0.00 100 (10 nm)
Case 3	0.0943 (150 nm)	0.0150 (150 nm)
Case 4	1.01 (1.6 μm)	0.00 100 (10 nm)
Case 5	1.01 (1.6 μm)	0.100 (1 μm)
Case 6	5.03 (8 μm)	0.0100 (100 nm)
Case 7	5.03 (8 μm)	0.500 (5 μm)

A. Regime $k_0 D \ll 1$

Two sizes, namely $k_0 D = 0.00\,628$ ($D = 10$ nm) and $k_0 D = 0.0943$ ($D = 150$ nm), are investigated. A gap thickness of $d/\lambda = 0.001$ ($d = 10$ nm) is selected for $k_0 D = 0.00\,628$ (case 1 in Table I). Larger gaps correspond to the dipolar regime for which a closed-form expression exists (see Appendix) [55], while the validity of the fluctuational electrodynamics framework is questionable at sub-10-nm gaps. Two gap sizes of $d/\lambda = 0.001$ ($d = 10$ nm) and $d/\lambda = 0.015$ ($d = 150$ nm) are tested for $k_0 D = 0.0943$ (cases 2 and 3 in Table I, respectively).

The absolute value of the relative error of the conductance as a function of the number of subvolumes per sphere and the refractive index is provided in Fig. 2 for case 1. The dashed line shows the 5% error threshold. It can be seen that for all refractive indices, describing a sphere by a single subvolume results in an error of approximately 30% even if $D \ll \lambda$. This is due to the shape error and the non-negligible variation of the electric field inside the spheres. The shape error is caused by an inaccurate representation of the separation distance $X(y,z)$ between the spheres that is fixed at 10 nm, while, in reality, it should vary from 10 to 20 nm. Clearly, the subvolume size to

TABLE II. Refractive indices investigated in the convergence analysis.

m_a (ε_a)	$1.33 + 0.01i$ ($1.77 + 0.0266i$)
m_b (ε_b)	$1.33 + 1i$ ($0.769 + 2.66i$)
m_c (ε_c)	$3 + 0.01i$ ($9 + 0.06i$)
m_d (ε_d)	$3 + 1i$ ($8 + 6i$)
m_e (ε_e)	$3 + 3i$ ($0 + 18i$)
m_f (ε_f)	$0.53 + 1.28i$ ($-1.36 + 1.36i$)

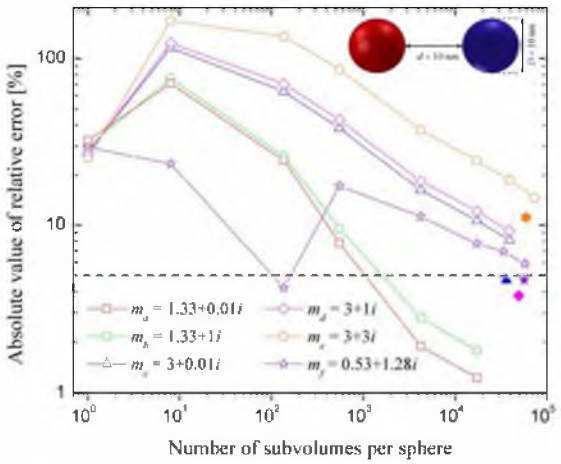

FIG. 2. (Color online) Absolute value of the relative error of the conductance as a function of the number of subvolumes and the refractive index for case 1 ($k_0D = 0.00\,628$, $d/\lambda = 0.001$). Open and filled symbols denote the error for uniform and nonuniform discretizations, respectively.

gap ratio, Δ/d, should be much smaller than unity in order to minimize the shape error. Additionally, heat transfer in case 1 is dominated by exponentially decaying evanescent modes with minimum penetration depth approximately equal to the gap size d. This results in sharp variations of the electric field within the spheres with diameter D equals to d. The variation of the electric field is obviously not taken into account when modeling a sphere by a single subvolume. As for the shape error, the ratio Δ/d must be much smaller than unity in order to represent accurately the variation of the electric field within the spheres. Physically, this error can be understood by recognizing that when $d \gg D$ is not satisfied, the multipoles inside the spheres are excited by the evanescent modes [70] such that the dipole approximation is inapplicable. When d/λ is increased to 10 ($d = 100$ μm), which results in a ratio Δ/d of 0.000 080 6, describing each sphere by a single subvolume leads to a small error of 0.01% (result not shown). This is to be expected, since the 10 nm variations of the distance $X(y,z)$ between the spheres along the y and z axis are insignificant compared to the gap d of 100 μm. Additionally, the electric field within the spheres is nearly uniform as heat transfer occurs via propagating modes and $D \ll \lambda$.

In Fig. 2, the error grows as the number of subvolumes is increased from one to eight, and then decreases as the number of subvolumes is further increased. This counterintuitive behavior has also been observed for a large gap size of $d/\lambda = 10$ and for DDA simulations of a single sphere of size $k_0D = 0.00\,628$ (results not shown). The shape error and the error associated with the assumption of constant electric field within the subvolumes both decrease when increasing the number of subvolumes. However, an additional error caused by the sharp variation of the free-space DGF inside the spheres comes into picture. The free-space DGF between points $\mathbf{r}_i$ and $\mathbf{r}_j$, $\overline{\overline{\mathbf{G}}}_{ij}$, varies rapidly as $\mathbf{r}_j$ approaches $\mathbf{r}_i$ and becomes singular when $\mathbf{r}_i = \mathbf{r}_j$. Since the spheres are much smaller than the wavelength, the points $\mathbf{r}_i$ and $\mathbf{r}_j$ are always close to each other, which results in sharp variations of the DGF throughout the entire spheres. The variations of the free-space DGF within small objects do not introduce any error in the T-DDA when a single subvolume per sphere is used, as the integration of the DGF over the subvolume is performed analytically [see Eq. (7)]. The variations of the free-space DGF induce an error when modeling the objects with more than one subvolume. Note that this error was also observed in Refs. [37,58] when applying the DDA to Rayleigh particles. Chaumet *et al.* [58] showed that performing the integration of the free-space DGF over the subvolumes, instead of assuming constant free-space DGF, improves the accuracy of the DDA for very small spherical particles. The assumption of constant free-space DGF inside the subvolumes, and therefore the T-DDA results, become more accurate as the number of subvolumes increases.

As expected, the error strongly depends on the refractive index of the material. The error grows as both the real and the imaginary parts of the refractive index increase. In general, increasing the refractive index negatively affects the accuracy of the T-DDA by amplifying the shape error [39], by amplifying the error associated with assuming the free-space DGF constant within the subvolumes, and by increasing the variation of the electric field inside the spheres. For case 1, the fact that the error increases with increasing the refractive index is mostly due to the amplification of the shape error and the variation of the DGF; the refractive index has only a small influence on the variation of the electric field within the spheres since this variation is caused by evanescent modes with minimum penetration depth approximately equal to the gap size d. The amplification of the shape and constant DGF errors with increasing the refractive index can be mitigated by increasing the number of subvolumes, as shown in Fig. 2. The refractive index m_f corresponds to surface phonon-polariton resonance of a silica sphere. In the near field, the total thermal conductance is largely dominated by the contribution of surface phonon polaritons [23]. Here, the conductance for m_f is one to six orders of magnitude larger than the conductance calculated for the refractive indices m_a to m_e. As depicted in Fig. 2, the T-DDA converges rapidly for the resonant refractive index. Furthermore, the spectral locations of the resonant modes are predicted accurately via the T-DDA [35]. This demonstrates that the T-DDA is an accurate tool for predicting surface phonon-polariton mediated near-field radiative heat transfer.

In case 1, errors of 1.2% and 1.8% are obtained using 17 256 subvolumes for m_a and m_b, respectively. Reducing the error to less than 5% for other refractive indices requires a larger number of subvolumes. The number of subvolumes used for the simulations is limited by the memory requirement for storing the interaction matrix $\overline{\overline{\mathbf{A}}}$. For N subvolumes, $144N^2$ bytes of memory are needed to store $9N^2$ complex elements of the interaction matrix with a double precision format. The size of the subvolumes Δ decreases with N as $\Delta \propto N^{-1/3}$. This implies that the memory requirement is proportional to Δ^{-6}. Additionally, the computational time, which is almost equal to the calculation time of the inverse of $\overline{\overline{\mathbf{A}}}$, is approximately proportional to N^3. A significant amount of computational resources are therefore required when a large number of subvolumes are used. A solution to this bottleneck

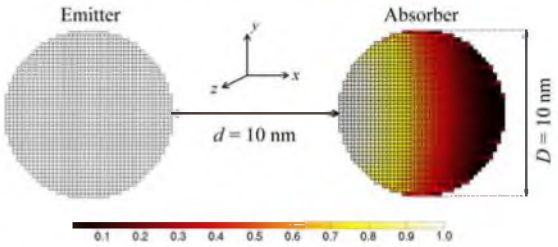

FIG. 3. (Color online) Spatial distribution of the normalized volumetric power absorbed for case 1 (refractive index m_e, 39 024 uniform subvolumes).

is the implementation of a nonuniform discretization scheme. Indeed, depending on the problem, some portions of the spheres may have negligible contribution to the overall heat transfer. A cross section of the spatial distribution of the normalized volumetric power absorbed by sphere 2 is shown in Fig. 3 for the refractive index m_e and for 39 024 uniform subvolumes. The cross section is parallel to the x-y plane and passes through the center of the sphere. For this case, more than 85% and 95% of the absorption takes place within distances of 6.18 nm and 7.84 nm from the left edge of the absorbing sphere, respectively. Also, the shape error is more important for the portion of the absorber facing the emitter. Based on the power distribution of Fig. 3, a nonuniform discretization with 36 168 subvolumes is proposed in Fig. 4, where the size of the subvolumes increases as the power absorbed decreases. The error obtained with 36 168 nonuniform subvolumes per sphere is 4.7%, as opposed to 8.16% when using 39 024 uniform subvolumes per sphere. Clearly, a nonuniform discretization scheme helps achieving a smaller error for a fixed number of subvolumes. The distribution of the fine and coarse subvolumes in a nonuniform discretization depends on the physics of the problem. Performing a preliminary simulation using a reasonable amount of uniform subvolumes (e.g., 5000) is helpful for visualizing the power distribution and thus defining an adequate nonuniform meshing. Nonuniform discretization has also been applied to refractive indices m_d to m_f. Note that the error values reported in all figures are shown with open symbols when uniform discretization is utilized, while filled symbols are used for nonuniform discretization. Errors less than 5% are achieved for m_d and m_f using nonuniform discretization. The smallest error obtained for m_e is 11.1% with 59 360 nonuniform subvolumes. It should be noted that both the real and the imaginary parts of m_e are large. Therefore, the shape error and the variation of the free-space DGF are larger for m_e than for the other refractive indices.

The absolute value of the relative error for case 2 is plotted in Fig. 5. Compared to case 1, the size of the spheres is increased while the separation gap d is the same. The error follows the same trend as in case 1. However, for a given number of subvolumes, the errors in Fig. 5 are considerably larger than in case 1 except for the resonant refractive index m_f. Increasing the ratio D/d while keeping the number of subvolumes fixed results in a larger discretization size such that the accuracy

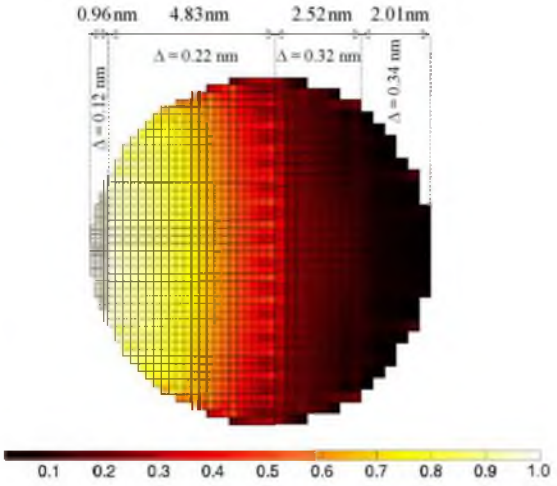

FIG. 4. (Color online) Spatial distribution of the normalized volumetric power absorbed for case 1 (refractive index m_e, 36 168 nonuniform subvolumes); the size of the subvolumes increases as the power absorbed decreases.

of all approximations listed in Sec. III deteriorates. Modeling each sphere by a single subvolume also leads to larger errors when compared to case 1, due to the fact that the shape error and the variation of the electric field within the spheres increase as the ratio D/d increases (for a fixed number of subvolumes, Δ/d increases when compared to case 1). As for case 1, the thermal conductance at resonance is well predicted by the T-DDA and an error of 2.0% is achieved with 33 552

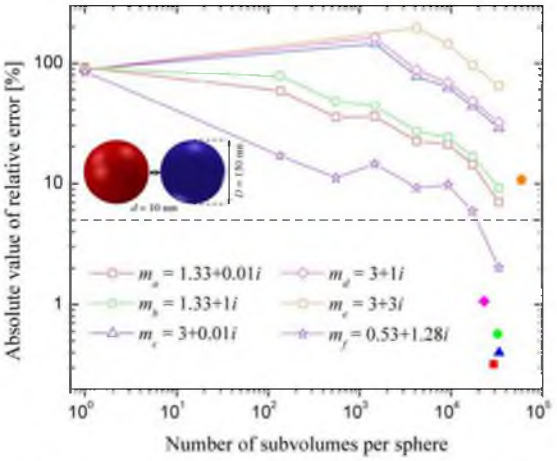

FIG. 5. (Color online) Absolute value of the relative error of the conductance as a function of the number of subvolumes and the refractive index for case 2 ($k_0D = 0.0943$, $d/\lambda = 0.001$). Open and filled symbols denote the error for uniform and nonuniform discretizations, respectively.

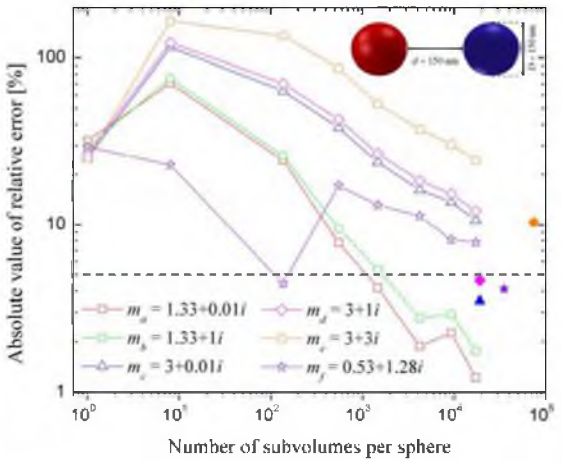

FIG. 6. (Color online) Absolute value of the relative error of the conductance as a function of the number of subvolumes and the refractive index for case 3 ($k_0D = 0.0943$, $d/\lambda = 0.015$). Open and filled symbols denote the error for uniform and nonuniform discretizations, respectively.

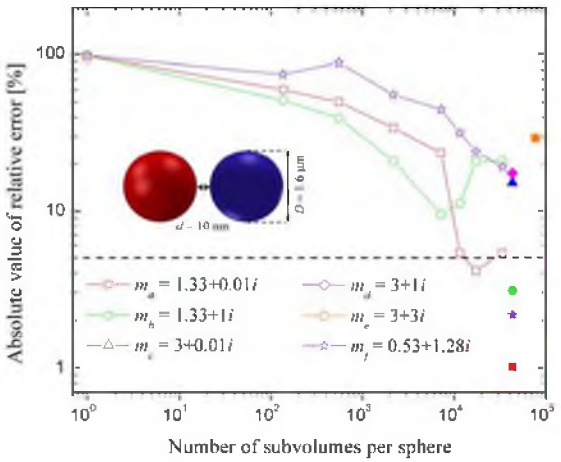

FIG. 7. (Color online) Absolute value of the relative error of the conductance as a function of the number of subvolumes and the refractive index for case 4 ($k_0D = 1.01$, $d/\lambda = 0.001$). Open and filled symbols denote the error for uniform and nonuniform discretizations, respectively.

uniform subvolumes per sphere. Nonuniform discretization is adopted for the other refractive indices. An error less than 5% is achieved for the refractive indices m_a to m_d when using up to 33 740 nonuniform subvolumes. For the largest refractive index m_e, the error reduces from 64.9% with 33 552 uniform subvolumes to 10.7% with 59 408 nonuniform subvolumes. A better accuracy can be obtained for m_e by increasing further the numbers of subvolumes. For all refractive indices considered in case 2, more than 95% of the absorption occurs within the first half of the sphere. This shows that as the ratio D/d increases, a smaller portion of the absorber contributes to the overall heat exchange, since radiative transfer is dominated by evanescent modes with minimum penetration depth d that is much smaller than the sphere diameter D. As such, nonuniform discretization can effectively be utilized in this situation.

Next, the gap thickness is increased to $d/\lambda = 0.015$ while the size is kept constant at $k_0D = 0.0943$ (case 3). The absolute value of the relative error is shown in Fig. 6. It can be seen that the error obtained in case 3 is very similar to case 1. Indeed, in both cases 1 and 3, radiative transfer is dominated by evanescent modes ($d \ll \lambda$) and the sphere diameter to gap ratio, D/d, is the same. This implies that the shape error and the error associated with the assumption of constant electric field within the subvolumes introduce the same amount of inaccuracy in cases 1 and 3 as the ratios Δ/d and Δ/D are the same for a fixed number of subvolumes. Additionally, the error associated with assuming the free-space DGF as constant inside the subvolumes is still important since $D \ll \lambda$. An error less than 5% is obtained for m_a and m_b when 17 256 uniform subvolumes are used. For the other refractive indices, nonuniform discretization has been applied. The error reduces to less than 5% for refractive indices m_c, m_d, and m_f with up to 35 256 nonuniform subvolumes. As in the previous cases, the most difficult refractive index to handle is m_e for which an error of 10.3% is achieved using 74 180 nonuniform subvolumes.

B. Regime $k_0D \approx 1$

The convergence of the T-DDA is analyzed for $k_0D = 1.01$ ($D = 1.6$ μm) and two gap sizes of $d/\lambda = 0.001$ ($d = 10$ nm) and $d/\lambda = 0.1$ ($d = 1$ μm), corresponding to cases 4 and 5, respectively. The absolute value of the relative error for case 4 is shown in Fig. 7, where up to 33 552 uniform subvolumes per sphere are used. For this number of uniform subvolumes and for the refractive indices m_c, m_d, and m_e, the error is extremely large; as such, these points are not plotted in Fig. 7. This behavior can be explained by analyzing the discretized spheres shown in Fig. 8(a). Clearly, the size of the subvolumes is too large for a 10-nm-thick gap ($\Delta/d = 4.0$), such that the shape error is significant. The discretization of the spheres should be fine enough compared to the gap size ($\Delta/d \ll 1$) in order to represent accurately the smooth variation of $X(y,z)$ with respect to the y and z axis. A nonuniform discretization using smaller subvolumes at the front sides of the spheres is thus beneficial. This is particularly helpful because the size of the spheres is much larger than the gap size ($D/d = 160$) such that only a small portion of the absorber contributes to the overall heat transfer (more than 95% of the absorption takes place within a distance smaller than 240 nm for all refractive indices). A nonuniform discretization with 43 324 subvolumes is applied to case 4 and is shown in Fig. 8(b), where $\Delta/d = 0.4$ for $d = 10$ nm. The variation of $X(y,0)$ between the discretized spheres along the y axis for the uniform and nonuniform discretizations is shown in Fig. 8(c). The distance $X(y,0)$ varies in a smoother manner with the nonuniform discretization scheme compared to the uniform discretization. Consequently, by decreasing the shape error, the accuracy of the T-DDA is drastically improved. With the nonuniform

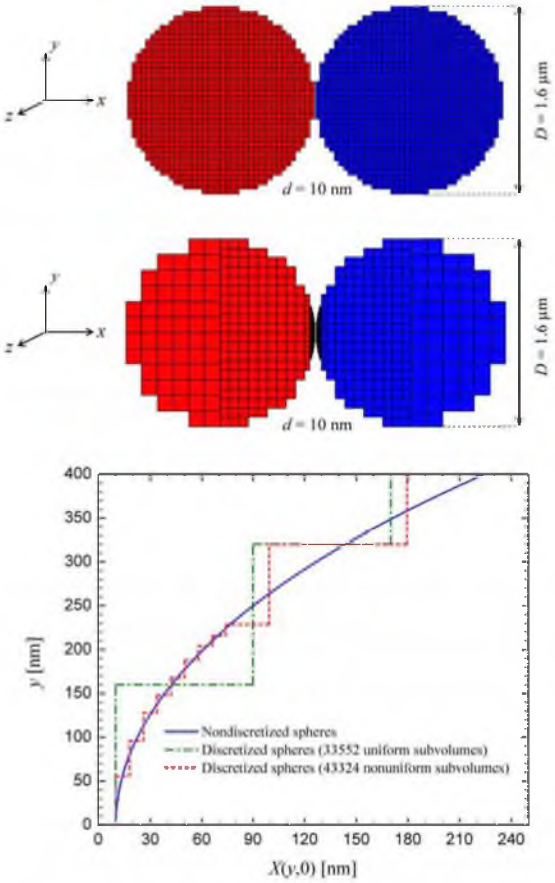

FIG. 8. (Color online) Two spheres of diameter $D = 1.6$ μm separated by a gap size $d = 10$ nm are discretized using (a) 33 552 uniform subvolumes, and (b) 43 324 nonuniform subvolumes. (c) Variation of the distance between the spheres, $X(y,0)$, along the y axis for the uniform and nonuniform discretizations shown in (a) and (b).

discretization, an error less than 3.1% is obtained for m_a, m_b, and m_f. Also, compared to the uniform discretization with 33 552 subvolumes, the error reduces from 310 to 15.2% for m_c, from 333 to 17.5% for m_d and from 868 to 40.5% for m_e. The error for m_e is decreased further to 29.5% using 77 196 nonuniform subvolumes. It is worth noting that for the small refractive index m_a, an error of 5.4% is achieved with a simple uniform discretization of 33 552 subvolumes ($\Delta/d = 4.0$). Therefore, it can be concluded that the value of Δ/d required for convergence depends strongly on the refractive index of the material. This is in agreement with the observation made in the DDA that the shape error is a function of the refractive index [39].

The absolute value of the relative error for case 5 is presented in Fig. 9. Compared to case 4, the gap size is increased while the sphere size is the same (D/d is 1.6 instead of 160). The error in case 5 is between 3.8 to 92 times smaller

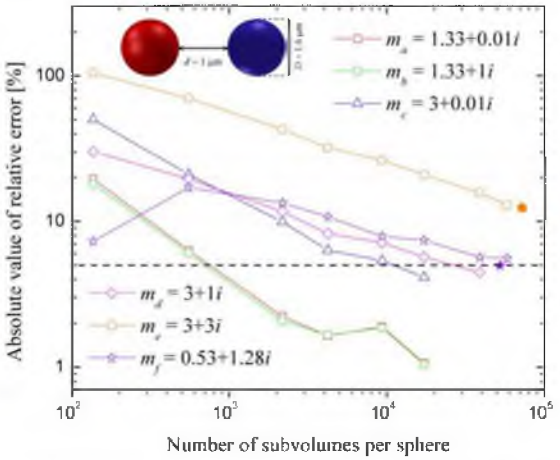

FIG. 9. (Color online) Absolute value of the relative error of the conductance as a function of the number of subvolumes and the refractive index for case 5 ($k_0 D = 1.01$, $d/\lambda = 0.1$). Open and filled symbols denote the error for uniform and nonuniform discretizations, respectively.

than in case 4, depending on the refractive index, when 17 256 uniform subvolumes are used (Δ/d decreases from 5.0 to 0.05 compared to case 4). This confirms that the shape error is dominant when dealing with large sphere diameter to gap ratio D/d in the near-field regime of thermal radiation. An error less than 5% is achieved for m_a to m_d when using up to 39 024 uniform subvolumes. With a nonuniform discretization, the errors for m_e and m_f are respectively 12.4% (72 264 subvolumes) and 5.0% (52 388 subvolumes).

C. Regime $k_0 D \gg 1$

A size of $k_0 D = 5.03$ ($D = 8$ μm) and two gap thicknesses of $d/\lambda = 0.01$ ($d = 100$ nm) and $d/\lambda = 0.5$ ($d = 5$ μm) are considered (cases 6 and 7, respectively). Note that case 7 corresponds to the transition between the near- and far-field regimes of thermal radiation. The spatial distribution of the power absorbed for cases 6 and 7 is quite different from the previous problems analyzed. Here, the absorption distribution depends strongly on the imaginary part of the refractive index. The normalized volumetric power absorbed in case 6 for the refractive indices m_c and m_d, which have the same real part but have different imaginary parts, are compared in Fig. 10 when 33 552 uniform subvolumes per sphere are used. It is important to note that even if the gap d is much smaller than the wavelength λ in case 6, propagating modes have a non-negligible contribution to heat transfer since the distance $X(y,z)$ between the spheres varies from 100 nm (near-field) to 8.1 μm (~ far-field). When the imaginary part of the refractive index is large, most of the absorption occurs within the first half of the sphere [Fig. 10(b)]. However, the contributing portion of the absorber to the overall heat transfer is larger than for cases 1 to 5 due to the important contribution of propagating modes with larger penetration depth than the evanescent modes. For example, in case 4, where $D/d = 160$ ($D = 1.6$ μm), more

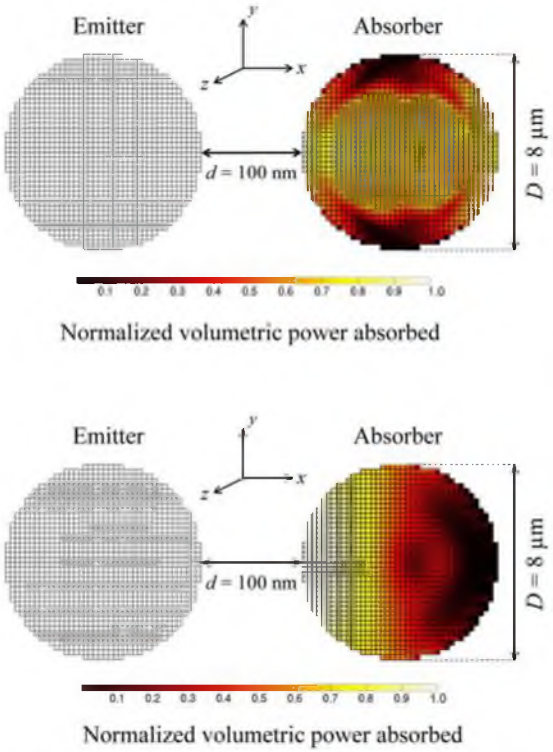

FIG. 10. (Color online) Spatial distribution of the normalized volumetric power absorbed for case 6 (33 552 uniform subvolumes): (a) Refractive index $m_c = 3 + 0.01i$, and (b) refractive index $m_d = 3 + 1i$.

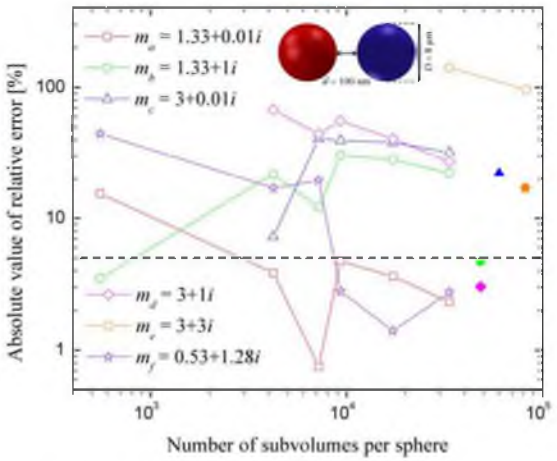

FIG. 11. (Color online) Absolute value of the relative error of the conductance as a function of the number of subvolumes and the refractive index for case 6 ($k_0 D = 5.03$, $d/\lambda = 0.01$). Open and filled symbols denote the error for uniform and nonuniform discretizations, respectively.

than 95% of the power is absorbed within the first 200 nm of the absorber with m_d. In case 6, where $D/d = 80$ ($D = 8$ μm), this distance is equal to 4.4 μm with m_d. When the imaginary part of the refractive index is small, a different pattern is observed in the power distribution [Fig. 10(a)]. For this case, the whole sphere contributes significantly to the overall heat transfer. This is because the thermally generated propagating waves experience multiple reflections within the sphere due to low absorption. Yet, it can be seen in Fig. 10(a) that significant absorption occurs within a small portion of the sphere facing the emitter due to evanescent modes with minimum penetration depth approximately equal to d. It is thus clear that the proximity approximation cannot be applied for cases where the imaginary part of the refractive index is small, since the absorber is optically thin. Additionally, nonuniform discretization for cases 6 and 7 is not as effective as for the previous cases, since a large portion of the absorber contributes to heat transfer. A fine discretization is thus required throughout the spheres. For this reason, cases 6 and 7 are difficult to handle with the T-DDA.

The absolute value of the relative error is shown in Fig. 11 for case 6. The errors for m_a and m_f are 2.3% and 2.75%, respectively, when 33 552 uniform subvolumes are used. This confirms that when $|m|$ is small, the T-DDA is accurate regardless of the parameters of the problem. The error grows rapidly as $|m|$ increases such that an error of 96.4% is obtained with 82 712 uniform subvolumes for m_e. Nonuniform discretization has been applied to refractive indices m_b through m_e. Since the gap size is small, a fine discretization is required at the front side of the spheres. Yet, a fine discretization also needs to be applied to the whole sphere (when the imaginary part of the refractive index is small) or to a large portion of the absorber (when the imaginary part of the refractive index is large). As shown in Fig. 11, the error reduces considerably when nonuniform discretization is used. Errors less than 5% are obtained for m_b and m_d using 48 367 nonuniform subvolumes. Furthermore, the error for m_e reduces to 17.0% with 81 980 nonuniform subvolumes. The smallest error obtained for m_c is 22.1% with 60 200 nonuniform subvolumes. The number of subvolumes used for m_c should be increased further if a better accuracy is desired.

The absolute value of the relative error for case 7 is provided in Fig. 12, where the gap size is increased to $d/\lambda = 0.5$ ($d = 5$ μm). As expected, the errors are considerably smaller than in case 6 due to the larger gap size which results in a smaller Δ/d and thus a smaller shape error. For the refractive indices m_a, m_b, and m_f, an error approximately equal to, or smaller than, 5% is obtained with 2176 uniform subvolumes per sphere. Nonuniform discretization has been applied to the other refractive indices. Since the distance between the spheres $X(y,z)$ vary between 5 μm and 13 μm, most of the energy is transferred by propagating modes such that there is a larger contribution from the back side of the absorber to the overall heat exchange when compared to case 6. For example, for the refractive index m_d, approximately 95% of the absorption happens within the first 7.4 μm of the absorber while this distance was equal to 4.4 μm in case 6. Therefore, the nonuniform discretization is not as efficient as in case 6. Errors of 3.8% (66 796 nonuniform subvolumes), 8.3% (67 472

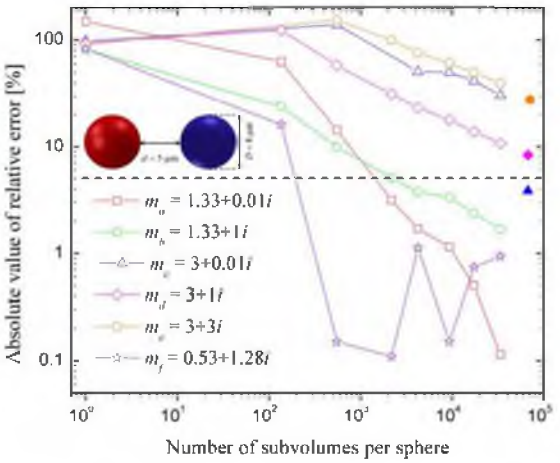

FIG. 12. (Color online) Absolute value of the relative error of the conductance as a function of the number of subvolumes and the refractive index for case 7 ($k_0 D = 5.03$, $d/\lambda = 0.5$). Open and filled symbols denote the error for uniform and nonuniform discretizations, respectively.

nonuniform subvolumes), and 27.8% (70 544 nonuniform subvolumes) are obtained for m_c, m_d, and m_e, respectively.

V. CONCLUSIONS

The accuracy and convergence of the T-DDA was analyzed using the exact solution for two spheres separated by a vacuum gap. The study was performed as a function of the size, the gap size, and the refractive index. The key results of the convergence analysis are summarized in Table III and the main conclusions are:

(i) An error less than 5% was obtained for 74% of the cases studied using up to 82 712 subvolumes.

(ii) Nonuniform discretization is particularly useful when the sphere diameter to gap ratio, D/d, is large, when $d \ll \lambda$, and $D < \lambda$, such that significant absorption occurs within a small portion of the sphere. Additionally, nonuniform discretization mitigates the shape error by allowing a better representation of the variation of the gap size by decreasing Δ/d at the front side of the spheres without increasing drastically the number of subvolumes. The value of Δ/d leading to a convergent solution varies strongly with the refractive index. For the simulations performed in this study, $\Delta/d \approx 1$ can be satisfactory for the smallest refractive index ($1.33 + 0.01i$) while $\Delta/d \approx 0.01$ is needed for the largest refractive index ($3 + 3i$).

(iii) For all sizes, the accuracy of the T-DDA decreases as both the real and the imaginary parts of the refractive index increase. A large refractive index affects the accuracy of the results by increasing the variation of the electric field and the free-space DGF inside the spheres and by amplifying the shape error. It was also shown that fast convergence is achieved when dealing with resonant modes. The T-DDA is therefore accurate for predicting surface phonon-polariton mediated near-field radiative heat transfer.

(iv) When the sphere diameter D and the gap size d have the same order of magnitude as the wavelength λ, nonuniform discretization is not as efficient as for the other cases. For this situation, the whole sphere contributes to the overall heat transfer such that a fine discretization is required throughout the entire volume of the absorber.

The conclusions of this paper are applicable to other geometries, except that the error is likely to be smaller due to a weaker shape error. The T-DDA is currently suitable for particles with sizes smaller than, or of the same order of magnitude as, the wavelength due to computational limitations. The accuracy of the T-DDA can potentially be improved further using the various techniques proposed in the DDA literature such as the weighted discretization approach [49,50] and the filtered coupled-dipole method [50–52]. This is left for a future research effort.

ACKNOWLEDGMENTS

This work was sponsored by the US Army Research Office under Grant No. W911NF-14-1-0210. The authors also acknowledge the Extreme Science and Engineering Discovery Environment (NSF Grant No. ACI-1053575) and the Center for High Performance Computing at the University of Utah for providing the computational resources used in this study. Financial support for T.T. and R.B. was provided by the Undergraduate Research Opportunities Program (UROP) at the University of Utah and by the NSF Research Experiences for Undergraduates (REU) program (Grant No. CBET-1253577), respectively.

TABLE III. Smallest relative error of the conductance obtained for all cases considered in the convergence analysis (N: number of subvolumes per sphere; U: uniform discretization; NU: nonuniform discretization).

	Case 1		Case 2		Case 3		Case 4		Case 5		Case 6		Case 7	
	N	Error (%)	N	Error (%)	N	Error (%)	N	Error (%)	N	Error (%)	N	Error (%)	N	Error (%)
m_a	17 256 (U)	1.23	29 340 (NU)	0.318	17 256 (U)	1.22	43 324 (NU)	1.01	17 256 (U)	1.06	33 552 (U)	2.31	33 552 (U)	0.115
m_b	17 256 (U)	1.79	32 572 (NU)	0.572	17 256 (U)	1.77	43 324 (NU)	3.08	17 256 (U)	1.04	48 368 (NU)	4.70	33 552 (U)	1.68
m_c	36 168 (NU)	4.70	33 740 (NU)	0.405	19 064 (NU)	3.50	43 324 (NU)	15.2	17 256 (U)	4.14	60 200 (NU)	22.1	66 796 (NU)	3.83
m_d	49 216 (NU)	3.80	23 080 (NU)	1.06	19 064 (NU)	4.62	43 324 (NU)	17.5	39 024 (U)	4.45	48 368 (NU)	3.03	67 472 (NU)	8.33
m_e	59 360 (NU)	11.1	59 408 (NU)	10.7	74 180 (NU)	10.3	77 196 (NU)	29.5	72 264 (NU)	12.4	81 980 (NU)	17.0	70 544 (NU)	27.8
m_f	56 500 (NU)	4.69	33 552 (U)	2.01	35 256 (NU)	4.10	43 324 (NU)	2.18	52 388 (NU)	4.99	33 552 (U)	2.75	33 552 (U)	0.931

APPENDIX: DERIVATION OF THE DIPOLE APPROXIMATION FROM THE T-DDA

In this Appendix, it is shown that the T-DDA applied to the two-sphere problem described in Sec. IV reduces to the dipole approximation when $D \ll \lambda$ and $d \gg D$ [55]. The first sphere is assumed to be at a temperature $T > 0$ K (emitter), while the second sphere is maintained at 0 K (absorber). In the dipolar regime, each sphere is modeled by a single subvolume behaving as an electric point dipole. The first subvolume is assigned to the emitting sphere, while the second one is allocated to the absorbing sphere. The quantity of interest is the power absorbed in sphere 2 calculated from Eq. (13) using the correlation matrix of the induced dipole moment. The (total) dipole moment in subvolume 2 is related to the (total) dipole moment in subvolume 1 by applying Eq. (10) to subvolume 2:

$$\mathbf{p}_2 = \frac{\alpha_2 k_0^2}{\varepsilon_0}\overline{\overline{\mathbf{G}}}_{21}\cdot\mathbf{p}_1, \tag{A1}$$

where $\mathbf{p}_2^{fl} = \mathbf{0}$ since subvolume 2 is nonemitting. Equation (A1) implies that the dipole moment in subvolume 2 is induced by the dipole moment in subvolume 1. The dipole moment in subvolume 1 is also determined using Eq. (10):

$$\mathbf{p}_1 = \frac{3\alpha_1}{(\varepsilon_1+2)\alpha_1^{CM}}\mathbf{p}_1^{fl} + \frac{\alpha_1 k_0^2}{\varepsilon_0}\overline{\overline{\mathbf{G}}}_{12}\cdot\mathbf{p}_2. \tag{A2}$$

According to Eq. (A2), the total dipole moment of subvolume 1 is the summation of the contributions from the thermally fluctuating dipole moment and the dipole moment induced by subvolume 2 (multiple scattering). In the dipolar regime, the second contribution is assumed to be negligible compared to the first one [55] such that the dipole moment of subvolume 1 is approximated by:

$$\mathbf{p}_1 \approx \frac{3\alpha_1}{(\varepsilon_1+2)\alpha_1^{CM}}\mathbf{p}_1^{fl}. \tag{A3}$$

Substituting Eq. (A3) into Eq. (A1) and applying the fluctuation-dissipation theorem, the ensemble average of the correlation matrix of the dipole moment of subvolume 2 is given by:

$$\langle \mathbf{p}_2 \otimes \mathbf{p}_2 \rangle \approx \frac{4k_0^4}{\pi\omega\varepsilon_0^2}|\alpha_2|^2\mathrm{Im}\left(\alpha_1^{CM}\right)\Theta(\omega,T)\overline{\overline{\mathbf{G}}}_{21}\cdot\left(\overline{\overline{\mathbf{G}}}_{21}\right)^{\dagger}, \tag{A4}$$

where $\mathbf{p}_2 = \mathbf{p}_2^{ind}$. The trace of the correlation matrix of the induced dipole moment in subvolume 2 is obtained using Eq. (A4) and by substituting the free-space DGF:

$$\mathrm{tr}\left(\langle \mathbf{p}_2^{ind} \otimes \mathbf{p}_2^{ind} \rangle\right) \approx \frac{\Theta(\omega,T)\mathrm{Im}\left(\alpha_1^{CM}\right)\left|\alpha_2^{CM}\right|^2 k_0^6}{2\pi^3\omega\varepsilon_0^2} \times \left|\frac{3}{[k_0(d+D)]^6} + \frac{1}{[k_0(d+D)]^4} + \frac{1}{[k_0(d+D)]^2}\right|. \tag{A5}$$

Note that when deriving Eq. (A5), it is assumed that $\alpha_i \approx \alpha_i^{CM}$ $(i = 1, 2)$. It can be seen from Eqs. (11a) and (11b) that as the size of a subvolume decreases, the radiative polarizability approaches the Clausius-Mossotti polarizability such that they are approximately equal in the dipolar regime. The power absorbed by sphere 2 is finally obtained by substituting Eq. (A5) into Eq. (13). Note that the term $(2/3)k_0^3$ in Eq. (13) has been ignored in some previous DDA formulations due to its small contribution [38,39]. Following the same procedure, the power absorbed in subvolume 2 is given by:

$$\langle Q_{abs,\omega}\rangle \approx \frac{1}{4\pi^3\varepsilon_0^2}\Theta(\omega,T)\mathrm{Im}\left(\alpha_1^{CM}\right)\mathrm{Im}\left(\alpha_2^{CM}\right)k_0^6 \times \left|\frac{3}{[k_0(d+D)]^6} + \frac{1}{[k_0(d+D)]^4} + \frac{1}{[k_0(d+D)]^2}\right|, \tag{A6}$$

which is the same as the power absorbed derived by Chapuis *et al.* [55] in the dipolar regime.

[1] B. Guha, C. Otey, C. B. Poitras, S. Fan, and M. Lipson, Nano Lett. **12**, 4546 (2012).
[2] Y. De Wilde, F. Formanek, R. Carminati, B. Gralak, P.-A. Lemoine, K. Joulain, J.-P. Mulet, Y. Chen, and J.-J. Greffet, Nature (London) **444**, 740 (2006).
[3] E. A. Hawes, J. T. Hastings, C. Crofcheck, and M. P. Mengüç, Opt. Lett. **33**, 1383 (2008).
[4] V. L. Y. Loke and M. P. Mengüç, J. Opt. Soc. Am. A **27**, 2293 (2010).
[5] C. R. Otey, W. T. Lau, and S. Fan, Phys. Rev. Lett. **104**, 154301 (2010).
[6] S. Basu and M. Francoeur, Appl. Phys. Lett. **98**, 113106 (2011).
[7] A. Babuty, K. Joulain, P.-O. Chapuis, J.-J. Greffet, and Y. De Wilde, Phys. Rev. Lett. **110**, 146103 (2013).
[8] A. C. Jones and M. B. Raschke, Nano Lett. **12**, 1475 (2012).
[9] B. T. O'Callahan, W. E. Lewis, A. C. Jones, and M. B. Raschke, Phys. Rev. B **89**, 245446 (2014).
[10] R. S. DiMatteo, P. Greiff, S. L. Finberg, K. A. Young-Waithe, H. K. H. Choy, M. M. Masaki, and C. G. Fonstad, Appl. Phys. Lett. **79**, 1894 (2001).
[11] K. Park, S. Basu, W. P. King, and Z. M. Zhang, J. Quant. Spectrosc. Radiat. Transfer **109**, 305 (2008).
[12] M. Francoeur, R. Vaillon, and M. P. Mengüç, IEEE Trans. Energy Convers. **26**, 686 (2011).
[13] A. Kittel, W. Müller-Hirsch, J. Parisi, S.-A. Biehs, D. Reddig, and M. Holthaus, Phys. Rev. Lett. **95**, 224301 (2005).
[14] E. Rousseau, A. Siria, G. Jourdan, S. Volz, F. Comin, J. Chevrier, and J.-J. Greffet, Nature Photon. **3**, 514 (2009).
[15] S. Shen, A. Narayanaswamy, and G. Chen, Nano Lett. **9**, 2909 (2009).
[16] S. M. Rytov, Y. A. Kravtsov, and V. I. Tatarskii, *Principles of Statistical Radiophysics 3: Elements of Random Fields*, (Springer, New York, 1989).
[17] D. Polder and M. Van Hove, Phys. Rev. B **4**, 3303 (1971).

[18] K. Joulain, J.-P. Mulet, F. Marquier, R. Carminati, and J.-J. Greffet, Surf. Sci. Rep. **57**, 59 (2005).
[19] C. J. Fu and Z. M. Zhang, Int. J. Heat Mass Transfer **49**, 1703 (2006).
[20] J.-P. Mulet, K. Joulain, R. Carminati, and J-J. Greffet, Nanoscale Microscale Thermophys. Eng. **6**, 209 (2002).
[21] M. Francoeur, M. P. Mengüç, and R. Vaillon, J. Quant. Spectrosc. Radiat. Transfer **110**, 2002 (2009).
[22] R. Messina, M. Tschikin, S.-A. Biehs, and P. Ben-Abdallah, Phys. Rev. B **88**, 104307 (2013).
[23] A. Narayanaswamy and G. Chen, Phys. Rev. B **77**, 075125 (2008).
[24] K. Sasihithlu and A. Narayanaswamy, Opt. Express **19**, A772 (2011).
[25] K. Sasihithlu and A. Narayanaswamy, Phys. Rev. B **83**, 161406(R) (2011).
[26] M. Krüger, T. Emig, and M. Kardar, Phys. Rev. Lett. **106**, 210404 (2011).
[27] C. Otey and S. Fan, Phys. Rev. B **84**, 245431 (2011).
[28] B. Liu and S. Shen, Phys. Rev. B **87**, 115403 (2013).
[29] A. W. Rodriguez, O. Ilic, P. Bermel, I. Celanovic, J. D. Joannopoulos, M. Soljačić, and S. G. Johnson, Phys. Rev. Lett. **107**, 114302 (2011).
[30] A. Datas, D. Hirashima, and K. Hanamura, J. Therm. Sci. Technol. **8**, 91 (2013).
[31] A. Didari and M. P. Mengüç, J. Quant. Spectrosc. Radiat. Transfer **146**, 214 (2014).
[32] S.-B. Wen, J. Heat Transfer **132**, 072704 (2010).
[33] A. W. Rodriguez, M. T. Homer Reid, and S. G. Johnson, Phys. Rev. B **86**, 220302(R) (2012).
[34] A. P. McCauley, M. T. Homer Reid, M. Krüger, and S. G. Johnson, Phys. Rev. B **85**, 165104 (2012).
[35] S. Edalatpour and M. Francoeur, J. Quant. Spectrosc. Radiat. Transfer. **133**, 364 (2014).
[36] E. M. Purcell and C. R. Pennypacker, Astrophys. J. **186**, 705 (1973).
[37] B. T. Draine and P. J. Flatau, J. Opt. Soc. Am. A **11**, 1491 (1994).
[38] M. A. Yurkin and A. G. Hoekstra, J. Quant. Spectrosc. Radiat. Transfer **106**, 558 (2007).
[39] B. T. Draine, Astrophys. J. **333**, 848 (1988).
[40] I. Ayranci, R. Vaillon, and N. Selçuk, J. Quant. Spectrosc. Radiat. Transfer **103**, 83 (2007).
[41] M. A. Yurkin, D. De Kanter, and A. G. Hoekstra, J. Nanophotonics **4**, 041585 (2010).
[42] P. J. Flatau, K. A. Fuller, and D. W. Mackowski, Appl. Opt. **32**, 3302 (1993).
[43] Y.-L. Xu and B. A. S. Gustafson, Astrophys. J. **513**, 894 (1999).
[44] M. A. Yurkin, V. P. Maltsev, and A. G. Hoekstra, J. Opt. Soc. Am. A **23**, 2578 (2006).
[45] M. A. Yurkin, V. P. Maltsev, and A. G. Hoekstra, J. Opt. Soc. Am. A **23**, 2592 (2006).
[46] A. C. Andersen, H. Mutschke, T. Posch, M. Min, and A. Tamanai, J. Quant. Spectrosc. Radiat. Transfer **100**, 4 (2006).
[47] B. T. Draine and P. J. Flatau, arXiv:1305.6497.
[48] M. A. Yurkin and A. G. Hoekstra, J. Quant. Spectrosc. Radiat. Transfer **112**, 2234 (2011).
[49] N. B. Piller, Opt. Lett. **22**, 1674 (1997).
[50] N. B. Piller, Opt. Comm. **160**, 10 (1999).
[51] N. B. Piller and O. J. F. Martin, IEEE Trans. Ant. Propag. **46**, 1126 (1998).
[52] M. A. Yurkin, M. Min, and A. G. Hoekstra, Phys. Rev. E **82**, 036703 (2010).
[53] M. A. Yurkin and M. Kahnert, J. Quant. Spectrosc. Radiat. Transfer **123**, 176 (2013).
[54] E. Zubko, D. Petrov, Y. Grynko, Y. Shkuratov, H. Okamoto, K. Muinonen, T. Nousiainen, H. Kimura, T. Yamamoto, and G. Videen, Appl. Opt. **49**, 1267 (2010).
[55] P.-O. Chapuis, M. Laroche, S. Volz, and J.-J. Greffet, Appl. Phys. Lett. **92**, 201906 (2008).
[56] L. Novotny and B. Hecht, *Principles of Nano-Optics* (Cambridge University Press, New York, 2006).
[57] W. C. Chew, *Waves and Fields in Inhomogeneous Media* (IEEE Press, Piscataway, 1995).
[58] P. C. Chaumet, A. Sentenac, and A. Rahmani, Phys. Rev. E **70**, 036606 (2004).
[59] D. A. Smunev, P. C. Chaumet, and M. A. Yurkin, J. Quant. Spectrosc. Radiat. Transfer **156**, 67 (2015).
[60] D. J. Griffiths, *Introduction to Electrodynamics* (Prentice Hall, Upper Saddle River, 1999).
[61] R. Schmehl, MS Thesis, Arizona State University, 1994.
[62] R. D. Yates and D. J. Goodman, *Probability and Stochastic Processes* (Wiley, Hoboken, 2005), 2nd edition.
[63] A. Lakhtakia and G. W. Mulholland, J. Res. Natl. Inst. Stand. Technol. **98**, 699 (1993).
[64] C. E. Dungey and C. F. Bohren, J. Opt. Soc. Am. A **8**, 81 (1991).
[65] B. T. Draine and J. Goodman, Astrophys. J. **405**, 685 (1993).
[66] D. Gutkowicz-Krusin and B. T. Draine, arXiv:astro-ph/0403082.
[67] A. Rahmani, P. C. Chaumet, and G. W. Bryant, Opt. Lett. **27**, 2118 (2002).
[68] A. Rahmani, P. C. Chaumet, and G. W. Bryant, Astrophys. J. **607**, 873 (2004).
[69] M. J. Collinge and B. T. Draine, J. Opt. Soc. Am. A **21**, 2023 (2004).
[70] P. C. Chaumet, A. Rahmani, F. de Fornel, and J.-P. Dufour, Phys. Rev. B **58**, 2310 (1998).

CHAPTER 5

NEAR-FIELD RADIATIVE HEAT TRANSFER BETWEEN ARBITRARILY-SHAPED OBJECTS AND A SURFACE*

5.1 Abstract

A fluctuational electrodynamics-based formalism for calculating near-field radiative heat transfer between objects of arbitrary size and shape and an infinite surface is presented. The surface interactions are treated analytically via Sommerfeld's theory of electric dipole radiation above an infinite plane. The volume integral equation for the electric field is discretized using the thermal discrete dipole approximation (T-DDA). The framework is verified against exact results in the sphere-surface configuration, and is applied to analyze near-field radiative heat transfer between a complex-shaped probe and an infinite plane both made of silica. It is found that when the probe tip size is approximately equal to or smaller than the gap d separating the probe and the surface, coupled localized surface phonon (LSPh)-surface phonon-polariton (SPhP) mediated heat transfer occurs. In this regime, the net spectral heat rate exhibits four resonant modes due to LSPhs along the minor axis of the probe while the net total heat rate in the near fieldfollows a $d^{-0.3}$ power law. Conversely, when the probe tip size is much larger than

* The following sections have been submitted to be published in *Physical Review B* as a paper. As such, it is to be treated as a stand-alone paper with its own references, sections, and equations. Coauthors of this paper are Sheila Edalatpour and Mathieu Francoeur.

the separation gap d, heat transfer is mediated by SPhPs resulting in two resonant modes in the net spectral heat rate corresponding to those of a single emitting silica surface while the net total heat rate follows a d^{-2} power law. It is also demonstrated that a complex-shaped probe can be approximated by a prolate spheroidal electric dipole when the thermal wavelength is larger than the major axis of the spheroidal dipole and when the separation gap d is much larger than the radius of curvature of the dipole tip facing the surface.

5.2 Introduction

Near-field radiative heat transfer between arbitrarily-shaped objects and a surface is of importance in many engineering applications such as near-field thermal spectroscopy and imaging [1-4], tip-based nanomanufacturing [5-7] and localized radiative cooling [8]. An analytical solution for this type of problem only exists for the case of a single sphere above an infinite plane [9,10]. Simplified formulations, namely the proximity and electric dipole approximations, have been used to model experiments involving a micro/nanosized object and a large surface exchanging thermal radiation [1,3,4,11-14]. The proximity approximation is valid when the object size is much larger than its distance relative to the surface and when the object is optically thick [15,16]. When these conditions are satisfied, the heat rate between the object and the surface can be modeled as a summation of local heat rates between two parallel planes [13]. The electric dipole approximation is valid when the size of the object is much smaller than the thermal wavelength and its distance relative to the surface. Various electric dipole formulations have been proposed for modeling near-field thermal interactions between a small object

and a surface. These formulations include a spherical dipole above a flat [17] and a structured surface [18], a spherical dipole with dressed polarizability above a flat surface [14], and a spheroidal dipole above a flat surface [19]. These simplified models are however valid under limiting conditions that are often not satisfied in actual experiments. Accurate modeling of near-field radiative heat transfer between arbitrarily-shaped objects and a surface that does not rely on simplified formulations and fitting parameters can be done via numerical methods [16,20-24]. Yet, numerical methods are difficult to apply to this multiscale problem due to the prohibitive calculation time associated with discretizing a surface that is many orders of magnitude larger than the micro/nanosized objects. The only numerical formulation capable of handling nontrivial geometries and an infinite surface is a combination of a scattering-based approach and the boundary element method [25].

In this paper, a framework for modeling near-field radiative heat transfer between objects and an infinite surface is provided. The formalism, based on fluctuational electrodynamics [26], is independent of the size, shape and number of objects. The volume integral equation for the electric field derived from fluctuational electrodynamics is discretized using the thermal discrete dipole approximation (T-DDA) [16,23,27]. The interactions between the objects and the surface are treated analytically using Sommerfeld's theory of electric dipole radiation above an infinite plane [28]. This approach, also used in the discrete dipole approximation literature for predicting light scattering by particles on or near a surface [29-36], does not necessitate discretization of the surface. The T-DDA with surface interaction is afterwards applied to study near-field radiative heat transfer between a probe and a surface. Understanding the thermal

interactions in the probe-surface configuration is of interest in near-field thermal spectroscopy where two independent experimental studies reported resonance redshift of the scattered thermal near field [3,4]. McCauley et al. [25] analyzed the total heat rate between a conically-shaped probe and a surface as well as the spatial distribution of power absorbed within the surface. Kim et al. [37] investigated the validity of fluctuational electrodynamics in the extreme near field by measuring the heat rate between a dull probe and a surface. The probing tip was modeled as a hemisphere for which the heat rate could also be obtained via the proximity approximation. In this work, the spectral and total heat rate between a probe with a tip size smaller than, approximately equal to, and larger than the separation gap is studied for the first time. The validity of the spheroidal electric dipole approximation for predicting near-field radiative heat transfer between a probe and a surface is also discussed.

The paper is organized as follows. The framework for calculating near-field radiative heat transfer between arbitrarily-shaped objects and a surface is presented in Section 5.3. In Section 5.4, the T-DDA with surface interaction is applied to the analysis of near-field radiative heat transfer between a probe and a surface. Concluding remarks are then provided.

5.3 Description of the Framework

5.3.1 Volume integral equation for the electric field

The formalism described hereafter is based on fluctuational electrodynamics, and is thus valid for heat sources in local thermodynamic equilibrium. The problem under consideration is shown in Fig. 5.1, where radiative heat transfer between objects

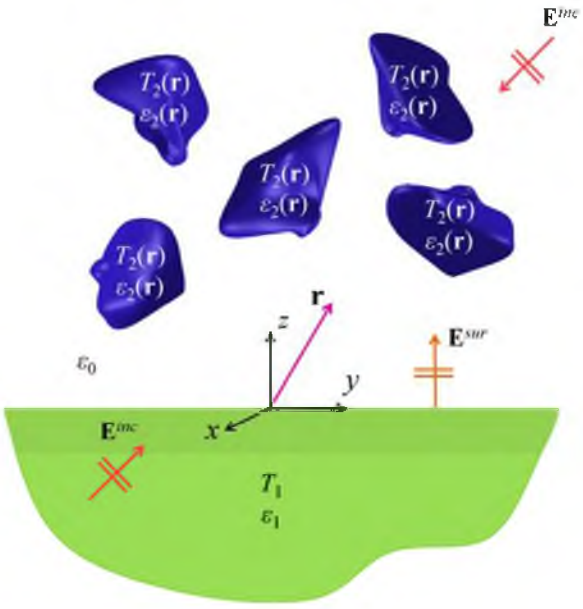

Figure 5.1 Schematic representation of the problem under consideration. Objects (medium 2) are submerged in vacuum (medium 0) above an infinite surface (medium 1). The incident electric field $\mathbf{E}^{inc}$ accounts for illumination by external sources, while the surface field $\mathbf{E}^{sur}$ is the electric field due to thermal emission by the surface.

submerged in vacuum and an infinite surface is to be calculated. The vacuum, the surface and the objects are referred to as medium 0, 1 and 2, respectively. It is assumed that the objects of arbitrary number, shape and size occupy a total volume V_2 and are isotropic, linear and nonmagnetic. Individual objects may have different, inhomogeneous temperatures T_2 and frequency-dependent dielectric functions ε_2 local in space. The surface, of volume V_1 and uniform temperature T_1, is assumed to be isotropic, linear, nonmagnetic and is characterized by a homogeneous dielectric function ε_1 local in space. Illumination by external sources such as laser irradiation or thermal emission by the surroundings (i.e., the thermal bath) is modeled via an incident electric field $\mathbf{E}^{inc}$. The incident electric field can originate from above or below the surface. The electric field thermally emitted by the surface into the vacuum of volume V_0 is denoted by $\mathbf{E}^{sur}$.

The net radiative heat rate between the objects and the surface is derived from the

stochastic Maxwell equations, where a fluctuating current $\mathbf{J}^{fl}$ representing thermal emission is added to Ampère's law [26]. The ensemble average of the fluctuating current is zero, while the ensemble average of the spatial correlation function of the fluctuating current is related to the local temperature of a heat source via the fluctuation-dissipation theorem [26]:

$$\left\langle \mathbf{J}^{fl}\left(\mathbf{r}',\omega\right)\otimes\mathbf{J}^{fl}\left(\mathbf{r}'',\omega'\right)\right\rangle = \frac{4\omega\varepsilon_0\varepsilon''}{\pi}\Theta\left(\omega,T\right)\delta\left(\mathbf{r}'-\mathbf{r}''\right)\delta\left(\omega-\omega'\right)\overline{\overline{\mathbf{I}}} \tag{5.1}$$

where $\otimes$ denotes the outer product, $\overline{\overline{\mathbf{I}}}$ is the unit dyadic, ε_0 is the electric permittivity of vacuum, ε'' is the imaginary part of the dielectric function of the heat source and $\Theta(\omega,T)$ is the mean energy of an electromagnetic state given by $\Theta(\omega,T)=\hbar\omega/[\exp(\hbar\omega/k_BT)-1]$.

The electric field everywhere above the surface satisfies the following vector wave equation derived from the stochastic Maxwell equations [16,27]:

$$\nabla\times\nabla\times\mathbf{E}(\mathbf{r},\omega)-k_0^2\mathbf{E}(\mathbf{r},\omega)=i\omega\mu_0\mathbf{J}(\mathbf{r},\omega),\quad \mathbf{r}\in V_0\cup V_2 \tag{5.2}$$

where k_0 and μ_0 are the magnitude of the wavevector and the magnetic permeability of vacuum, respectively, i is the complex constant and $\mathbf{r}$ is the position vector where the fields are observed in $V_0\cup V_2$. The current $\mathbf{J}$ in Eq. (5.2) is an equivalent source function generating fluctuating and scattered electric fields:

$$\mathbf{J}(\mathbf{r},\omega)=\mathbf{J}_2^{fl}(\mathbf{r},\omega)-i\omega\varepsilon_0\left(\varepsilon_2(\mathbf{r})-1\right)\mathbf{E}(\mathbf{r},\omega),\quad \mathbf{r}\in V_2 \tag{5.3}$$

where the subscript 2 in $\mathbf{J}_2^{fl}$ specifies that the fluctuating current is in V_2. Note that the current $\mathbf{J}$ vanishes in V_0.

The solution of the inhomogeneous linear differential equation (5.2) is the sum of the solution of the homogeneous equation and a particular solution of the inhomogeneous

equation. The homogeneous vector wave equation is given by:

$$\nabla\times\nabla\times\left(\mathbf{E}^{inc}(\mathbf{r},\omega)+\mathbf{E}^{sur}(\mathbf{r},\omega)\right)-k_0^2\left(\mathbf{E}^{inc}(\mathbf{r},\omega)+\mathbf{E}^{sur}(\mathbf{r},\omega)\right)=\mathbf{0},\quad \mathbf{r}\in V_0\cup V_2 \tag{5.4}$$

The solution of Eq. (5.4) provides the electric field that would exist above the surface in the absence of objects. This electric field is comprised of two components, namely the incident field $\mathbf{E}^{inc}$ and the surface field $\mathbf{E}^{sur}$. The surface field is generated by fluctuating currents in V_1, $\mathbf{J}_1^{fl}$, and its expression is given by:

$$\mathbf{E}^{sur}(\mathbf{r},\omega)=i\omega\mu_0\int_{V_1}\overline{\overline{\mathbf{G}}}^{T}(\mathbf{r},\mathbf{r}',\omega)\cdot\mathbf{J}_1^{fl}(\mathbf{r}',\omega)d^3\mathbf{r}',\quad \mathbf{r}\in V_0\cup V_2 \tag{5.5}$$

where $\overline{\overline{\mathbf{G}}}^{T}$ is the transmission dyadic Green's function (DGF) relating the field observed at $\mathbf{r}$ in $V_0\cup V_2$ to a source point $\mathbf{r}'$ located in V_1 [38,39]. The expression for the incident field must satisfy Eq. (5.4) and depends on the external radiation source.

The particular solution of Eq. (5.2) is the sum of the fluctuating and scattered electric fields generated by the current $\mathbf{J}$. The fluctuating and scattered fields are obtained using DGFs relating the electric field observed at $\mathbf{r}$ to a source located at $\mathbf{r}'$, as shown in Fig. 5.2, when both $\mathbf{r}$ and $\mathbf{r}'$ are located above the surface in $V_0\cup V_2$:

$$\mathbf{E}^{sca}(\mathbf{r},\omega)+\mathbf{E}^{fl}(\mathbf{r},\omega)=i\omega\mu_0\int_{V_2}\overline{\overline{\mathbf{G}}}(\mathbf{r},\mathbf{r}',\omega)\cdot\mathbf{J}(\mathbf{r}',\omega)d^3\mathbf{r}',\quad \mathbf{r}\in V_0\cup V_2 \tag{5.6}$$

The DGF $\overline{\overline{\mathbf{G}}}$ is comprised of two components. The first component is the free space DGF, $\overline{\overline{\mathbf{G}}}^{0}$, that accounts for the electric field generated at $\mathbf{r}$ due to direct radiation by the source $\mathbf{J}$ located at $\mathbf{r}'$ in the absence of the surface. The second component is the reflection DGF, $\overline{\overline{\mathbf{G}}}^{R}$, representing the electric field generated at $\mathbf{r}$ due to radiation by the

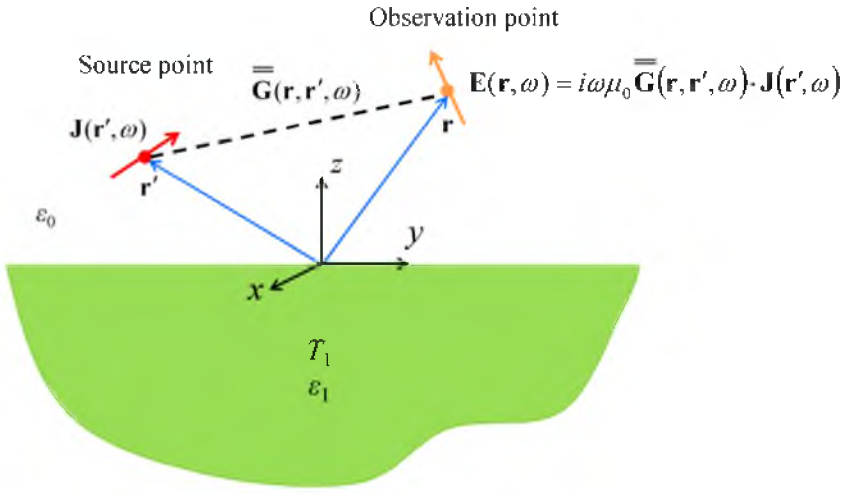

Figure 5.2 Dyadic Green's function (DGF) relating the electric field at point **r** to a source located at point $\mathbf{r}'$ in the presence of a surface.

source **J** located at $\mathbf{r}'$ after reflection by the surface.

The volume integral equation for the total electric field in $V_0 \cup V_2$ is obtained by adding the incident and surface fields to Eq. (5.6):

$$\mathbf{E}(\mathbf{r},\omega)=i\omega\mu_0\int_{V_2}\left(\overline{\overline{\mathbf{G}}}^{0}(\mathbf{r},\mathbf{r}',\omega)+\overline{\overline{\mathbf{G}}}^{R}(\mathbf{r},\mathbf{r}',\omega)\right)\cdot\mathbf{J}(\mathbf{r}',\omega)d^3\mathbf{r}' + \mathbf{E}^{inc}(\mathbf{r},\omega)+\mathbf{E}^{sur}(\mathbf{r},\omega), \qquad \mathbf{r}\in V_0\cup V_2 \tag{5.7}$$

The magnetic field in $V_0 \cup V_2$ can be obtained from Eq. (5.7) using Faraday's law.

The solution of Eq. (5.7) provides the electric field in V_2 from which heat transfer is calculated. An analytical solution of Eq. (5.7) only exists for a single sphere above an infinite surface [9,10]. For arbitrarily-shaped objects, numerical approaches should be considered. Here, the T-DDA [16,23,27], which is a numerically exact method, is used for solving Eq. (5.7) and thus for computing radiation heat transfer.

5.3.2 Radiative heat transfer calculations with the thermal discrete dipole approximation (T-DDA)

The T-DDA formulation is initiated by discretizing V_2 into N cubical subvolumes. The size of the subvolumes must be smaller than all characteristic lengths of the problem, namely the wavelength in V_2 as well as the object-object and object-surface separation distances. In addition, the subvolume size must be small enough to represent accurately the object shape via a cubical lattice. When these conditions are fulfilled, the electric field, the DGFs and the electromagnetic properties can be assumed uniform inside a given subvolume. Under the approximation of uniform electric field, it is possible to conceptualize the subvolumes as electric point dipoles. The total dipole moment associated with a subvolume i of volume ΔV_i is related to the equivalent current via $\mathbf{p}_i = (i/\omega)\int_{\Delta V_i} \mathbf{J}(\mathbf{r}',\omega)d^3\mathbf{r}'$. The discretized volume integral equation for the electric field (5.7) can thus written in terms of dipole moments as follows:

$$\frac{1}{\alpha_i}\mathbf{p}_i - \frac{k_0^2}{\varepsilon_0}\sum_{j\neq i}\overline{\overline{\mathbf{G}}}_{ij}^{0}\cdot\mathbf{p}_j - \frac{k_0^2}{\varepsilon_0}\sum_{j}\overline{\overline{\mathbf{G}}}_{ij}^{R}\cdot\mathbf{p}_j = \frac{3}{(\varepsilon_{2,i}+2)}\frac{1}{\alpha_i^{CM}}\mathbf{p}_i^{fl} + \mathbf{E}_i^{inc} + \mathbf{E}_i^{sur} \tag{5.8}$$

where the DGFs $\overline{\overline{\mathbf{G}}}_{ij}^{0}$ and $\overline{\overline{\mathbf{G}}}_{ij}^{R}$ are evaluated between the center points of subvolumes i and j. The total dipole moment $\mathbf{p}_i$ is the sum of two contributions, namely an induced dipole moment $\mathbf{p}_i^{ind} = \Delta V_i \varepsilon_0 (\varepsilon_{2,i} - 1)\mathbf{E}_i$ and a thermally fluctuating dipole moment $\mathbf{p}_i^{fl} = (i/\omega)\int_{\Delta V_i} \mathbf{J}_2^{fl}(\mathbf{r}',\omega)d^3\mathbf{r}'$. Using this last expression in combination with the fluctuation-dissipation theorem (1), the ensemble average of the spatial correlation function of fluctuating dipole moments can be expressed in terms of the local temperature of the medium [16]. The terms α_i^{CM} and α_i are the Clausius-Mossotti and radiative

polarizabilities given by:

$$\alpha_i^{CM} = 3\varepsilon_0 \Delta V_i \frac{\varepsilon_{2,i} - 1}{\varepsilon_{2,i} + 2} \tag{5.9}$$

$$\alpha_i = \frac{\alpha_i^{CM}}{1 - (\alpha_i^{CM} / 2\pi\varepsilon_0 a_i^3)[e^{ik_0 a_i}(1 - ik_0 a_i) - 1]} \tag{5.10}$$

where a_i is the radius of a sphere of volume ΔV_i. The application of Eq. (5.8) to all N subvolumes in V_2 results in a system of equations that can be written in a matrix form:

$$\left(\overline{\overline{\mathbf{A}}} + \overline{\overline{\mathbf{R}}}\right) \cdot \overline{\mathbf{P}} = \overline{\mathbf{E}}^{fdt} + \overline{\mathbf{E}}^{inc} + \overline{\mathbf{E}}^{sur} \tag{5.11}$$

where $\overline{\mathbf{E}}^{fdt}$ and $\overline{\mathbf{E}}^{sur}$ are $3N$ stochastic column vectors containing the first term on the right-hand side of Eq. (5.8) and the surface field, respectively, while $\overline{\mathbf{E}}^{inc}$ is the $3N$ deterministic column vector containing the incident field. The term $\overline{\mathbf{P}}$ is the $3N$ stochastic column vector containing the unknown total dipole moments of the subvolumes. The matrix $\overline{\overline{\mathbf{A}}}$ is the $3N$ by $3N$ deterministic interaction matrix which is composed of submatrices $\overline{\overline{\mathbf{A}}}_{ij}$ representing the direct interaction between subvolumes i and j in the absence of the surface. A submatrix $\overline{\overline{\mathbf{A}}}_{ij}$, obtained from the free space DGF, is calculated using the following expressions when $i \neq j$:

$$\overline{\overline{\mathbf{A}}}_{ij} = C_{ij} \begin{bmatrix} \beta_{ij} + \gamma_{ij}\hat{r}_{ij,x}^2 & \gamma_{ij}\hat{r}_{ij,x}\hat{r}_{ij,y} & \gamma_{ij}\hat{r}_{ij,x}\hat{r}_{ij,z} \\ \gamma_{ij}\hat{r}_{ij,y}\hat{r}_{ij,x} & \beta_{ij} + \gamma_{ij}\hat{r}_{ij,y}^2 & \gamma_{ij}\hat{r}_{ij,y}\hat{r}_{ij,z} \\ \gamma_{ij}\hat{r}_{ij,z}\hat{r}_{ij,x} & \gamma_{ij}\hat{r}_{ij,z}\hat{r}_{ij,y} & \beta_{ij} + \gamma_{ij}\hat{r}_{ij,z}^2 \end{bmatrix} \tag{5.12}$$

where

$$\hat{r}_{ij,\alpha} = \frac{r_{ij,\alpha}}{r_{ij}} \ (\alpha = x, y, z) \tag{5.13}$$

$$C_{ij} = -\frac{k_0^2}{4\pi\varepsilon_0}\frac{e^{ik_0 r_{ij}}}{r_{ij}} \tag{5.14}$$

$$\beta_{ij} = \left[1 - \frac{1}{(k_0 r_{ij})^2} + \frac{i}{k_0 r_{ij}}\right] \tag{5.15}$$

$$\gamma_{ij} = -\left[1 - \frac{3}{(k_0 r_{ij})^2} + \frac{3i}{k_0 r_{ij}}\right] \tag{5.16}$$

In Eqs. (13) to (16), r_{ij} is the magnitude of the distance vector between subvolumes i and j. When $i = j$, the submatrix $\overline{\overline{\mathbf{A}}}_{ii}$ represents the self-interaction of subvolume i in the absence of surface and its expression is given by $(1/\alpha_i)\overline{\overline{\mathbf{I}}}$.

The term $\overline{\overline{\mathbf{R}}}$ in Eq. (5.11) is the $3N$ by $3N$ deterministic reflection-interaction matrix that contains submatrices $\overline{\overline{\mathbf{R}}}_{ij}$ representing the interaction between subvolumes i and j due to reflection by the surface. A submatrix $\overline{\overline{\mathbf{R}}}_{ij}$ is obtained from the reflection DGF [31,40]:

$$\begin{aligned}\overline{\overline{\mathbf{R}}}_{ij} = {} & C_{I,ij}\frac{\varepsilon_1 - 1}{\varepsilon_1 + 1}\begin{bmatrix} -(\beta_{I,ij} + \gamma_{I,ij}\hat{r}_{I,ij,x}^2) & -\gamma_{I,ij}\hat{r}_{I,ij,x}\hat{r}_{I,ij,y} & \gamma_{I,ij}\hat{r}_{I,ij,x}\hat{r}_{I,ij,z} \\ -\gamma_{I,ij}\hat{r}_{I,ij,x}\hat{r}_{I,ij,y} & -(\beta_{I,ij} + \gamma_{I,ij}\hat{r}_{I,ij,y}^2) & \gamma_{I,ij}\hat{r}_{I,ij,y}\hat{r}_{I,ij,z} \\ -\gamma_{I,ij}\hat{r}_{I,ij,x}\hat{r}_{I,ij,z} & -\gamma_{I,ij}\hat{r}_{I,ij,y}\hat{r}_{I,ij,z} & (\beta_{I,ij} + \gamma_{I,ij}\hat{r}_{I,ij,z}^2) \end{bmatrix} \\ & -\frac{1}{4\pi\varepsilon_0}\begin{bmatrix} \hat{\rho}_{ij,x}^2 I_\rho^H - \hat{\rho}_{ij,y}^2 I_\varphi^H & \hat{\rho}_{ij,x}\hat{\rho}_{ij,y}(I_\rho^H + I_\varphi^H) & \hat{\rho}_{ij,x} I_\rho^V \\ \hat{\rho}_{ij,x}\hat{\rho}_{ij,y}(I_\rho^H + I_\varphi^H) & \hat{\rho}_{ij,y}^2 I_\rho^H - \hat{\rho}_{ij,x}^2 I_\varphi^H & \hat{\rho}_{ij,y} I_\rho^V \\ -\hat{\rho}_{ij,x} I_\rho^V & -\hat{\rho}_{ij,y} I_\rho^V & I_z^V \end{bmatrix}\end{aligned} \tag{5.17}$$

where the subscripts x, y, and z indicate vector components in Cartesian coordinates, while the subscripts ρ, φ, and z refer to vector components in cylindrical coordinates. The parameters $\hat{r}_{I,ij,\alpha}$, $C_{I,ij}$, $\beta_{I,ij}$, and $\gamma_{I,ij}$ are defined in the same manner as in Eqs. (13) to (16), except that r_{ij} is replaced by $r_{I,ij}$, which is defined as the distance between

subvolume i and the image of subvolume j within the surface. In Eq. (5.17), $\hat{\rho}_{ij,\alpha} = \dfrac{\rho_{ij,\alpha}}{|\boldsymbol{\rho}_{ij}|}$ ($\alpha = x, y$), where $\boldsymbol{\rho}_{ij}$ is the distance vector between subvolumes i and j along the surface ($\boldsymbol{\rho}_{ij} = (x_i - x_j)\hat{\mathbf{x}} + (y_i - y_j)\hat{\mathbf{y}}$). The terms I_ρ^V, I_z^V, I_ρ^H, and I_φ^H are defined as:

$$I_\rho^V = \frac{\partial^2}{\partial\rho\partial z} k_1^2 V'_{00} \tag{5.18}$$

$$I_z^V = \left(\frac{\partial^2}{\partial z^2} + k_0^2 \right) k_1^2 V'_{00} \tag{5.19}$$

$$I_\rho^H = \frac{\partial^2}{\partial\rho^2} k_0^2 V'_{00} + k_0^2 U'_{00} \tag{5.20}$$

$$I_\varphi^H = -\frac{1}{\rho_{ij}} \frac{\partial}{\partial\rho} k_0^2 V'_{00} - k_0^2 U'_{00} \tag{5.21}$$

where k_1 is the magnitude of the wavevector in V_1, while V'_{00} and U'_{00} are the Sommerfeld integrals given by:

$$V'_{00} = 2i \int_0^\infty \left[\frac{1}{k_1^2 k_{z0} + k_0^2 k_{z1}} - \frac{1}{k_{z0}(k_1^2 + k_0^2)} \right] e^{ik_{z0}(z_i + z_j)} J_0(k_\rho \rho_{ij}) k_\rho dk_\rho \tag{5.22}$$

$$U'_{00} = 2i \int_0^\infty \left[\frac{1}{k_{z0} + k_{z1}} - \frac{k_0^2}{k_{z0}(k_1^2 + k_0^2)} \right] e^{ik_{z0}(z_i + z_j)} J_0(k_\rho \rho_{ij}) k_\rho dk_\rho \tag{5.23}$$

In Eqs. (22) and (23), J_0 is the zeroth-order Bessel function of the first kind, while k_ρ and k_{zj} are the wavevector components parallel and perpendicular to the surface, respectively. Note that the parallel component of the wavevector is a complex number, such that the Sommerfeld integrals are evaluated in the complex plane [40]. The z-components of the position vectors (i.e., z_i and z_j) are calculated relative to the surface. Evaluation of the Sommerfeld integrals involves complex integration of multivalued functions k_{zj} (= (

$k_j^2 - k_\rho^2)^{1/2}$). Multivalued functions are represented in the complex plane via Riemann surfaces [41]. In order to perform the integration of a multivalued function, it is necessary to perform branch cuts such that the problem reduces to the integration of a single valued function on a single branch of the Riemann surface. Once branch cuts are performed, it is necessary to define the path of the integration. The integration path should avoid the poles of the function to be integrated and should not cross branch cuts in order to stay on a single branch of the Riemann surface. The integration path is not unique and is selected to ensure a fast convergence of the function to be integrated. In this work, the techniques and FORTRAN subroutines developed by Lager and Lytle [42,43] are used for calculating the Sommerfeld integrals.

The submatrix $\overline{\overline{\mathbf{R}}}_{ij}$ given by Eq. (5.17) represents the electric field intercepted by subvolume *i* due to emission by subvolume *j* after reflection at the surface. Mathematically, spherical waves emitted by subvolume *j* are expressed using Eqs. (22) and (23) as the product of cylindrical waves propagating parallel to the surface (Bessel function) and plane waves propagating along the *z*-direction (exponential term). Only the plane wave component interacts with the surface. In the static limit or when the surface is a perfect electric conductor, $\overline{\overline{\mathbf{R}}}_{ij}$ can be obtained from the image theory using the direct interaction between subvolume *i* and the image of subvolume *j*, with dipole moment $\frac{\varepsilon_1 - 1}{\varepsilon_1 + 1}\left(-p_{jx}\hat{\mathbf{x}} - p_{jy}\hat{\mathbf{y}} + p_{jz}\hat{\mathbf{z}}\right)$, within the surface [44]. The image contribution corresponds to the first term on the right-hand side of Eq. (5.17). In this paper, the general case where $\overline{\overline{\mathbf{R}}}_{ij}$ is calculated from Eq. (5.17) is considered.

The net spectral heat rate between the surface and the objects is defined as $\langle Q_{net,\omega} \rangle = \sum_i \langle Q_{abs,\omega,1i} \rangle - \sum_i \langle Q_{abs,\omega,i1} \rangle$, where $\langle Q_{abs,\omega,1i} \rangle$ is the spectral power absorbed by subvolume i due to thermal emission by the surface and vice-versa for $\langle Q_{abs,\omega,i1} \rangle$, while $\langle\ \rangle$ denotes a time average. Using reciprocity, the net spectral heat rate can be expressed solely in terms of $\langle Q_{abs,\omega,1i} \rangle$:

$$\langle Q_{net,\omega} \rangle = \sum_i \langle Q_{abs,\omega,1i} \rangle \left[\frac{\Theta(\omega, T_{2i})}{\Theta(\omega, T_1)} - 1 \right] \tag{5.24}$$

where T_{2i} is the temperature of subvolume i. The power absorbed $\langle Q_{abs,\omega,1i} \rangle$ is calculated from the induced dipole moments as follows:

$$\langle Q_{abs,\omega,1i} \rangle = \frac{\omega}{2} \left(\mathrm{Im}[(\alpha_i^{-1})^*] - \frac{2}{3} k_0^3 \right) \mathrm{tr} \langle \mathbf{p}_i^{ind} \otimes \mathbf{p}_i^{ind} \rangle \tag{5.25}$$

where ergodicity is assumed [45]. Note that when calculating the power absorbed, it is assumed that the objects described by V_2 are nonemitting and purely absorbing (T_{2i} = 0 K). Yet, thermal emission by V_2 is accounted for by capitalizing on reciprocity, as shown by Eq. (5.24). Therefore, $\mathbf{p}_i^{fl} = \mathbf{0}$ and $\mathbf{p}_i = \mathbf{p}_i^{ind}$ for all subvolumes contained in V_2. The trace of the autocorrelation function of the induced dipole moments in Eq. (5.25) is obtained directly from the system of equations (5.11):

$$\langle \bar{\mathbf{P}} \otimes \bar{\mathbf{P}} \rangle = (\bar{\bar{\mathbf{A}}} + \bar{\bar{\mathbf{R}}})^{-1} \cdot \langle (\bar{\mathbf{E}}^{inc} \otimes \bar{\mathbf{E}}^{inc}) + (\bar{\mathbf{E}}^{sur} \otimes \bar{\mathbf{E}}^{sur}) \rangle \cdot \left((\bar{\bar{\mathbf{A}}} + \bar{\bar{\mathbf{R}}})^{-1} \right)^{\dagger} \tag{5.26}$$

where the superscript † indicates the Hermitian operator defined as the conjugate transpose. The ensemble average of the spatial correlation function of the surface fields in subvolumes i and j is calculated as [46]:

$$\left\langle \mathbf{E}_i^{sur} \otimes \mathbf{E}_j^{sur} \right\rangle = \frac{\varepsilon_0 \mu_0^2 \omega^3 \varepsilon_1''}{8\pi^3} \Theta(\omega, T_1) \times \int_0^{\infty} \int_0^{2\pi} \frac{k_\rho}{|k_{z1}|^2 k_{z1}''} e^{i(k_{z0} z_i - k_{z0}^* z_j)} e^{i\mathbf{k}_\rho \cdot \boldsymbol{\rho}_{ij}} \left[\left| t_{12}^s \right|^2 (\hat{\mathbf{s}} \cdot \hat{\mathbf{s}})(\hat{\mathbf{s}} \otimes \hat{\mathbf{s}}) + \left| t_{12}^p \right|^2 (\hat{\mathbf{p}}_1 \cdot \hat{\mathbf{p}}_1^*)(\hat{\mathbf{p}}_0 \otimes \hat{\mathbf{p}}_0^*) \right] d\varphi dk_\rho \tag{5.27}$$

where k_{z1}'' is the imaginary part of k_{z1}, t_{12}^s and t_{12}^p are the Fresnel transmission coefficients for transverse electric (TE) and transverse magnetic (TM) polarizations, and the azimuthal angle φ is measured between the parallel component of the wavevector and the x-axis. The terms $\hat{\mathbf{s}}$ and $\hat{\mathbf{p}}$ are unit vectors oriented along the TE and TM polarizations, respectively [38]. In Eq. (5.27), the parallel component of the wavevector k_ρ is a real number since the electric field does not vary along the x- and y-directions for an emitting infinite surface.

Once the dipole moment correlation matrix is computed with Eq. (5.26), the power absorbed in subvolume i, $\left\langle Q_{abs,\omega,i} \right\rangle$, and the net heat rate between the objects and the surface, $\left\langle Q_{net,\omega} \right\rangle$, are respectively calculated with Eqs. (25) and (24). The T-DDA with surface interaction is used next to analyze near-field radiative heat transfer between a complex-shaped probe and a surface.

5.4 Near-field radiative heat transfer between a probe and a surface

The framework described in Section 5.3 has been verified in the sphere-surface configuration using the analytical solution of Otey and Fan [10]. An excellent agreement between the T-DDA and exact results has been found (see Section 5.6.1), such that the framework is used hereafter to analyze radiative heat transfer between a probe and a surface. The probe geometry consists of an assembly of a rectangular cuboid, a conical

frustum and a cylinder (see Fig. 5.3). The base and the height of the cuboid have dimensions of 57.8 nm and 288.9 nm, respectively. The conical frustum has a height of 3.872 μm, and the diameters of its lower and upper bases are 115.6 nm and 1.16 μm, respectively. The cylinder has a height of 809.0 nm and a diameter of 1.16 μm. The probe and the surface are both made of silica. The dielectric function of silica has been taken from Ref. [47]. In all cases, the surface is at a temperature T_1 = 300 K while the probe is at T_2 = 400 K. For simplicity, it is assumed that there is no incident electric field. For far-field simulations (d = 100 μm), 11113 uniform subvolumes were used to discretize the probe while 13111 nonuniform subvolumes were employed for near-field simulations (d = 10 nm). Increasing the number of subvolumes beyond these values did not affect the results.

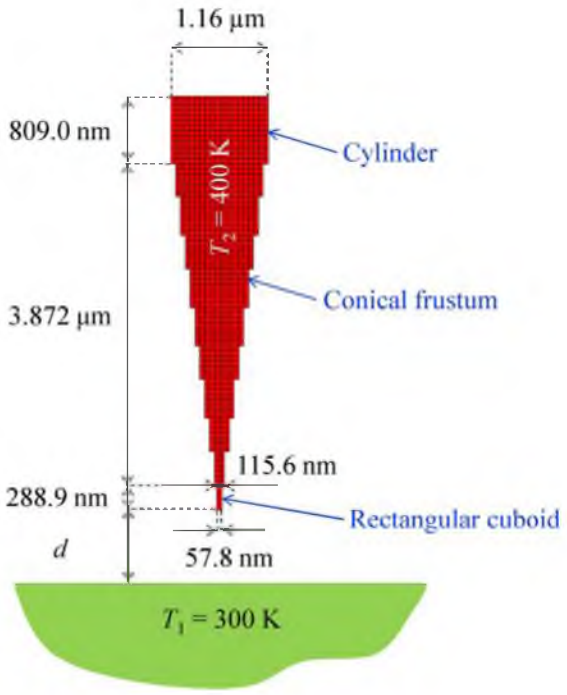

Figure 5.3 Radiative heat transfer between a probe and a surface separated by a gap of thickness d. The probe is modeled as an assembly of a rectangular cuboid, a conical frustum and a cylinder.

5.4.1 Spectral distribution of heat rate and near-field regimes

Figure 5.4(a) shows the net spectral heat rate for separation gaps d between the probe and the surface of 10 nm, 100 nm and 100 μm. For purpose of comparison, the net spectral heat rate for a sphere of same material, volume (diameter of 1.6 μm) and temperature as the probe is reported in Fig. 5.4(b). The heat rate profiles exhibit low-frequency (~ 0.06 eV) and high-frequency (~ 0.14 eV) resonances due to surface phonon-polaritons (SPhPs) and localized surface phonons (LSPhs). At separation gaps of 100 nm and 100 μm, both the low- and high-frequency resonances of the probe-surface heat rate are split into two modes, while this splitting is not observed for a 10-nm-thick gap as well as in the sphere-surface configuration. The origin of these resonances can be explained by first considering the near-field thermal spectrum of the surface in the absence of object, characterized by the energy density, as shown in Section 5.6.2 for distances of 10 nm, 100 nm and 100 μm. In the near field (10 nm and 100 nm), low- and high-frequency resonances are observed at 0.0613 eV and 0.1435 eV due to thermal excitation of SPhPs. When losses are small ($\varepsilon_1'' \to 0$), SPhPs are resonantly excited at a flat material-vacuum interface when the real part of the dielectric function ε_1' equals -1 [39]. Here, the high-frequency resonance occurs when $\varepsilon_1' = -1$, while the low-frequency SPhP mode arises when ε_1' is equal to -0.83 due to nonnegligible losses. In the far field (100 μm), SPhPs lead to low thermal emission resulting in local minima in the energy density profile. Yet, when an object is located at a distance of 100 μm above the surface, low- and high-frequency resonances arise due to LSPhs supported by the sphere and the probe. The electric dipole approximation can be used for estimating these LSPh modes. The

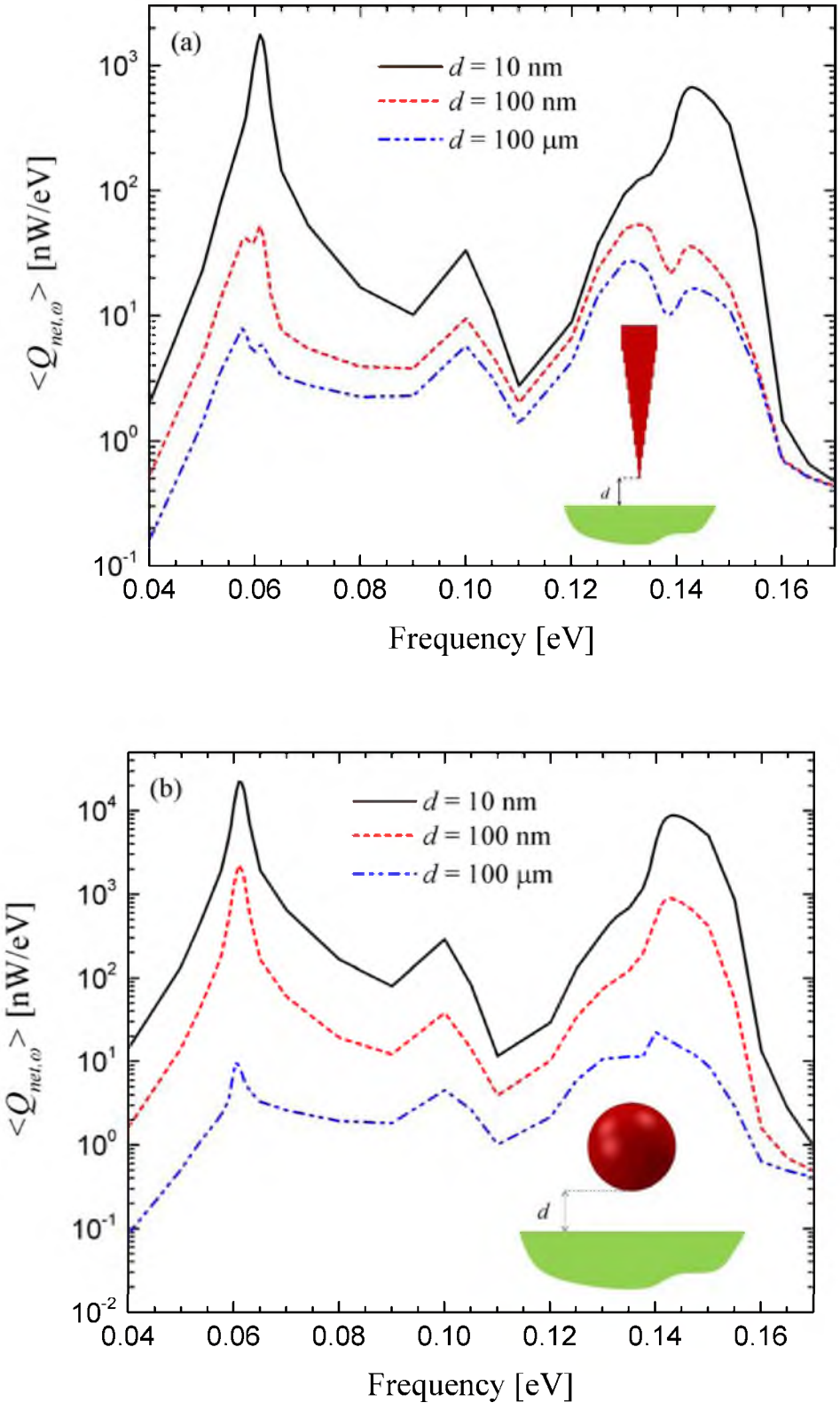

Figure 5.4 Net spectral heat rate between (a) a probe and a surface, and (b) a sphere and a surface for separation gaps d of 10 nm, 100 nm and 100 μm. The sphere and the probe are at T_2 = 400 K, while the surface is at T_1 = 300 K.

power absorbed by an electric dipole is proportional to Im(α_j), where α_j ($j = x, y, z$) is the dipole polarizability tensor given by [48,49]:

$$\alpha_j = \frac{4\pi}{3}\varepsilon_0 a_x a_y a_z \frac{\varepsilon_2 - 1}{1 + L_j(\varepsilon_2 - 1)} \tag{5.28}$$

where a_x, a_y and a_z are the dimensions of the dipole along the x-, y- and z-directions. The geometrical factors L_j, determined solely from the dipole geometry, satisfy $\sum_{j=x,y,z} L_j = 1$ and $L_j \geq 0$. For a spherical dipole, $L_x = L_y = L_z = 1/3$ such that Eq. (5.28) reduces to the Clausius-Mossotti polarizability with resonant enhancement when $|\varepsilon_2 + 2|$ is minimum. In this limit, LSPh resonances are predicted at frequencies of 0.0605 eV and 0.1410 eV, which is in good agreement with the resonances of the heat rate for the case of a sphere located 100 μm above the surface (0.0605 eV and 0.1400 eV). For the probe, LSPh resonances can be estimated by considering a prolate spheroidal dipole having a major axis a_z equal to the probe length of 4.97 μm. The minor axes a_x and a_y are the same and are equal to 321 nm such that the spheroid and the probe have the same volume. For these dimensions, the geometrical factors needed to calculate the polarizability tensor are $L_x = L_y = 0.495$ and $L_z = 0.010$. Thus, resonant enhancement due to LSPhs for the case of a prolate spheroidal electric dipole occurs along the major axis and minor axes when $|\varepsilon_2 + 99|$ and $|\varepsilon_2 + 1.02|$ are minimum, respectively. In this limit, four resonant modes along the minor axes are predicted at frequencies of 0.0575 eV, 0.0615 eV, 0.1325 eV and 0.1450 eV. These predictions are in good agreement with the resonant modes of the heat rate profile for a probe located 100 μm above the surface.

As the gap decreases to 100 nm and 10 nm, the heat rate for both the probe and sphere cases increases due to the additional contribution of evanescent modes, and

particularly due to SPhPs supported by the surface. In the near field, the sphere is optically thick and its diameter is much larger than the gap distance, such that heat transfer can be approximated as a summation of local heat rates between two parallel surfaces with varying gap thicknesses (proximity approximation) [13,15]. Consequently, the resonant frequencies of the near-field heat rate profiles are essentially the same as the SPhP resonant frequencies of the surface. In the proximity approximation limit, the total near-field conductance, which is proportional to the net total heat rate, is calculated as:

$$G(T) = \lim_{\delta T \to 0} \frac{\langle Q_{net} \rangle}{\delta T} = \int_A h(\tilde{d}, T)\, dA \tag{5.29}$$

where $\tilde{d}$ is the local distance between two parallel surfaces and h is the heat transfer coefficient in the two-surface configuration that follows a $\tilde{d}^{-2}$ power law [39] . For a sphere and a surface, Eq. (5.29) results in a d^{-1} power law for small gaps up to approximately 100 nm [13]. This is shown in Fig. 5.5, where the sphere-surface total heat rate is plotted as a function of the separation gap (10 nm to 100 nm).

The probe-surface spectral heat rate for a 100-nm-thick gap is similar to the far-field profile, where both low- and high-frequency resonance splitting mediated by LSPhs along the minor axis of the probe is observed. However, when the gap reduces to 10 nm, which is smaller than the probe tip size of 57.8 nm, resonance splitting does not occur. Instead, the resonances are aligned with those of the sphere-surface configuration in the near field, and thus essentially correspond to SPhP modes of the surface. Here, heat transfer is dominated by SPhPs with penetration depth approximately equal to the gap size and thus smaller than the probe tip size [50]. Consequently, the heat rate between the probe and the surface can also be estimated using the proximity approximation. For a

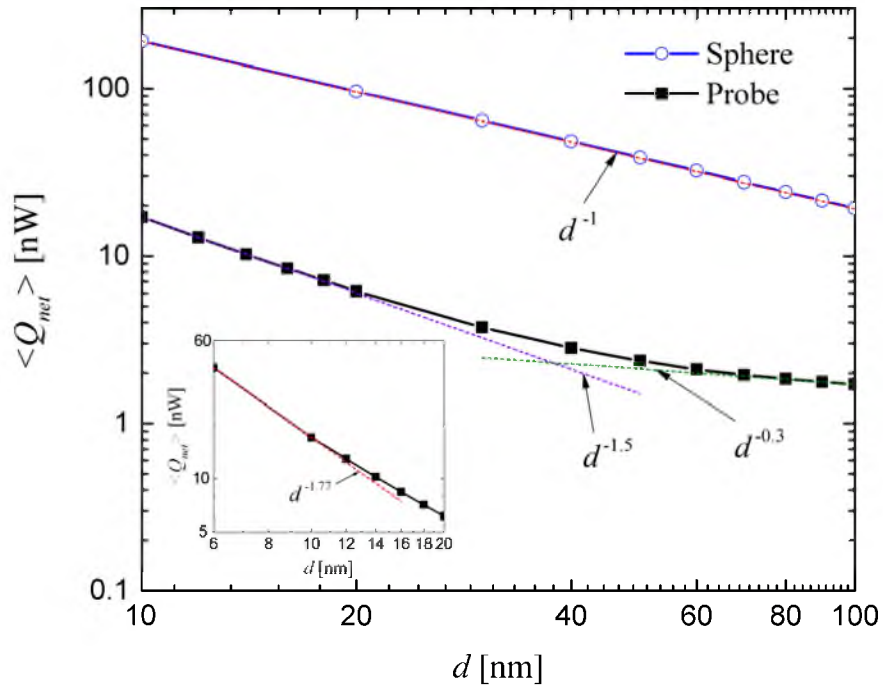

Figure 5.5 Net total heat rate in the near field as a function of the separation gap d for the probe-surface and sphere-surface configurations.

probe with a flat tip, the total heat rate is expected to follow a d^{-2} power law in the limit that $d \to 0$ since $\tilde{d}$ in Eq. (5.29) is independent of the surface area A. Near a 10-nm-thick gap, Fig. 5.5 shows that the heat rate varies as $d^{-1.5}$ while a $d^{-0.3}$ power law is observed around a gap size of 100 nm. It can be seen in the inset of Fig. 5.5 that the heat rate decays as $d^{-1.77}$ near a gap size of 6 nm, such that the d^{-2} regime is expected to arise at an extremely small gap where the validity of fluctuational electrodynamics is questionable. From these results, it is concluded that the d^{-2} regime is reached when the probe tip size is larger than the gap by more than one order of magnitude. Note that for a spheroid and a cone above a surface, the integration of Eq. (5.29) leads to d^{-1} and $\log(d^{-1})$ power laws, such that these geometries do not represent well the heat rate between the probe and the surface in the framework of the proximity approximation.

To summarize, the decay rate of the probe-surface near-field heat transfer decreases

as the gap thickness increases. When the gap size is much smaller than the probe tip size, SPhP mediated heat transfer between the probe and the surface occurs such that the heat rate follows a power law approaching d^{-2}. For gap sizes of the same order of magnitude as or larger than the probe tip size, the near-field heat rate is mediated by coupled SPhP and LSPh (along the minor axis of the probe) modes, resulting in a decay rate of $d^{-0.3}$. In the far field, heat transfer between the probe and the surface is dominated by LSPhs. The spatial distribution of volumetric heat rate, normalized by its maximum value, at the low-frequency resonance is plotted for SPhP (10 nm), coupled SPhP-LSPh (100 nm) and LSPh (100 μm) mediated heat transfer. For 100 nm and 100 μm gaps, the first mode of the low-frequency resonance is considered. Note that the spatial distribution of volumetric heat rate is shown for a cross-section parallel to the y-z plane passing through the central axis of the probe. It is clear from Fig. 5.6 that as the contribution of SPhPs increases, the heat absorbed by the probe is essentially concentrated at its tip. As a final remark, note that the peak observed at 0.10 eV in Fig. 5.4 is due to a local maximum in the imaginary part of the dielectric function of silica leading to increased radiation absorption by the object and enhanced contribution of frustrated modes in the near field. As the distance between the object and the surface decreases, the contribution from this peak decreases and becomes essentially negligible at a gap distance of 10 nm where the heat rate is dominated by SPhPs.

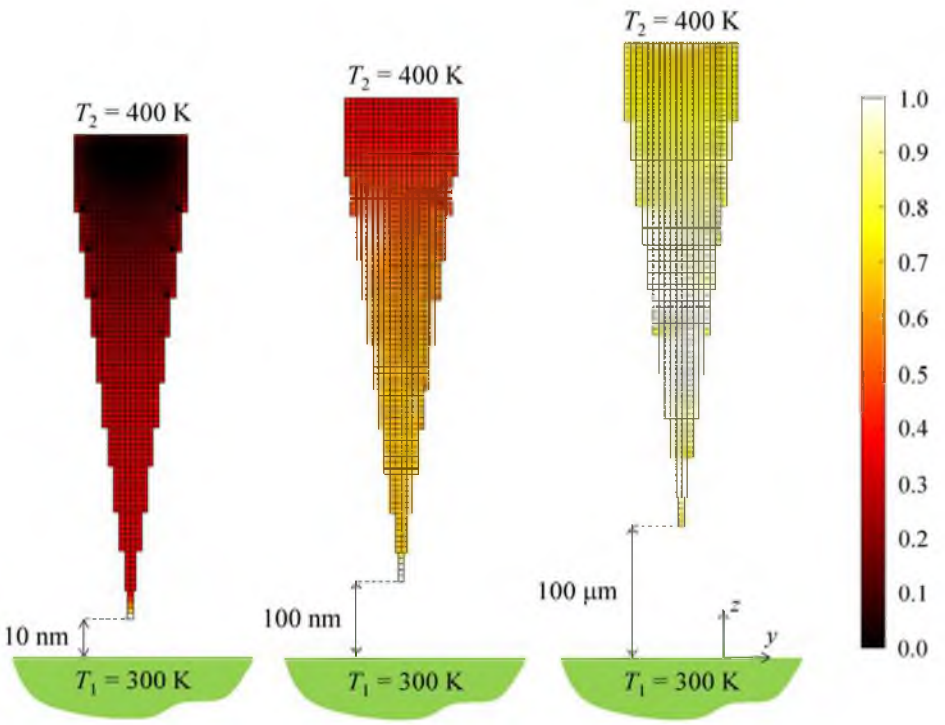

Figure 5.6 Spatial distribution of normalized volumetric heat rate within the probe at the low-frequency resonance for gap sizes d of 10 nm, 100 nm and 100 μm.

5.4.2 Validity of the spheroidal electric dipole approximation for modeling near-field radiative heat transfer between a probe and a surface

The validity of the spheroidal electric dipole model for approximating near-field radiative heat transfer between a probe and a surface is analyzed. Note that the spherical electric dipole approximation is not considered, as it cannot predict the splitting of the low- and high-frequency resonances of the spectral heat rate profile (see Fig. 5.4(a)). The net spectral heat rate between an electric dipole and a surface is given by [17,19]:

$$\left\langle Q_{net,\omega} \right\rangle = \frac{2\omega^4 \mu_0^2 \varepsilon_0 \varepsilon_1''}{\pi} \left[\Theta(\omega, T_2) - \Theta(\omega, T_1) \right] \sum_{j=x,y,z} \left(\mathrm{Im}(\alpha_j) \sum_{k=x,y,z} \int_{V_1} \left| G_{jk}^T(\mathbf{r}_2, \mathbf{r}', \omega) \right|^2 d^3\mathbf{r}' \right) \tag{5.30}$$

where α_j is the polarizability tensor given by Eq. (5.28) and $\mathbf{r}_2$ is the distance between the centroid of the dipole and the surface. Figure 5.7 shows the net spectral heat rate for the

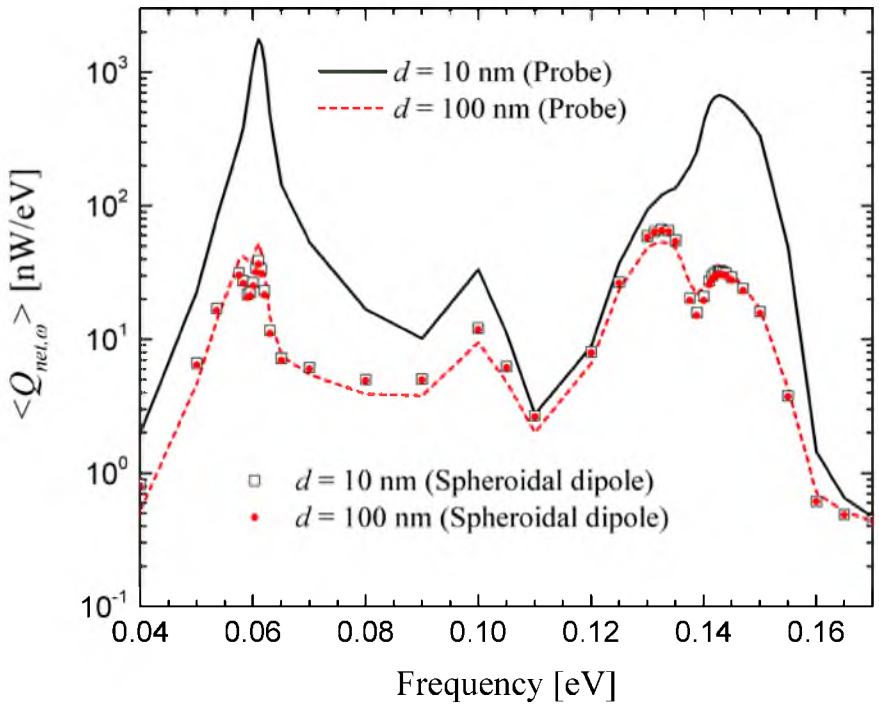

Figure 5.7 Net spectral heat rate between a probe and a surface for gap sizes d of 10 nm and 100 nm. Results are compared against the spheroidal electric dipole model.

prolate spheroidal dipole and probe discussed in Section 5.4.1 at separation gaps d of 10 nm and 100 nm, while the net total heat rate is provided in Fig. 5.8 for gaps ranging from 10 nm to 500 nm. The spheroidal electric dipole model predicts low- and high-frequency resonance splitting regardless of the gap size. As discussed previously, these four resonances are due to LSPhs associated with the minor axes of the prolate spheroidal dipole and are thus independent of the gap size. It can be seen in Fig. 5.8 that the total near-field heat rate in the spheroidal dipole approximation is a weak function of the gap size. This is due to the fact that the dipole centroid is located at a distance $d + a_z/2$ (a_z = 4.97 μm) above the surface, such that variations of d by a few tens to a few hundreds of nanometers do not significantly affect heat transfer.

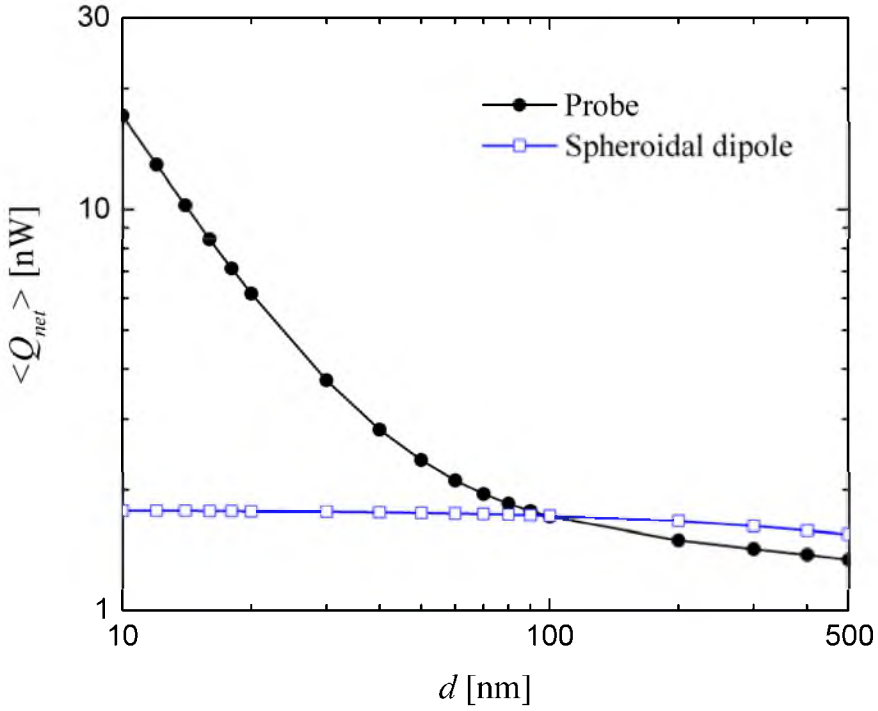

Figure 5.8 Net total heat rate between a probe and a surface as a function of the separation gap d. Results are compared against the spheroidal electric dipole model.

According to Ref. [19], the spheroidal dipole model is expected to provide reliable results when the wavelength λ and the gap d is larger than $a_{max} = \max\{a_x,a_y,a_z\}$. Figure 5.8 however suggests that starting at a gap size of approximately 70 nm, where the probe tip size is smaller than the gap size, the spheroidal dipole model approximates reasonably well the heat rate between a probe and a surface. In addition, as discussed in Section 5.4.1, the resonant modes of the probe-surface heat rate are well predicted by the spheroidal dipole approximation when heat transfer is mediated by coupled SPhPs-LSPhs. For a spheroidal dipole, a more appropriate criterion should require that the gap thickness d be much larger than the radius of curvature R of the spheroidal dipole tip facing the surface (R = 10.4 nm). When $d >> R$, multiple reflections between the probe and the surface can be ignored. This new criterion assessing the applicability of the

spheroidal dipole approximation to model the heat rate between a probe and a surface is in line with the results observed in Figs. 5.7 and 5.8. Yet, the total heat rates obtained for the probe and the spheroidal dipole are not in perfect agreement, and some discrepancies can be observed between gaps of 100 nm and 500 nm. As seen in Fig. 5.7 at a gap size of 100 nm, the spheroidal dipole model overestimates the heat rate associated with the first mode of the high-frequency resonance (0.1325 eV). This can be explained by the fact that the material wavelength corresponding to that frequency is 3.93 μm, which is of the same order of magnitude as the major axis of the spheroid. In the SPhP regime, where the probe tip size is larger than the gap size, the spheroidal dipole model cannot be used for approximating heat transfer between a probe and a surface, both in terms of resonance and total heat rate predictions, since the criterion $d >> R$ is not respected. For this case, the proximity approximation can be employed to estimate the heat rate and resonant modes in the probe-surface configuration.

5.5 Conclusions

A general formalism for modeling near-field radiative heat transfer between arbitrarily-shaped objects and an infinite surface was proposed. The thermal discrete dipole approximation (T-DDA) was used to discretize the volume integral equation for the electric field derived from fluctuational electrodynamics, while the surface interactions were treated analytically using Sommerfeld's theory of electric dipole radiation above an infinite plane. The framework was applied to near-field radiative heat transfer between a complex-shaped probe and a surface both made of silica. The study revealed that when the probe tip size is much larger than the separation gap d, surface

phonon-polariton (SPhP) mediated heat transfer occurs such that the resonances of the heat rate correspond essentially to those of a single surface while the total heat rate approaches a d^{-2} power law as $d \rightarrow 0$. It was also found that coupled localized surface phonon (LSPh)-SPhP mediated heat transfer arises when the probe tip size is approximately equal to or smaller than the separation gap. In that case, the spectral heat rate exhibits four resonant modes due to LSPhs along the minor axis of the probe while the total heat rate in the near field convergences to a $d^{-0.3}$ regime. Finally, it was demonstrated that a prolate spheroidal electric dipole can approximate reasonably well near-field radiative heat transfer between a probe and a surface when the thermal wavelength is larger than the major axis of the spheroidal dipole and when the separation gap is much larger than the radius of curvature of the dipole tip facing the surface. The framework presented in this paper is not restricted to the probe-surface configuration, and can be applied to cases involving an arbitrary number of objects with various sizes and shapes above an infinite plane.

5.6 Supplemental Materials

5.6.1 Verification of the thermal discrete dipole approximation (T-DDA) with surface interaction

The T-DDA is verified by comparison against the exact solution of the heat rate between a sphere and a surface [10]. The problem parameters are the same as those discussed in the introduction of Section 5.4. The surface and the 1.6-μm-diameter sphere are both made of silica and are maintained at temperatures T_1 = 300 K and T_2 = 400 K, respectively. It is also assumed that there is no incident electric field. Figure 5.9 shows

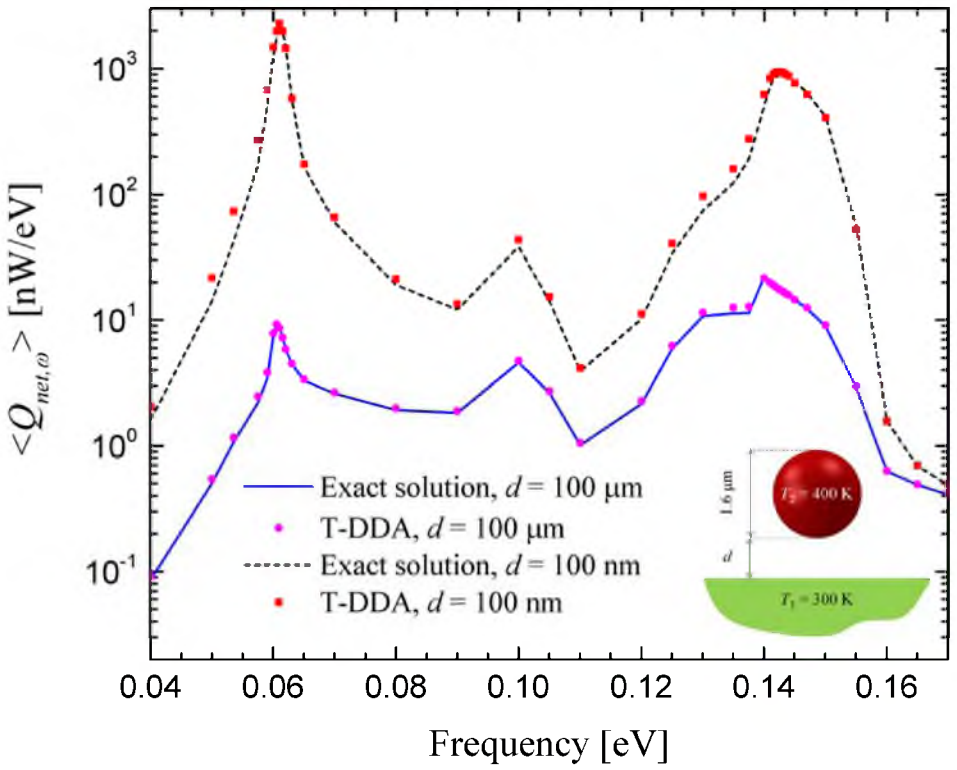

Figure 5.9 Net spectral heat rate between a sphere and a surface for separation gaps d of 100 nm and 100 μm obtained with the T-DDA and the exact solution [10]. The sphere is at a temperature T_2 = 400 K, while the surface is at T_1 = 300 K.

the net spectral heat rate obtained from the exact solution and the T-DDA for separation gaps d of 100 nm and 100 μm.

The convergence of the T-DDA depends strongly on the dielectric function of the discretized object [16]. As the dielectric function increases, the wavelength and the decay length of the electric field (skin depth) inside the object shrinks. As such, the subvolume size resulting in a converged solution decreases as the dielectric function increases. Additionally, a large dielectric function negatively affects the T-DDA convergence by amplifying the shape error [16]. Since the dielectric function of silica varies significantly with the frequency in the infrared band (see Fig. 5.10), a frequency-dependent nonuniform discretization was used for calculating the net spectral heat rate. The number

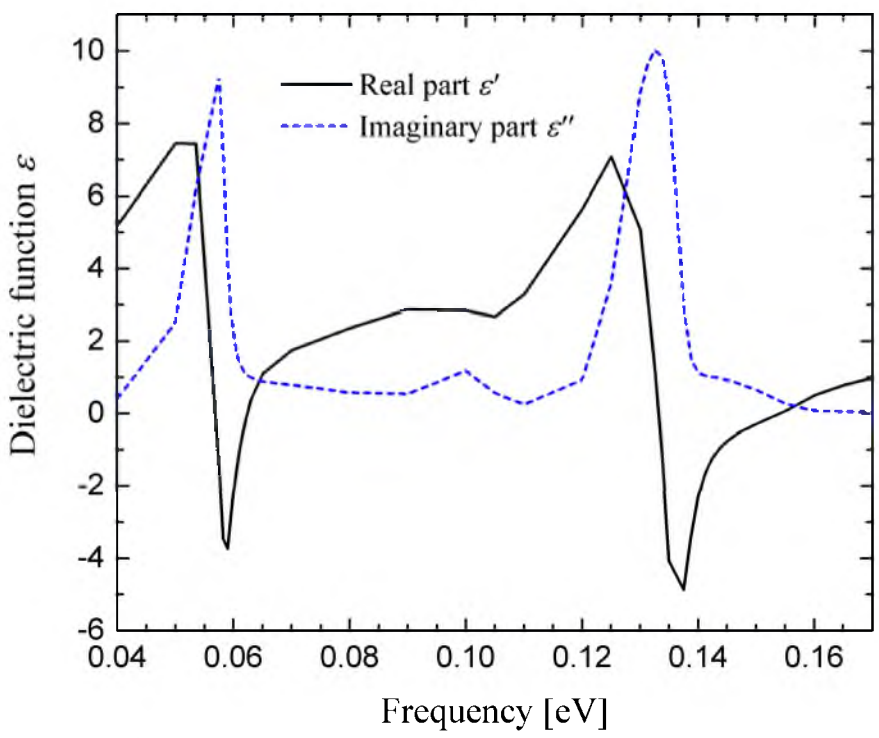

Figure 5.10 Dielectric function of silica obtained from Ref. [48].

of subvolumes employed for discretizing the sphere varied between 11536 and 33552 depending on the frequency. It can be seen in Fig. 5.9 that the T-DDA and exact results are in excellent agreement. The locations of the resonances and their magnitudes are predicted accurately via the T-DDA. The small discrepancy observed for frequencies ranging from 0.1300 eV to 0.1375 eV is due to the fact that the dielectric function of silica is large within that spectral band. A better accuracy could be obtained by employing a larger number of subvolumes, since the accuracy of the T-DDA increases as the subvolume size decreases [16]. Yet, increasing the number of subvolumes within the 0.1300-0.1375 eV spectral band is not necessary as its contribution to the net total heat rate is negligible. The satisfactory results obtained for the case of a sphere, which is one of the most difficult shapes to model with a cubical lattice, demonstrates that the T-DDA can accurately be used for modeling arbitrarily-shaped objects.

5.6.2 Energy density at different distances above a silica surface at 300 K

Figure 5.11 shows energy density at three distances d of 10 nm, 100 nm and 100 μm above the silica surface.

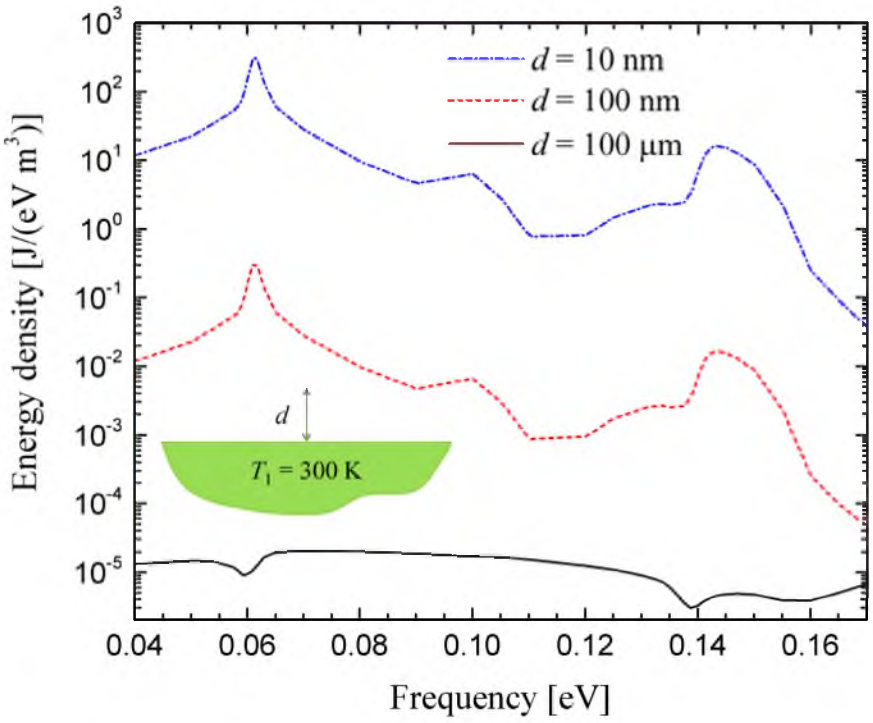

Figure 5.11 Spectral distribution of energy density at distances d of 10 nm, 100 nm and 100 μm above a silica surface at a temperature T_1 = 300 K.

5.7. References

[1] De Wilde Y., Formanek F., Carminati R., Gralak B., Lemoine P.-A., Joulain K., Mulet J.-P., Chen Y., and Greffet J.-J., Thermal radiation scanning tunnelling microscopy, *Nature* **444**, 740-743, 2006.

[2] Jones A.C. and Raschke M.B., Thermal infrared near-field spectroscopy, *Nano Letters* **12**, 1475-1481, 2012.

[3] Babuty A., Joulain K., Chapuis P.-O., Greffet J.-J. and De Wilde Y., Blackbody spectrum revisited in the near field, *Physical Review Letters* **110**, 146103, 2013.

[4] O'Callahan B.T., Lewis W.E., Jones A.C. and Raschke M.B., Spectral frustration and spatial coherence in thermal near-field spectroscopy, *Physical Review B* **89**, 245446, 2014.

[5] Mamin H.J., Thermal writing using a heated atomic force microscope tip, *Applied Physics Letters* **69**, 433, 1996.

[6] Wilder K., Quate C.F., Adderton D., Bernstein R. and Elings V., Noncontact nanolithography using the atomic force microscope, *Applied Physics Letters* **73**, 2527, 1998.

[7] Hawes E.A., Hastings J.T., Crofcheck C. and Mengüç M.P., Spatially selective melting and evaporation of nanosized gold particles, *Optics Letters* **33**, 1383-1385, 2008.

[8] Guha B., Otey C., Poitras C.B., Fan S. and Lipson M., Near-field radiative cooling of nanostructures, *Nano Letters* **12**, 4546-4550, 2012.

[9] Krüger M., Emig T., and Kardar M., Nonequilibrium electromagnetic fluctuations: heat transfer and interactions, *Physical Review Letters* **106**, 210404, 2011.

[10] Otey C. and Fan S., Numerically exact calculation of electromagnetic heat transfer between a dielectric sphere and plate, *Physical Review B* **84**, 245431, 2011.

[11] Kittel A., Müller-Hirsch W., Parisi J., Biehs S.-A., Reddig D. and Holthaus M., Near-field radiative heat transfer in a scanning thermal microscope, *Physical Review Letters* **95**, 224301, 2005.

[12] Narayanaswamy A., Shen S. and Chen G., Near-field radiative heat transfer between a sphere and a substrate, *Physical Review B* **78**, 115303, 2008.

[13] Rousseau E., Siria A., Jourdan G., Volz S., Comin F., Chevrier J. and Greffet J.-J., Radiative heat transfer at the nanoscale, *Nature Photonics* **3**, 514-517, 2009.

[14] Joulain K., Ben-Abdallah P., Chapuis P.-O., De Wilde Y., Babuty A. and Henkel C., Strong tip–sample coupling in thermal radiation scanning tunneling microscopy, *Journal of Quantitative Spectroscopy and Radiative Transfer* **136**, 1-15, 2014.

[15] Sasihithlu K. and Narayanaswamy A., Proximity effects in radiative heat transfer, *Physical Review B* **83**, 161406(R), 2011.

[16] Edalatpour S., Čuma M., Trueax T., Backman R. and Francoeur M., Convergence analysis of the thermal discrete dipole approximation, *Physical Review E* **91**, 063307, 2015.

[17] Mulet J.-P, Joulain K., Carminati R. and Greffet J.-J., Nanoscale radiative heat transfer between a small particle and a plane surface, *Applied Physics Letter* **78**, 2931, 2001.

[18] Biehs S.-A., Huth O. and Rüting F., Near-field radiative heat transfer for structured surfaces, *Physical Review B* **78**, 085414, 2008.

[19] Huth O., Rüting F., Biehs S.-A. and Holthaus M., Shape-dependence of near-field heat transfer between a spheroidal nanoparticle and a flat surface, *The European Physical Journal* **50**, 10603, 2010.

[20] Rodriguez A.J., Ilic O., Bermel P., Celanovic I., Joannopoulos J. D., Soljacic M., and Johnson S.G., Frequency-selective near-field radiative heat transfer between photonic crystal slabs: A computational approach for arbitrary geometries and materials, *Physical Review Letters* **107**, 114302, 2011.

[21] Rodriguez A.W., Reid M.T.H. and Johnson S.G., Fluctuating-surface-current formulation of radiative heat transfer for arbitrary geometries, *Physical Review B* **86**, 220302(R), 2012.

[22] Didari A. and Mengüç M.P., Analysis of near-field radiation transfer within nano-gaps using FDTD method, *Journal of Quantitative Spectroscopy and Radiative Transfer* **146**, 214-226, 2014.

[23] Edalatpour S. and Francoeur M., The Thermal Discrete Dipole Approximation (T-DDA) for near-field radiative heat transfer simulations in three-dimensional arbitrary geometries, *Journal of Quantitative Spectroscopy and Radiative Transfer* **133**, 364 -373, 2014.

[24] Polimeridis A.G., Reid M.T.H., Jin W., Johnson S.G., White J.K. and Rodriguez A.W., Fluctuating volume-current formulation of electromagnetic fluctuations in inhomogeneous media: Incandescence and luminescence in arbitrary geometries, *Physical Review B* **92**, 134202, 2015.

[25] McCauley A.P., Reid M.T.H., Krüger M. and Johnson S.G., Modeling near-field radiative heat transfer from sharp objects using a general three-dimensional numerical scattering technique, *Physical Review B* **85**, 165104, 2012.

[26] Rytov S.M., Kravtsov Y.A. and Tatarskii V.I., *Principles of Statistical Radiophysics 3: Elements of Random Fields*, Springer, New York, 1989.

[27] Edalatpour S., DeSutter J. and Francoeur M., Near-field thermal electromagnetic transport: An overview, *Journal of Quantitative Spectroscopy and Radiative Transfer* **178**, 14-21, 2016.

[28] Sommerfeld A., On the propagation of waves in wireless telegraphy, *Annals of Physics* **81**, 1135, 1926.

[29] Taubenblatt M.A., Light scattering from cylindrical structures on surfaces, *Optics Letters* **15**, 255 -257, 1990.

[30] Taubenblatt M.A. and Tran T.K., Calculation of light scattering from particles and structures on a surface by the coupled-dipole method, *Journal of the Optical Society of America A* **10**, 912 -919, 1993.

[31] Schmehl R., *The coupled-dipole method for light scattering from particles on plane surfaces*, M.S. Thesis, Arizona State University, 1994.

[32] Schmehl R., Nebeker B.M. and Hirleman E.D., Discrete-dipole approximation for scattering by features on surfaces by means of a two-dimensional fast Fourier transform technique, *Journal of the Optical Society of America A* **14**, 3026 -3036, 1997.

[33] Nebeker B.M., *Modeling of light scattering from features above and below surfaces using the discrete-dipole approximation*, Ph.D. thesis, Arizona State University, 1998.

[34] Loke V.L.Y. and Mengüç M.P., Surface waves and atomic force microscope probe-particle near-field coupling: Discrete dipole approximation with surface interaction, *Journal of the Optical Society of America A* **27**, 2293-2303, 2010.

[35] Loke V.L.Y., Mengüç M.P. and Nieminen T.A., Discrete-dipole approximation with surface interaction: Computational toolbox for MATLAB, *Journal of Quantitative Spectroscopy and Radiative Transfer* **112**, 1711-1725, 2011.

[36] Yurkin M.A. and Huntemann M., Rigorous and fast discrete dipole approximation for particles near a plane interface, *The Journal of Physical Chemistry C* **119**, 29088, 2015.

[37] Kim K., Song B., Fernández-Hurtado V., Lee W., Jeong W., Cui L., Thompson D., Feist J., Reid M.T.H., García-Vidal F.J., Carlos Cuevas J., Meyhofer E. and Reddy P., Radiative heat transfer in the extreme near field, *Nature* **528**, 387–391, 2015.

[38] J.E. Sipe, New Green-function formalism for surface optics, *Journal of the Optical Society of America B* **4**, 481 -489, 1987.

[39] Joulain K., Mulet J.-P., Marquier F., Carminati R. and Greffet J.-J., Surface electromagnetic waves thermally excited: Radiative heat transfer, coherence properties and Casimir forces revisited in the near field, *Surface Science Reports* **57**, 59-112, 2005.

[40] Baños A., *Dipole Radiation in the Presence of a Conducting Half space*, Pergamon Press, Oxford, 1966.

[41] Chew W.C., *Waves and Fields in Inhomogeneous Media,* IEEE Press, 1995.

[42] Lytle R.J. and Lager D.L., *Numerical evaluation of Sommerfeld integrals*, Technical Report UCRL-51688, Lawrence Livermore Laboratory, Livermore, California, 1974.

[43] Lager D.L. and Lytle R.J., *FORTRAN subroutines for the numerical evaluation of Sommerfeld integrals*, Technical Report UCRL-51688, Lawrence Livermore Laboratory, Livermore, California, 1974.

[44] Novotny L. and Hecht B., *Principles of Nano-Optics*, Cambridge University Press, New York, 2006.

[45] Mishchenko M.I., *Electromagnetic Scattering by Particles and Particle Groups*, Cambridge University Press, Cambridge, 2014.

[46] Lau W.T., Shen J.-T., Veronis G. and Fan S., Spatial coherence of the thermal electromagnetic field in the vicinity of a dielectric slab, *Physical Review E* **76**, 016601, 2007.

[47] Palik E.D., *Handbook of Optical Constants of Solids*, Academic Press, Boston, 1985.

[48] Bohren C.F. and Huffman D.R., *Absorption and Scattering of Light by Small*

Particles, Wiley-VCH, Weinheim, 2004.

[49] Maier S.A., *Plasmonics: Fundamentals and Applications*, Springer, New York, 2007.

[50] Francoeur M., Mengüç M.P. and Vaillon R., Spectral tuning of near-field radiative heat flux between two thin silicon carbide films, *Journal of Physics D: Applied Physics* **43,** 075501, 2010.

CHAPTER 6

INVESTIGATION OF RESONANCE REDSHIFT IN NEAR-FIELD THERMAL SPECTROSCOPY

6.1 Introduction

So far, most near-field thermal radiation experiments have measured total (rather than spectral) radiative heat transfer [1-10]. However, many potential applications capitalize on the quasi-monochromatic behavior of thermal radiation in the near field [11-21]. As such, measuring the near-field thermal spectrum is of critical importance. Spectral measurement of near-field thermal radiation has been attempted in three recent studies [22-24] using a near-field thermal spectroscopy technique. In this technique, as shown in Fig. 6.1, the near-field thermal energy of a sample is scattered using a subwavelength probing tip brought within a subwavelength distance from the sample surface. Typical probes have a sharp tip size of approximately 100 nm, while the probe height can be as large as 10 μm [24]. The distance between the probe and the sample varies in a range of 0 to about 100 nm [24]. The evanescent component of thermal emission present in the near field is scattered by the probe into the far field in the form of propagating waves. The resulting signal, detected in the far field, is used to infer the spectral distribution of near-field thermal emission by the sample. The main challenge in this technique is to extract the near-field thermal spectrum from the measured far-field signal. Particularly, recent

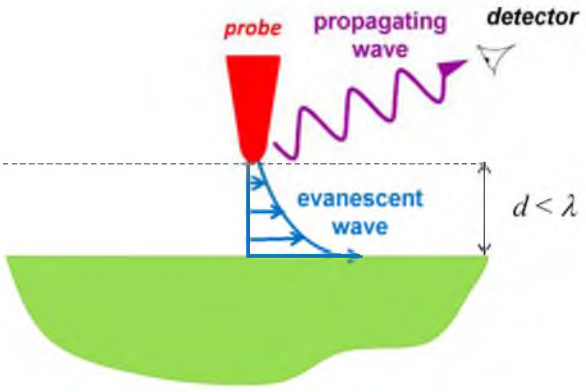

Figure 6.1 Probe-sample interactions in near-field thermal spectroscopy.

studies [23,24] reported that the resonant frequency of the measured far-field signal is spectrally redshifted compared to the resonant frequency of thermal emission by the sample in the near field as predicted by fluctuational electrodynamics. The measured redshift ranges from 5 cm^{-1} to 50 cm^{-1} [23,24]. It is not clear if the observed resonance redshift is due to a physical phenomenon happening during the interaction between the probe and the sample or if it is an experimental artifact. A physical model capable of simulating the interaction between the probe and the sample is required to answer this question. Due to the complex shape of the probe, an analytical solution is unattainable. In addition, numerical methods are difficult to apply to such a multiscale problem due to the prohibitive calculation time associated with discretizing a sample that is many orders of magnitude larger than the probe. A few approximate models [23-25] have been applied to the probe-sample problem, but none of them was able to explain the physics underlying the resonance redshift.

The resonance redshift is undesired, because it prevents a one-to-one relationship between the near-field thermal spectrum and the measured far-field signal. Understanding probe-sample interactions is crucial for the interpretation of the measured signal and for

designing an experimental setup that prevents the resonance redshift. In addition to near-field thermal spectroscopy, an insight into the probe-sample interactions is beneficial for the establishment of techniques such as tip-based nanomanufacturing [26-29] and high-resolution imaging [30]. The objective of this chapter is to employ the T-DDA with surface interaction, which does not neglect any physical aspect of the probe-sample problem, to analyze the physics of the observed resonance redshift. A further investigation of the resonance redshift is performed by analyzing the heat flux between the sample and a thin film.

The rest of this chapter is organized as follows. The problem under investigation is described in Section 6.2. The T-DDA with surface interaction is applied to the probe-sample problem in Section 6.3. The resonance redshift is investigated in Section 6.4 by analyzing heat transfer between a thin film and the sample. The conclusions and the references of this chapter are provided in Sections 6.5 and 6.6, respectively.

6.2 Description of the problem

The interaction between the near-field thermal spectrum of a silicon carbide (SiC) sample at T_1 = 300 K and an intrinsic silicon (Si) probe at T_2 = 400 K is investigated. This choice of materials is based on the latest experiments performed by O'Callahan et al. [24]. The probe geometry is detailed in Fig. 5.3 of Chapter 5. The probe has a tip size of 57.8 nm, modeled as a rectangular cuboid, and has a height of 4.97 μm. The frequency-dependent dielectric function of SiC is approximated by a damped harmonic oscillator given by $\varepsilon_1 = \varepsilon_\infty \left(\omega^2 - \omega_{LO}^2 + i\Gamma\omega\right)/\left(\omega^2 - \omega_{TO}^2 + i\Gamma\omega\right)$ [31], where ω is the angular frequency and the high frequency dielectric constant ε_∞, the damping factor Γ,

the longitudinal optical phonon frequency ω_{LO}, and the transverse optical phonons frequency ω_{TO} take values of 6.7, 8.966×10^{11} s^{-1}, 1.825×10^{14} rad/s, and 1.494×10^{14} rad/s, respectively. The dielectric function of silicon is obtained from Ref. [31]. The frequency band of from 1.6×10^{14} rad/s to 1.9×10^{14} rad/s is considered hereafter. The dielectric functions of Si and SiC in this spectral band are shown in Fig. 6.2.

Near-field thermal emission by a SiC sample, characterized by the energy density, is shown in Fig. 6.3 at a distance d of 10 nm above the sample. The energy density exhibits a resonance at a frequency 1.785×10^{14} rad/s. At this frequency, the real part of the dielectric function of SiC is equal to -1.0 such that surface phonon-polaritons (SPhPs) are excited at the sample-vacuum interface [32]. The near-field spectrum of the SiC sample is perturbed by the Si probe and the scattered signal is measured in the far field. The resonance redshift of the far-field signal is discussed in the following sections.

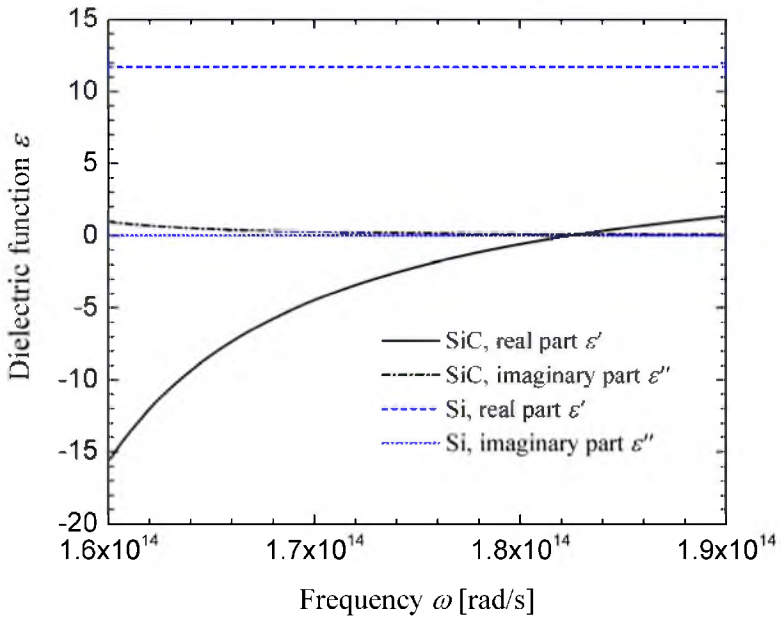

Figure 6.2 Dielectric functions of SiC and Si [31].

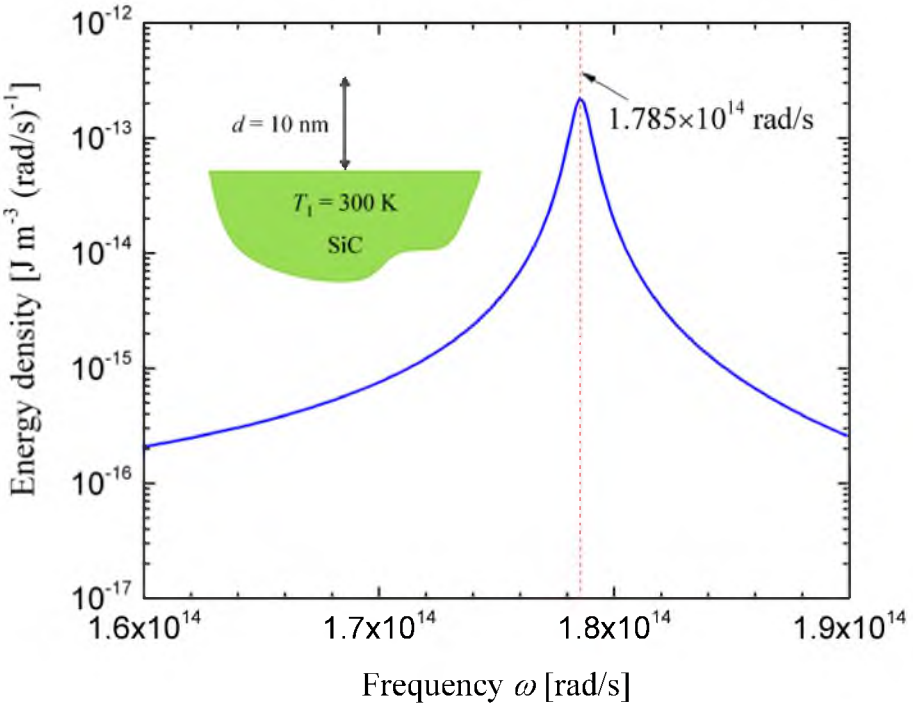

Figure 6.3 Energy density at distance d of 10 nm above a SiC sample at T_1 = 300 K.

6.3 T-DDA analysis of probe-sample interaction

The T-DDA with surface interaction, as discussed in details in Chapter 5, is used to establish a relationship between the far-field signal and the near-field spectrum of the sample. Near-field thermal emission by the sample at a distance d above its surface is proportional to the autocorrelation of the surface field, $\left\langle \left| \mathbf{E}^{sur} \right|^2 \right\rangle$, where the symbol < > denotes an ensemble average. The far-field signal is proportional to the correlation matrix of the induced dipole moments, $\left\langle \overline{\mathbf{P}}^{ind} \otimes \overline{\mathbf{P}}^{ind} \right\rangle$, and can be related to the surface field autocorrelation using the main equation of the T-DDA with surface interaction (Eq. (5.8)). To physically explain the probe-sample interaction, a simple case is considered in Section 6.3.1 where the probe is modeled using only one subvolume. The T-DDA simulations are performed in Section 6.3.2 using a sufficient number of subvolumes.

6.3.1 Spectral dependence of the far-field signal

The T-DDA with surface interaction is employed in this section to qualitatively analyze the spectral dependence of the far-field signal. For simplicity, the probe is modeled with a single subvolume. It is assumed that the probe is nonemitting, such that the thermally fluctuating dipole moment $\mathbf{p}^{fl}$ of the subvolume is zero and the total dipole moment $\mathbf{p}$ equals the induced dipole moment $\mathbf{p}^{ind}$. Also, the incident electric field due to external illumination is zero. Under these assumptions, Eq. (5.8) reduces to:

$$\frac{1}{\alpha^{CM}}\mathbf{p}^{ind}-\frac{1}{2\pi\varepsilon_0 a^3}\left[e^{ik_0 a}\left(1-ik_0 a\right)-1\right]\cdot\mathbf{p}^{ind}-\frac{k_0^2}{\varepsilon_0}\overline{\overline{\mathbf{G}}}^{R}\cdot\mathbf{p}^{ind}=\mathbf{E}^{sur} \tag{6.1}$$

where the subscript 1 is dropped for simplifying the nomenclature. The self-interaction of the probe, represented by the second term on the left-hand side of Eq. (6.1), is extracted from the radiative polarizability given by Eq. (5.10). In Eq. (6.1), α^{CM} is the Clausius-Mossotti polarizability, a is the radius of a sphere having the same volume as the probe, and $\overline{\overline{\mathbf{G}}}^{R}$ is the reflection dyadic Green's function. The induced dipole moment inside the probe can be derived from Eq. (6.1) as:

$$\mathbf{p}^{ind}=\alpha^{CM}\left(\frac{1}{2\pi\varepsilon_0 a^3}\left[e^{ik_0 a}\left(1-ik_0 a\right)-1\right]\cdot\mathbf{p}^{ind}+\frac{k_0^2}{\varepsilon_0}\overline{\overline{\mathbf{G}}}^{R}\cdot\mathbf{p}^{ind}+\mathbf{E}^{sur}\right) \tag{6.2}$$

According to Eq. (6.2), the dipole moment of the probe is the multiplication of the probe polarizability by the total electric field inside the probe given by the summation of the terms inside the parentheses. The electric field inside the probe has three components. The first and second terms are due to emission by the probe intercepted by itself directly and after interacting with the surface, respectively, and the third term indicates thermal emission by the sample. Equation (6.2) implies that the spectral distribution of the far-

field signal, determined by the induced dipole moment $\mathbf{p}^{ind}$, depends on the spectrum of the probe polarizability, direct self-interaction of the probe, indirect self-interaction of the probe through reflection at the surface and near-field thermal emission by the sample. The polarizability and direct self-interaction of the probe mostly depend on its dielectric function that is almost constant in the considered spectral band (see Fig. 6.2). The reflection interaction of the probe with the surface is a function of the probe dielectric function, the size and shape of the probe, as well as the dielectric function of the sample. The dielectric function of SiC varies strongly in the considered spectral band, which can result in a nonuniform spectral distribution of the reflection-interaction field. The spectrum of $\mathbf{p}^{ind}$ is the superposition of the spectral distributions of the surface field and the reflection-interaction field. As such, any shift in the resonant frequency of the induced dipole moment compared to the surface field can only be due to the reflection interactions of the probe and the sample.

6.3.2 T-DDA simulations

The net spectral heat rate between the probe and the sample is simulated using the T-DDA. Both the probe heat rate and the far-field signal are proportional to the correlation matrix of the induced dipole moments. As such, the same spectral dependency is expected for the two quantities. The probe is discretized into 13111 nonuniform cubical subvolumes. The size of the subvolumes varies from 5.78 nm at the probe tip to 57.8 nm at its base. The reflection interaction between the probe and the sample is accounted for in the T-DDA via the reflection-interaction matrix $\overline{\overline{\mathbf{R}}}$ which contains reflection dyadic Green's functions of subvolumes (see Eq. (5.11)). Figure 6.4 shows the net spectral heat

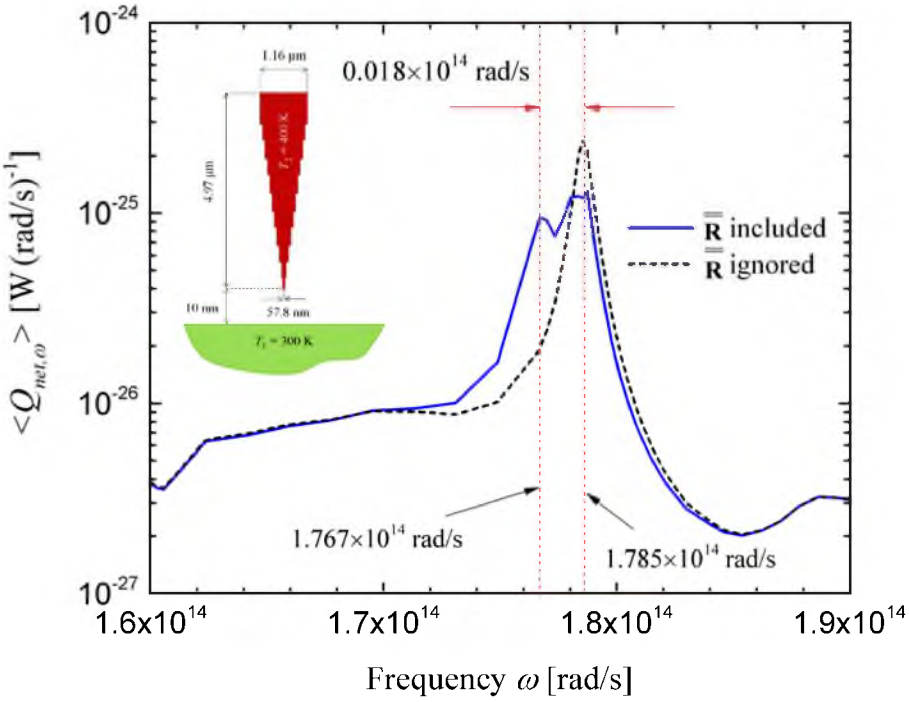

Figure 6.4 Net spectral heat rate between the probe and the sample with and without considering reflection interactions modeled using the reflection-interaction matrix $\overline{\overline{\mathbf{R}}}$. The reflection-interaction resonance is redshifted by 0.018×10^{14} rad/s (9.6 cm^{-1}) relative to the SPhP resonance of a single SiC sample.

rate between the probe and the sample with and without considering the reflection-interaction matrix. When reflection interactions are ignored, the resonant frequency of the heat rate is aligned with the SPhP resonance of a single SiC surface. The reflection interactions play a significant role in the spectral band from 1.7×10^{14} rad/s to 1.8×10^{14} rad/s, where they induce an additional resonance in the heat rate spectrum at a frequency of 1.767×10^{14} rad/s. This resonance is redshifted by 0.018×10^{14} rad/s (9.6 cm^{-1}) relative to the SPhP resonance of a single SiC surface. The location and magnitude of this resonance strongly depends on the shape and size of the probe as well as the gap thickness. Depending on the probe geometry and its distance from the surface, the reflection-interaction resonance might dominate SPhP resonance in the far-field signal.

The physical mechanism that amplifies the reflection-interaction contribution in the aforementioned spectral band can be investigated using Eq. (5.17). The physical interpretation of this equation is however not straightforward due to the complexity of the Sommerfeld integrals. In the next section, the probe is replaced with a thin film. The film-sample heat flux exhibits a similar spectral behavior to the probe-sample heat rate and is significantly simpler to analyze.

6.4 Spectral distribution of heat flux between the sample and a thin film

The heat flux between the SiC sample (medium 1) and a thin film of silicon (medium 2) separated by a vacuum gap show a similar spectral behavior as observed in the previous section for the probe-sample heat rate. In this case, the propagating and evanescent contributions to the monochromatic heat flux can be calculated analytically and are given by [32]:

$$\left\langle q_{\omega}^{\text{prop}} \right\rangle = \frac{\left[\Theta(\omega,T_2)-\Theta(\omega,T_1)\right]}{4\pi^2}\int_0^{k_0} k_\rho \sum_{\gamma=\text{TE,TM}} \frac{(1-\left|r_{01}^{\gamma}\right|^2)(1-\left|R_2^{\gamma}\right|^2)}{\left|1-r_{01}^{\gamma}R_2^{\gamma}e^{2ik_{z0}d}\right|^2}dk_\rho \tag{6.3}$$

$$\left\langle q_{\omega}^{\text{evan}} \right\rangle = \frac{\left[\Theta(\omega,T_2)-\Theta(\omega,T_1)\right]}{\pi^2}\int_{k_0}^{\infty} k_\rho e^{-2k''_{z0}d} \sum_{\gamma=\text{TE,TM}} \frac{\text{Im}(r_{01}^{\gamma})\,\text{Im}(R_2^{\gamma})}{\left|1-r_{01}^{\gamma}R_2^{\gamma}e^{2ik_{z0}d}\right|^2}dk_\rho \tag{6.4}$$

where Θ is the mean energy of an electromagnetic state [33], k_0 is the magnitude of the wavevector in vacuum (denoted as medium 0), k_ρ is the parallel component of the wavevector, $k_{zj}=k'_{zj}+ik''_{zj}$ is the z-component of the wavevector in medium j, TE and TM denote transverse electric and transverse magnetic polarizations, respectively, r_{01}^{γ} is the Fresnel reflection coefficient between medium 0 and 1 in polarization state γ [34] and R_2^{γ} is the film reflection coefficient in polarization state γ [32]. Figure 6.5 shows the

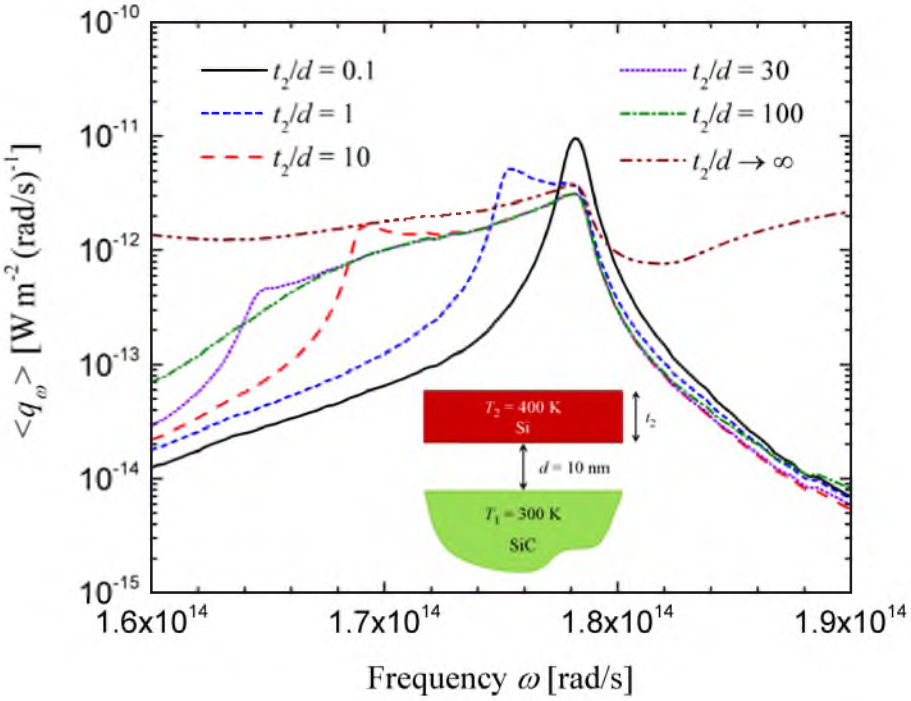

Figure 6.5 Spectral heat flux between a Si film of thickness t_2 separated from the SiC sample by a gap size d = 10 nm for various film thickness to gap size ratios.

spectral heat flux for different film thickness to gap ratios t_2/d ranging from 0.1 to 100 when d is fixed to 10 nm. The temperature of the SiC sample is T_1 = 300 K, while the Si film is kept at T_2 = 400 K. When t_2/d is in the order of 1~10, the heat flux spectrum exhibits a second resonance that is spectrally redshifted as t_2/d increases. When t_2/d = 1, the secondary resonance is redshifted by 0.031×10^{14} rad/s (16.5 cm^{-1}) relative to the SPhP resonance of a single SiC sample and it exceeds the SPhP heat flux by a factor of 1.35.

In Eqs. (6.3) and (6.4), the contributions from propagating and evanescent modes (in the vacuum gap) as well as TE and TM polarizations to the heat flux can be separated. Investigation of these four contributions reveals that the heat flux is dominated by evanescent modes in TM polarization. As such, the flux can be approximated as:

$$\langle q_\omega \rangle \approx \frac{[\Theta(\omega,T_2)-\Theta(\omega,T_1)]}{\pi^2}\int_{k_0}^{\infty} k_\rho e^{-2k''_{z0}d}\frac{\mathrm{Im}(r_{01}^{TM})\,\mathrm{Im}(R_2^{TM})}{\left|1-r_{01}^{TM}R_2^{TM}e^{2ik_{z0}d}\right|^2}dk_\rho \tag{6.5}$$

The terms $\mathrm{Im}(r_{01}^{TM})$ and $\mathrm{Im}(R_2^{TM})$ in Eq. (6.5) can be seen as the spectral near-field emittance and absorptance of media 1 and 2, respectively, while the term in the denominator accounts for the reflection interactions between the film and the sample [32]. For surface polaritons in the extreme near-field regime where $d << \lambda$, the most significant contribution to the heat flux is from very large values of k_ρ ($k_\rho >> k_0$) [32,35]. In this regime, the z-component of the wavevector in medium j can be estimated as $k_{zj} \approx ik_\rho$, and the following approximations can be made [32]:

$$r_{0j}^{TM} \approx \frac{\varepsilon_j - 1}{\varepsilon_j + 1}, \quad j = 1,2 \tag{6.6}$$

$$R_2^{TM} \approx \frac{r_{02}^{TM}\left(1-e^{-2k_\rho t_2}\right)}{1-(r_{02}^{TM})^2 e^{-2k_\rho t_2}} \tag{6.7}$$

According to Eq. (6.6), emission and absorption by the SiC sample, characterized by $\mathrm{Im}(r_{01}^{TM})$, are maximum when $\varepsilon_1' = -1$ and when losses are small. This condition is satisfied at a frequency of 1.785×10^{14} rad/s, where emission and absorption by the sample are dominated by the contribution of SPhPs. Emission and absorption by the Si film represented by $\mathrm{Im}(R_2^{TM})$ have a maximum value when the denominator of Eq. (6.7) is zero. This requires that the real part of the dielectric function be negative. The real part of the dielectric function of silicon in the considered spectral band is almost constant and approximately equal to 11.7, such that emission and absorption by the film cannot resonate.

The heat flux of the coupled film-sample system resonates at the poles of the

reflection-interaction term ($1/\left|1-r_{01}^{TM}R_2^{TM}e^{-2k_\rho d}\right|^2$). SiC supports SPhPs in the spectral band under study. For surface polaritons with the largest contributing wavevector approximately equal to d^{-1} [32], an asymptotic analysis of the reflection-interaction term predicts a resonance when $\varepsilon_1' = -1.25$. For SiC, this condition happens at a frequency of 1.777×10^{14} rad/s. The reflection-interaction term has another pole whose spectral location strongly depends on the film thickness and the gap size. For the case of $t_2 = d = 10$ nm, the reflection-interaction term resonates when $\varepsilon_1' \approx -2$ occurring at a frequency of 1.754×10^{14} rad/s. Figure 6.6 shows the TM evanescent component of the spectral heat flux per unit k_ρ for a gap size and a film thickness of 10 nm. A high-flux region is observed in the k_ρ-ω plane between k_ρ values from $10k_0$ to $150k_0$ and ω values from

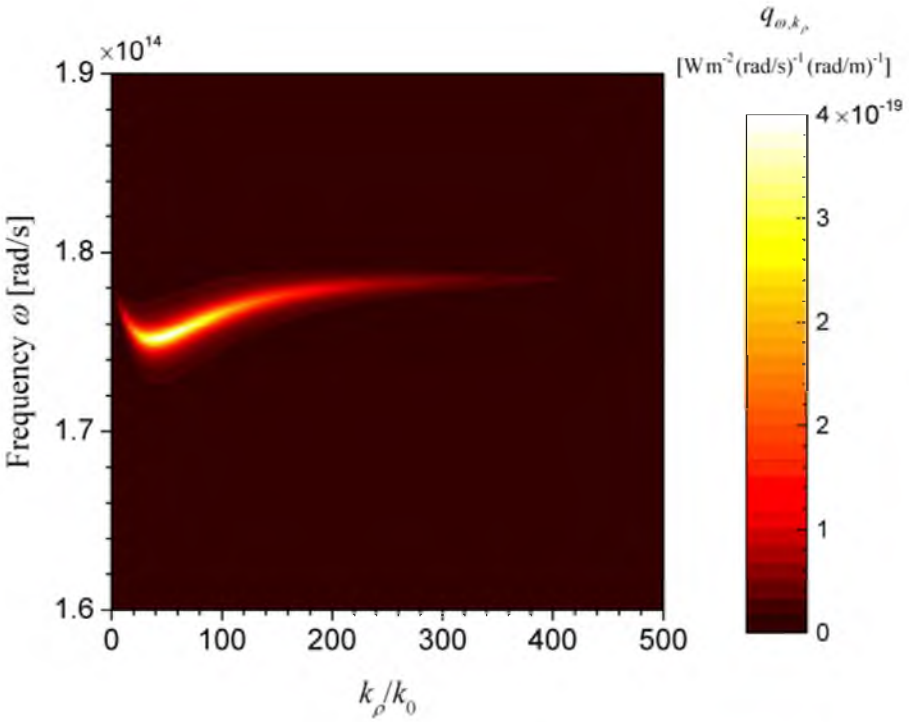

Figure 6.6 Spectral distribution of heat flux per unit k_ρ between a Si film and a SiC sample for film thickness t_2 and separation gap d of 10 nm. The film is at temperature T_2 of 400 K while the sample is kept at T_1 = 300 K.

1.75×10^{14} rad/s to 1.78×10^{14} rad/s. The high values of heat flux in this region are caused by the reflection interactions between the film and the sample. Figure 6.6 demonstrates the existence of a resonance redshift in the heat transfer spectrum which is in agreement with the T-DDA results and the experimental measurements. A close examination of reflection-interaction term is required to explain the physical mechanism responsible for enhanced reflection interactions in the aforementioned region, which is left as a future research effort.

6.5 Conclusions

The interactions between a Si probe and a SiC sample were analyzed using the T-DDA with surface interaction and by investigating the heat flux between the sample and a thin Si film. Both analyses suggested that reflection interactions between the Si object and the sample induce an additional resonance in the heat rate spectrum which is spectrally redshifted relative to the SPhP resonance. The magnitude and the location of this resonance depend on the size and the shape of the probe as well as the gap thickness. For a probe with a tip size of 57.8 nm and a height of 4.97 μm separated from the sample by a distance of 10 nm, this resonance redshift amounts to 0.018×10^{14} rad/s (9.6 cm^{-1}) which falls within the reported range of 5 cm^{-1} to 50 cm^{-1}. For some probe-sample configurations, the resonance due to reflection interactions might dominate SPhP resonance. In these cases, the resonant frequency of the far-field signal aligns with the reflection-interaction resonance rather than the SPhP resonance. For a 10-nm-thick film of Si separated from the sample by a gap of 10 nm, the heat flux at reflection-interaction resonance is larger than SPhP resonance by a factor of 1.35. A future research

recommendation would be to investigate the physical mechanism that is responsible for the enhanced reflection interactions. This would be beneficial for designing experimental setups that do not induce a resonance shift. Another recommendation for future work is to model the far-field signal rather than the heat rate. Since both the far-field signal and the heat rate are proportional to the induced dipole moment correlation matrix, it is expected that the spectral distributions of both quantities are similar. However, it would be beneficial to model the exact location and magnitude of the resonances of the far-field signal.

6.6 References cited

[1] Kittel A., Müller-Hirsch W., Parisi J., Biehs S.-A., Reddig D. and Holthaus M., Near-field radiative heat transfer in a scanning thermal microscope, *Physical Review Letters* **95**, 224301, 2005.

[2] Shen S., Narayanaswamy A. and Chen G., Surface phonon polaritons mediated energy transfer between nanoscale gaps, *Nano Letters* **9**(8), 2909-2913, 2009.

[3] Shen S., Mavrokefalos A., Sambegoro P. and Chen G., Nanoscale thermal radiation between two gold surfaces, *Applied Physics Letters* **100**, 233114, 2012.

[4] Hu L., Narayanaswamy A., Chen X.Y. and Chen G., Near-field thermal radiation between two closely spaced glass plates exceeding Planck's blackbody radiation law, *Applied Physics Letters* **92**, 133106, 2008.

[5] Rousseau E., Siria A., Jourdan G., Volz S., Comin F., Chevrier J. and Greffet J.-J., Radiative heat transfer at the nanoscale, *Nature Photonics* **3**(9), 514-517, 2009.

[6] Ottens R.S., Quetschke V., Wise S., Alemi A.A., Lundock R., Mueller G., Reitze D.H., Tanner D.B. and Whiting B.F., Near-field radiative heat transfer between macroscopic planar surfaces, *Physical Review Letters* **107**, 014301, 2011.

[7] Song B., Ganjeh Y., Sadat S., Thompson D., Fiorino A., Fernández-Hurtado V., Feist J., Garcia-Vidal F.J., Cuevas J.C., Reddy P. and Edgar M., Enhancement of near-field radiative heat transfer using polar dielectric thin films, *Nature Nanotechnology* **10**, 253–258 , 2015.

[8] Kim K., Song B., Fernández-Hurtado V., Lee W., Jeong W., Cui L., Thompson D., Feist J., Reid M.T.H., García-Vidal F.J., Carlos Cuevas J., Meyhofer E. and Reddy P.,

Radiative heat transfer in the extreme near field, *Nature* **528**, 387–391, 2015.

[9] Song B., Thompson D., Fiorino A., Ganjeh Y., Reddy P. and Meyhofer E., Radiative heat conductances between dielectric and metallic parallel plates with nanoscale gaps, *Nature Nanotechnology*, in press, 2016.

[10] St-Gelais R., Zhu L., Fan S. and Lipson M., Near-field radiative heat transfer between parallel structures in the deep subwavelength regime, *Nature Nanotechnology*, in press, 2016.

[11] DiMatteo R.S., Greiff P., Finberg S.L., Young-Waithe K.A., Choy H.K.H., Masaki M.M. and Fonstad C.G., Enhanced photogeneration of carriers in a semiconductor via coupling across a nonisothermmal nanoscale vacuum gap, *Applied Physics Letters* **79**(12), 1894-1896, 2001.

[12] Whale M.D. and Cravalho E.G., Modeling and performance of microscale thermophotovoltaic energy conversion devices, *IEEE Transactions on Energy Conversion* **17**(1), 130-142, 2002.

[13] Laroche M., Carminati R. and Greffet J-J., Near-field thermophotovoltaic energy conversion, *Journal of Applied Physics* **100**, 063704, 2006.

[14] Park K., Basu S., King W.P. and Zhang ZM. Performance analysis of near-field thermophotovoltaic devices considering absorption distribution, *Journal of Quantitative Spectroscopy and Radiative Transfer* **109**, 305-316, 2008.

[15] Francoeur M., Vaillon R., and Mengüç M.P., Thermal impacts on the performance of nanoscale-gap thermophotovoltaic power generators, *IEEE Transactions on Energy Conversion* **26**, 686-698, 2011.

[16] Bernardi M.P., Dupré O., Blandre E., Chapuis P.-O., Vaillon R. and Francoeur M., Impacts of propagating, frustrated and surface modes on radiative, electrical and thermal losses in nanoscale-gap thermophotovoltaic power generators, *Scientific Reports* **5**, 11626, 2015.

[17] Otey C.R., Lau W.T. and Fan S., Thermal rectification through vacuum, *Physical Review Letters* **104**, 154301, 2010.

[18] Basu S. and Francoeur M., Near-field radiative transfer based thermal rectification using doped silicon, *Applied Physics Letters* **98**, 113106, 2011.

[19] Greffet J.-J., Carminati R., Joulain K., Mulet J.-P., Mainguy S. and Chen Y., Coherent emission of light by thermal sources, *Nature* **416**, 61-64, 2002.

[20] Lee B.J., Wang L.P. and Zhang Z.M., Coherent thermal emission by excitation of magnetic polaritons between periodic strips and a metallic film, *Optics Express* **16**, 11328-11336, 2008.

[21] Francoeur M., Basu S. and Petersen S.J., Electric and magnetic surface polariton mediated near-field radiative heat transfer between metamaterials made of silicon carbide

particles, *Optics Express* **19**, 18774-18788, 2011.

[22] Jones A.C. and Raschke M.B., Thermal infrared near-field spectroscopy, *Nano Letters* **12**, 1475-1481, 2012.

[23] Babuty A., Joulain K., Chapuis P.-O., Greffet J.-J. and De Wilde Y., Blackbody spectrum revisited in the near field, *Physical Review Letters* **110**, 146103, 2013.

[24] O'Callahan B.T., Lewis W.E., Jones A.C. and Raschke M.B., Spectral frustration and spatial coherence in thermal near-field spectroscopy, *Physical Review B* **89**, 245446, 2014.

[25] Joulain K., Ben-Abdallah P., Chapuis P.-O., De Wilde Y., Babuty A. and Henkel C., Strong tip–sample coupling in thermal radiation scanning tunneling microscopy, *Journal of Quantitative Spectroscopy and Radiative Transfer* **136**, 1-15, 2014.

[26] Mamin H.J., Thermal writing using a heated atomic force microscope tip, *Applied Physics Letters* **69**, 433, 1996.

[27] Wilder K., Quate C.F., Adderton D., Bernstein R. and Elings V., Noncontact nanolithography using the atomic force microscope, *Applied Physics Letters* **73**, 2527, 1998.

[28] Hawes E.A., Hastings J.T., Crofcheck C. and Mengüç M.P., Spatially selective melting and evaporation of nanosized gold particles, *Optics Letters* **33**, 1383-1385, 2008.

[29] Loke V.L.Y. and Mengüç M.P., Surface waves and atomic force microscope probe-particle near-field coupling: Discrete dipole approximation with surface interaction, *Journal of the Optical Society of America A* **27**(10), 2293-2203, 2010.

[30] De Wilde Y., Formanek F., Carminati R., Gralak B., Lemoine P.-A., Joulain K., Mulet J.-P., Chen Y. and Greffet J.-J., Thermal radiation scanning tunneling microscopy, *Nature* **444**, 740-743, 2006.

[31] Palik E.D., *Handbook of Optical Constants of Solids*, Academic Press, Boston, 1985.

[32] Francoeur M., Mengüç M.P. and Vaillon R., Spectral tuning of near-field radiative heat flux between two thin silicon carbide films, *Journal of Physics D: Applied Physics* **43,** 075501, 2010.

[33] Zhang Z.M, *Micro/Nanoscale Heat Transfer*, McGraw-Hill, New York, 2007.

[34] Novotny L. and Hecht B., *Principles of Nano-Optics*, Cambridge University Press, New York, 2006.

[35] Joulain K., Mulet J.-P., Marquier F., Carminati R. and Greffet J.-J., Surface electromagnetic waves thermally excited: Radiative heat transfer, coherence properties and Casimir forces revisited in the near field, *Surface Science Reports* **57**, 59-112, 2005.

CHAPTER 7

CONCLUSIONS

Techniques for modeling near-field radiative heat transfer were discussed in this dissertation. These techniques provide solutions to near-field thermal radiation in several configurations including thin films, arbitrary-shaped objects and arbitrary-shaped objects interacting with an infinite surface. The proposed techniques were applied to study the physics of near-field radiative heat transfer in a number of geometries, namely thin films, sphere-sphere, sphere-surface, cube-cube and probe-surface. The main results of this research and recommendations for future work are provided hereafter.

7.1 Size effect on the emissivity of thin films

The emissivity of thin films was studied using a direct model based on fluctuational electrodynamics. A closed-form expression for thickness-dependent emissivity of thin films was derived, which can also be considered as a mathematical proof of Kirchhoff's law. The derived expression was applied for studying the emissivity of a number of metallic and dielectric films. The simulation results revealed that thermal emission in dielectrics is a volumetric process, such that thicker dielectric films have larger emissivities. However, the emissivity of metals increases with decreasing film thickness. This counterintuitive behavior is due to the extraneous contributions of

waves experiencing multiple reflections within the thin layer, which are usually internally absorbed for metallic bulks. The simulations showed that the critical thickness above which the size effect is not observed has different orders of magnitude for dielectrics and metals. While the critical thickness of dielectric materials can be as large as a few centimeters, the critical thickness of metals is about a hundred nanometers. Finally, a simple expression based on the radiation penetration depth was provided for estimating the critical thickness of materials.

A next step in this project would be analyzing the emissivity of one-dimensional layered media. This is of particular interest since thin films are usually deposited on a substrate. It is beneficial to investigate how the presence of a substrate affects the emissivity of thin films. The results of this study would also be helpful for tuning the emissivity of multilayer hyperbolic metamaterials [1,2].

7.2 Modeling of near-field thermal radiation in complex, three-dimensional and multiscale geometries

A novel computational method called the thermal discrete dipole approximation (T-DDA) was proposed, implemented and verified for large-scale computations of near-field thermal radiation in complex three-dimensional geometries. The T-DDA is based on discretizing the volume integral form of the thermal stochastic Maxwell equations, and is conceptually similar to the discrete dipole approximation (DDA). In the T-DDA, objects are discretized into cubical subvolumes conceptualized as electric point dipoles. The dipole moment of each subvolume includes a thermally fluctuating component accounting for thermal agitation of charged particles inside the subvolume. The T-DDA

was verified against the analytical solution of the radiative conductance between two spheres separated by a subwavelength gap. Excellent agreement was found between the T-DDA and analytical solutions for various sphere sizes, gap sizes and dielectric functions. Additionally, the T-DDA was applied to simulate the radiative conductance of two cubes for the first time. The T-DDA converges very rapidly for cubes compared to spheres. The fast convergence of the T-DDA for cubes is attributed to the fact that the shape error, due to approximating an object with a cubical lattice, is nonexistent in the case of cubes. The results of this study showed that the T-DDA is a robust and relatively simple numerical method for modeling near-field radiative heat transfer in complex geometries.

After verification of the T-DDA, an extensive convergence analysis of the method was performed using the analytical solution for two spheres. The approximations associated with the T-DDA were identified and discussed. The main parameters affecting the T-DDA accuracy are the refractive index, the size of the spheres, and their separation distance. The accuracy of the T-DDA was analyzed for six different refractive indices, including high and low real and imaginary parts, and a refractive index corresponding to surface phonon-polariton resonance of a silica sphere. Various sphere sizes and gap thicknesses ranging from much smaller than the wavelength to comparable to the wavelength were considered. It was found that regardless of the gap thickness and sphere size, the T-DDA accuracy decreases as the real and imaginary parts of the refractive index increase. A large refractive index negatively affects the accuracy of the T-DDA through increasing shape error and the error associated with assuming uniform dyadic Green's function and electric field inside the subvolumes. Since the resonant refractive

index has a moderate value ($|m|$ = 1.39, m being the refractive index), the T-DDA converges very rapidly for the resonant mode. This is of a great importance because the total radiative conductance between spheres is dominated by the contribution of surface phonon-polaritons in the near-field regime. An almost constant decreasing trend was observed in the T-DDA error with increasing the number of subvolumes. However, computational requirements of the T-DDA increase nonlinearly with increasing the number of subvolumes. As such, the maximum number of subvolumes that can be used in the T-DDA simulations is limited by the available computational resources. A solution to this bottleneck is to use a nonuniform discretization scheme, where the size of the subvolumes increases from the front sides of the spheres (i.e., the sphere sides facing each other) toward their back sides. A fine discretization at the front side is more beneficial than at the backside, since the shape error and the variation of the electric field inside the spheres is more dominant at the front side. The nonuniform discretization is most useful when significant absorption occurs within a small portion of the sphere and when the sphere size to gap ratio is very large. Using nonuniform discretization, an error less than 5% was obtained in the T-DDA simulations for 74% of the cases studied. The T-DDA error for nonspherical geometries is expected to be smaller than for the spheres, since the shape error for spheres is very large.

It is very challenging to model radiative heat transfer between objects with different length scales. However, multiscale problems are encountered in many potential near-field thermal radiation applications, where complex-shaped micro/nanoscale objects interact with a large surface. To address this multiscale challenge, surface interactions were included analytically into the T-DDA formalism such that the necessity of discretizing

the surface is eliminated. The presence of the surface modifies the T-DDA formalism in two ways. The first modification is concerned with the indirect interaction between the objects through reflection of the thermal electromagnetic field at the surface. This contribution was accounted for using a reflection-interaction matrix derived based on Sommerfeld's theory of electric dipole radiation above an infinite surface. The second modification is associated with thermal emission from the surface when it is at a temperature larger than absolute zero. Thermal emission from an infinite surface is well-known and is obtained from fluctuational electrodynamics. The new version of the T-DDA accounting for these two additional contributions, referred to as the T-DDA with surface interaction, was verified against the analytical solution of heat rate between a sphere and a surface. Excellent agreement between the T-DDA with surface interaction and the analytical solution was obtained. The T-DDA with surface interaction was then applied to model the heat rate between a complex-shaped silica probe and a silica surface. The probe dimensions are typical to what is used in near-field thermal spectroscopy measurements [3]. The probe has a sharp tip of 57.8 nm and a height of 4.97 μm. The T-DDA was employed to model the net spectral heat rate between the probe and the surface within a frequency band of 0.04 eV to 0.17 eV. In the extreme near-field regime, the heat transfer between the probe and the surface is dominated by the contribution of surface phonon-polaritons. In the limit that $d \rightarrow 0$, the total heat rate between the probe and the surface approaches a d^{-2} power law identical to what is observed in the two-surface geometry. In this regime, the total heat rate and the location of the resonant frequencies can be predicted using the proximity approximation. As the gap size d increases, the contribution from localized surface phonons becomes significant. When the gap thickness

is comparable to the probe tip size, resonance splitting is observed in the heat rate spectrum due to localized surface phonon modes along the minor axis of the probe. In this regime, the location of resonances can be estimated by approximating the probe as a prolate spheroidal dipole with the same height and volume as the probe. The values of the heat rate can also be roughly approximated using the spheroidal dipole model. The spheroidal dipole approximation is valid when its axes are smaller or comparable to the wavelength, while the radius of curvature at its closest vertex to the surface is a few times smaller than the gap thickness. A small radius of curvature compared to the gap size ensures negligible contribution from multiple reflections of the thermal electromagnetic field between the dipole and the surface.

The T-DDA was proved to be a robust and efficient numerical method for modeling near-field thermal radiation in arbitrary geometries. However, the performance of the T-DDA can be improved in several ways. The T-DDA is a particular implementation of the method of moments [4]. Currently, the basis and testing functions used in the T-DDA are constant function and Dirac-delta function, respectively. The accuracy of the T-DDA can be improved by using higher-order functions [5]. The weighted discretization approach [6,7] and the filtered coupled-dipole method [7-9] are other techniques that can potentially accelerate the convergence of the T-DDA. Currently, the maximum number of subvolumes that can be used in the T-DDA simulations is limited to a few hundred thousands. This limitation is due to the memory requirement and computational time associated with storing and inverting the interaction matrix. The computational demand of the T-DDA can be reduced considerably using an approach based on the fast Fourier transform [5]. In addition, the T-DDA is a very flexible method and can be applied to a

wide variety of problems. A future research direction would be to generalize the T-DDA such that it can be applied to magnetic materials [10,11], inhomogeneous materials, anisotropic materials, geometries including objects buried in a surface [12], periodic geometries [13,14], Casimir interactions [15] and cases in which nonlocal effects are significant [16-19].

7.3. Investigation of resonance redshift in near-field thermal spectroscopy

The T-DDA with surface interaction was employed to explain the reason behind the resonance redshift observed in near-field thermal spectroscopy measurements. The latest experimental attempts reported that the resonance frequency of the measured far-field signal can be redshifted by 5 cm^{-1} to 50 cm^{-1} compared to the near-field thermal spectrum of the sample as predicted by fluctuational electrodynamics [3,20]. The T-DDA analysis of the interactions between a silicon probe and a silicon carbide sample revealed that the spectrum of the far-field signal depends not only on the near-field thermal spectrum of the sample but also on the spectral distribution of the reflection interactions between the probe and the sample. The net spectral heat rate of a probe with a sharp tip of size 57.8 nm and a length of 4.97 μm was simulated using the T-DDA for a gap size of 10 nm. The simulations showed that reflection interactions between the probe and the sample induce an additional resonance in the heat rate spectrum which is spectrally redshifted by 10.8 cm^{-1} compared to surface phonon-polariton resonance. The location and magnitude of this resonance strongly depend on the shape and size of the probe as well as the gap thickness. For some probe-sample configurations, the reflection-interaction resonance might dominate surface phonon-polariton resonance in the far-field signal. An

investigation of the spectral heat flux between the sample and a thin film, used for modeling the probe, supported the T-DDA results.

This study demonstrated that the resonance redshift is a physical phenomenon arising due to enhanced reflection interactions between the probe and the sample. However, the exact physical mechanism responsible for this enhancement is still not clear and is left as a future research effort. A clear understanding of the reflection interactions between the probe and the sample would be beneficial for designing an experimental setup that does not induce a resonance redshift. In this case, the far-field signal can be directly related to the near-field thermal spectrum of the sample. In the current study, the spectrum of the probe-sample heat rate was simulated. Another recommendation for future work is to model the spectral distribution of the far-field signal rather than the heat rate. Both the probe heat rate and the far-field signal are proportional to the correlation matrix of the induced dipole moments of subvolumes used for discretization of the probe. As such, a similar spectral distribution is expected for both quantities. However, modeling the exact location and magnitude of the resonances of the far-field signal would be beneficial.

7.4. References cited

[1] Poddubny A., Iorsh I., Belov P. and Kivshar Y., Hyperbolic metamaterials, *Nature Photonics* **7**, 948-957, 2013.

[2] Shekhar P., Atkinson J. and Jacob Z., Hyperbolic metamaterials: Fundamentals and applications, *Nano Convergence* **1**, 14, 2014.

[3] O'Callahan B.T., Lewis W.E., Jones A.C. and Raschke M.B., Spectral frustration and spatial coherence in thermal near-field spectroscopy, *Physical Review B* **89**, 245446, 2014.

[4] Peterson A.F., Ray S.L. and Mittra R., *Computational Methods for Electromagnetics*, IEEE Press, 1998.

[5] Polimeridis A.G., Villena J.F., Daniel L. and White J.K., Stable FFT-JVIE solvers for

fast analysis of highly inhomogeneous dielectric objects, *Journal of Computational Physics* **269**, 280-296, 2014.

[6] Piller N.B., Influence of the edge meshes on the accuracy of the coupled-dipole approximation, *Optics Letters* **22**, 1674-1676, 1997.

[7] Piller N.B., Coupled-dipole approximation for high permittivity materials, *Optics Communications* **160**, 10-14, 1999.

[8] Piller N.B., Increasing the performance of the coupled-dipole approximation: a spectral approach, *IEEE Transactions on Antennas and Propagation* **46**, 1126-1137, 1998.

[9] Yurkin M.A., Min M. and Hoekstra A.G., Application of the discrete dipole approximation to very large refractive indices: Filtered coupled dipoles revived, *Physical Review E* **82**, 036703, 2010.

[10] Cai W. and Shalaev V., *Optical Metamaterials: Fundamentals and Applications*, Springer, New York, 2010.

[11] Joulain K., Drevillon J. and Ben-Abdallah P., Noncontact heat transfer between two metamaterials, *Physical Review B* **81**, 165119, 2010.

[12] Nebeker B.M., *Modeling of light scattering from features above and below surfaces using the discrete-dipole approximation*, Ph.D. thesis, Arizona State University, 1998.

[13] Draine B.T. and Flatau P.J., Discrete-dipole approximation for periodic targets: theory and tests, *Journal of the Optical Society of America A* **12**, 2693-2703, 2008.

[14] Chaumet P.C., Rahmani A. and Bryant G.W., Generalization of the coupled dipole method to periodic structures, *Physical Review B* **67**, 165404, 2003.

[15] Rodriguez A.W., Capasso F. and Johnson S.G., The Casimir effect in microstructured geometries, *Nature Photonics* **5**, 211-221, 2011.

[16] Henkel C. and Joulain K., Electromagnetic field correlations near a surface with a nonlocal optical response, *Applied Physics B* **84**, 61-68, 2006.

[17] Chapuis P.-O., Volz S., Henkel C., Joulain K. and Greffet J.-J., Effects of spatial dispersion in near-field radiative heat transfer between two parallel metallic surfaces, *Physical Review B* **77**, 035431, 2008.

[18] Singer F., Ezzahri Y. and Joulain K., Near field radiative heat transfer between two nonlocal dielectrics, *Journal of Quantitative Spectroscopy and Radiative Transfer* **154**, 55-62, 2015.

[19] Chiloyan V., Garg J., Esfarjani K. and Chen G., Transition from near-field thermal radiation to phonon heat conduction at sub-nanometre gaps, *Nature Communications* **6**, 6755, 2015.

[20] Babuty A., Joulain K., Chapuis P.-O., Greffet J.-J. and De Wilde Y., Blackbody spectrum revisited in the near field, *Physical Review Letters* **110**, 146103, 2013.